Excited Electron Production at HERA

Samantha. A. Murray

A thesis submitted to the University of Manchester for the degree of Doctor of Philosophy in the Department of Physics in the Faculty of Science.

January 1992

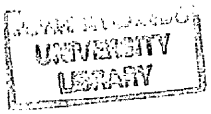

Abstract

A Monte Carlo study of excited electron production using the H1 detector at the ep collider HERA at DESY, Hamburg is presented. Using the process $ep \rightarrow e^*X \rightarrow e\gamma X$ kinematic distributions of the events are presented and discussed. The backgrounds due to wide angle bremsstrahlung and neutral current deep inelastic scattering events are studied and a set of event selection cuts which best isolate the excited electron signal developed. Limits on the scale of the production interaction and excited electron masses accessible to HERA are presented.

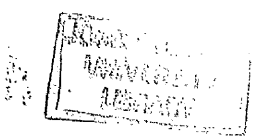

No portion of the work referred to in this thesis has been submitted in support of an application for another degree or qualification of this or any other institute of learning.

The author was educated at Sydenham Girls School, London between 1978 and 1985, and obtained her first degree in physics at Leeds University in 1988. In 1989 she was awarded a Diploma in Advanced Studies in Science from Manchester University. The work presented in this thesis was carried out at Manchester University and DESY, Hamburg.

To my Mother.

For her constant love and support.

Contents

Chapter 1

Introduction

Composite models are one class of theory proposed as an extension to the Standard Model. A natural consequence of such theories is the existence of excited states of quarks and leptons.

In this thesis a Monte Carlo study of the production and detection of excited electron events from ep collisions in the H1 detector at HERA ($\sqrt{s} = 314GeV$) is presented.

The structure of the report is as follows.

In chapter 2 a brief overview of the standard model is given. The present limitations and outstanding questions are examined and composite models introduced as one possible extension to the theory. The current status of relevant experimental composite searches is then summarised.

Chapter 3 examines the production of excited electrons at ep colliders. A realistic model with a minimal number of free parameters is introduced and used to derive production cross section estimates at HERA energies. The motivation for studying the $e^* \rightarrow e\gamma$ decay channel is presented and details of the anticipated background processes given.

The HERA collider and H1 detector are described in chapter 4 together with details of the expected performance of the various subdetectors. Chapter 5 introduces the H1 simulation software suite, in particular the detector and relevant generator Monte Carlos are discussed.

In chapter 6 a set of event selection criteria which best isolate an excited electron signal from the anticipated background processes over the mass range accessible to HERA ($40 - 250\ GeV$) is developed. This involves consideration of excited electron production kinematics and final state event characteristics. Further cuts are proposed to minimize

wide angle bremsstrahlung backgrounds and yield a final event sample relatively free from neutral current deep inelastic scattering contamination. Complete background event samples representing large values of integrated luminosity are then processed.

In chapter 7 these results are used to parameterise the anticipated background distributions in terms of effective cross sections. By considering the characteristics of excited electron invariant mass peaks and these distributions, 95% confidence levels are derived for lower limits on the characteristic scale of the production interaction and highest mass of excited electron which can be studied at HERA. These results are compared with present limits and those anticipated from LEP2. Suggestions for improving these limits are made.

Chapter 2

The Standard Model and Compositeness

In this chapter a brief overview of the main features of the Minimal Standard Model is given. More comprehensive treatments of the subject can be found elsewhere [1, 2].

The outstanding questions and current limitations of the model are then discussed and compositeness introduced as one possible extension to the theory.

Finally, a summary of the current status of some relevant composite searches is given.

2.1 The Standard Model

The success of the standard model, and its place at the core of current high energy physics theory, is easily understood. The model encompasses all currently known phenomenology of 3 of the 4 fundamental forces. It has the attractive feature of a consistent treatment of the seemingly highly disparate interactions, possibly unifying them as different manifestations of a single underlying principle.

The class of theories which make up the Standard Model are known as **RENORMALISABLE QUANTUM FIELD THEORIES WITH LOCAL GAUGE INVARIANCE.**

A brief explanation of each of these terms follows, with examples drawn from the prototype and most successful of such theories, Quantum Electrodynamics *(QED)*.

			Charge
Fermions (Spin=$\frac{1}{2}$)	Leptons	$\begin{pmatrix} \nu_e \\ e \end{pmatrix}_L \quad \begin{pmatrix} \nu_\mu \\ \mu \end{pmatrix}_L \quad \begin{pmatrix} \nu_\tau \\ \tau \end{pmatrix}_L$	0
		$e_R \qquad \mu_R \qquad \tau_R$	-1
			-1
	Quarks	$\begin{pmatrix} u \\ d \end{pmatrix}_L \quad \begin{pmatrix} c \\ s \end{pmatrix}_L \quad \begin{pmatrix} t^* \\ b \end{pmatrix}_L$	$+\frac{2}{3}$
			$-\frac{1}{3}$
		$\begin{pmatrix} u \\ d \end{pmatrix}_R \quad \begin{pmatrix} c \\ s \end{pmatrix}_R \quad \begin{pmatrix} t^* \\ b \end{pmatrix}_R$	$+\frac{2}{3}$
			$-\frac{1}{3}$
Gauge Bosons	Vector Bosons (Spin=1)	γ	0
		$W^{\pm}$, Z^0	$\pm 1, 0$
		g_i $(i = 1....8)$	0
	Scalar Bosons (Spin=0)	H^{0*}	0

*Yet to be experimentally observed.

Table 2.1: The Fundamental Particles

2.1.1 Quantum Field Theory

Tables 2.1 and 2.2 show the fundamental particles and interactions of the standard model. All matter is made up of half integral spin *fermions* while the integer spin *bosons* mediate the forces by which fermions interact and can be thought of as a glue by which matter is held together.

In quantum field theory the fermions and bosons are described in terms of *vector* and *scalar* fields in space-time. The number of components of the field depends on the number

INTERACTION	CHARGE	MEDIATING BOSON	RANGE	RELATIVE STRENGTH
STRONG	Color	Gluon	$\approx 1F$	1
ELECTROMAGNETIC	Electric charge Q	Photon	∞	10^{-2}
WEAK	Weak charge g	$W^{\pm}, Z^{0}$	$\approx \frac{1}{M_W}$	10^{-6}
GRAVITY	Mass	Graviton (?)	∞	10^{-39}

Table 2.2: The Fundamental Forces

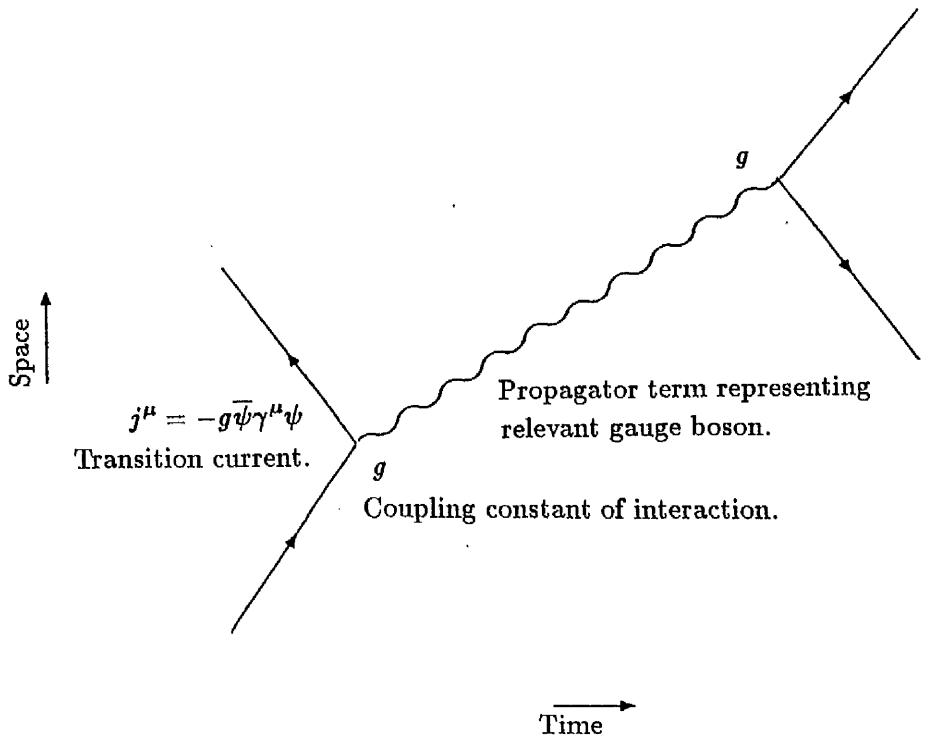

Figure 2.1: Interactions as visualized in QFT

of quantum mechanical spin states of the field quanta.

Fermion fields interact by coupling to boson fields via the exchange of virtual quanta. The quantum numbers of the exchange boson are specific to the type of interaction (Fig. 2.1).

The spontaneous existence of a virtual exchange particle does not violate conservation

of energy since the time for which it exists is restricted by the uncertainty principle;

$$\Delta E.\Delta t \leq \hbar \qquad \Delta t \leq \frac{\hbar}{mc^2} \tag{2.1}$$

Every field has an associated Lagrangian in the same way as do macroscopic systems.

$$\mathcal{L} = T - V \tag{2.2}$$

T = Kinetic energy

V = Potential energy

The field's Lagrangian is a representation of the energy distribution within it. The equations of motion of the particle represented by the field can be obtained from the Lagrangian [2] as in classical mechanics but the expression is now transformed to a continuous coordinate system rather than referring to a discrete body. For example

$$\mathcal{L} = i\overline{\psi}\gamma^{\mu}\partial_{\mu}\psi - m\overline{\psi}\psi \tag{2.3}$$

is the QED Lagrangian describing a free spin $\frac{1}{2}$ particle mass m.

$\psi(x)$ - 4 component spinor field describing the matter field of a charged particle.

2.1.2 Gauge Invariance

One result of QFT formalism is that for every particle there is an associated *phase* as in classical wave mechanics. The experimentally observed fact that there is no way of determining the absolute phase of a electron field leads to the constraint that the Lagrangian must be invariant under local phase transformations, i.e, applying an arbitrary phase transformation in space and time. This invariance is more commonly known as *gauge invariance.*

This is mathematically represented by a transformation of the form;

$$\psi(x) \rightarrow e^{i\alpha(x)}\psi(x) \tag{2.4}$$

$x = (ct, \mathbf{x})$ – Space-time coordinate.

α – Arbitrary function of space and time.

The QED Lagrangian of equation 2.3 is *not* invariant with respect to such transformations since the kinetic energy term changes;

$$\partial_{\mu}\psi \longrightarrow e^{i\alpha(x)}\partial_{\mu}\psi + iei\alpha(x)\psi\partial_{\mu}\psi \tag{2.5}$$

The modification to the Lagrangian necessary to restore local gauge invariance is;

$$D_\mu \equiv \partial_\mu - ieA_\mu \tag{2.6}$$

where

$$A_\mu \rightarrow A_\mu + \frac{1}{e}\partial_\mu \alpha \tag{2.7}$$

A_μ is identified with a vector field, spin 1, mass 0. This is the photon field and the corresponding particle is known as a gauge particle since it mediates the gauge interaction.

Thus, the constraint of local gauge invariance modifies the free electron Lagrangian by inducing electromagnetic interactions between an electron current J^μ and a photon field A_μ

The local transformation can also be written as;

$$\psi(x) \rightarrow e^{i\Lambda Q}\psi \tag{2.8}$$

Λ is an arbitrary real number.

Q is the electric charge operator associated with the field.

Q can be interpreted as the quantum mechanical generator of the local phase transformation group U(1), i.e, the set of unitary 1×1 matrices.

Terms in the modified Lagrangian can be identified with couplings and propagators in the QFT Feynman diagram representing the relevant interaction [2], and thus one becomes capable of making predictions of cross sections, lifetimes *etc* [3]. Since the QED coupling constant α is so small ($\approx \frac{1}{137}$) perturbative calculations can be performed taking into account higher order corrections (see Section 2.1.3) resulting in highly accurate predictions.

2.1.3 Renormalisation

The very nature of virtual states means that interactions between two particles have to take into account *higher order corrections*, i.e, the possibility (weighted by the appropriate coupling at each vertex) that an exchanged photon might have turned into an e^+e^- pair *etc.* and thus (see Figure 2.2) the full photon propagator must take into account all such corrections. This results in a divergence to ∞ of the integrals used in the calculations.

Fuller discussions of renormalisability are available elsewhere. In summary the procedure involves;

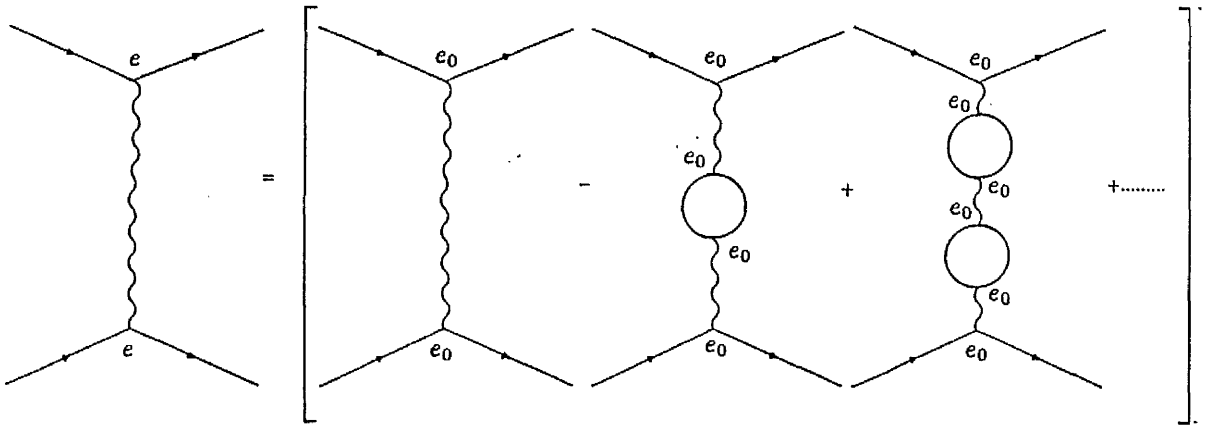

Figure 2.2: Higher Order Corrections to Interactions

- The integrals are *regularized* by the introduction of a large mass parameter Λ such that as $\Lambda \rightarrow \infty$ the regularising factor $\rightarrow 1$.
- All the divergent terms can now be expressed in terms of Λ which can therefore be used as a finite cutoff in virtual momentum.
- Alternatively, the divergences can be removed by an *infinite rescaling* of the fields and coupling constants.
- If the cutoff is now removed, the rescaling variables develop infinities of their own which compensate and you are left with.

$$e = Z_e e_0$$

The so-called *bare* parameter e_0 which appears in the Lagrangian and represents the charge of the electron in the absence of the 'cloud' of virtual states is redefined to the physically measured value e. Since the bare charge is not constrained by the theory anyway this is reasonable.

Thus, with the introduction of 3 arbitrary parameters (rescalings), h, e and m, all infinities in the observables are cancelled and QED remains highly predictive since other rescaled quantities are now completely defined and can therefore be used to test the theory.

In order for the rescaled values e and D to remain dimensionless a *mass scale* μ must be introduced.

$$Z = Z(\frac{\Lambda^2}{\mu^2}, e_0) \tag{2.9}$$

This is the renormalisation mass and different choices, although resulting in different expansions of the integrals does not affect the observable physics processes. Thus renormalisation also introduces a mass scale into the calculations.

Using the technique of renormalisation QED can make predictions accurate to $\approx 10^{-9}$ for relevant interactions. In fact it is the most accurate theory in modern physics.

2.1.4 Quantum Chromodynamics

The treatment of the observed phenomenology of the strong interaction is based upon a generalisation of QED.

However, there are now 3 distinct color charges which the quarks can possess, red, green and blue, analogous to electric charge. This extra degree of freedom was invoked to preserve the Pauli exclusion principle, the restriction that no two fermions can simultaneously possess the same quantum numbers, in light of the existence of spin $\frac{3}{2}$ baryons such as the $\Delta^{++}(u\uparrow u\uparrow u\uparrow)$ which would otherwise have 3 quarks with the same space and spin quantum numbers and therefore violate the principle.

The color charges are visualized as forming a triplet state under the application of an SU(3) local gauge transformation. These transformations now change the *particle* rather than just the *phase* of the particle.

In the same way as the freedom to change the local phase of a charged particle imposes a coupling to the photon field, so the 8 independent symmetry transformations which can change the color of a quark result in 8 spin 1 massless gauge fields, the gluons. Each gluon carries one color, one anti-color charge.

The difference between these fields and the photon field however is that gluons are themselves colored objects, each carries one color one anticolor charge. Gluons can therefore feel the strong force they mediate and this *self-interaction* gives rise to two important physical consequences.

The first is *asymptotic freedom*, the effective weakening of color charge at short distances. Every quark is visualized as being surrounded by a cloud of virtual gluons which act to enhance the color charge of the quark. The effective color charge increases as distance increases (Q^2 decreases) since this *anti-screening* cloud is not penetrated and virtual gluons of the same color as the quark act to enhance the net color charge. At high energies on the other hand, $Q^2 > \approx 5\ GeV^2/c$ the quarks inside hadrons behave as though they are almost free, the strong coupling constant α_s is small enough for perturbative techniques to be used to calculate hadronic processes successfully.

The second consequence is permanent *quark confinement* inside colorless hadrons. As distance increases from a colored object the gluon self interaction results in a rapidly increasing number of virtual gluons acting to increase the color charge. Thus, it becomes impossible for a colored object to propagate any distance and quarks are only observed within hadrons whose net color is zero.

Because of these phenomena, the strong coupling constant α_s is said to *run* with Q^2, i.e, the observed magnitude of α_s is dependant on the energy of the probe. The magnitude is such that terms due to higher order corrections are no longer negligible for low Q^2 processes due to the proliferation of virtual gluons and QCD calculations become highly complex. The theory thus loses a lot of its predictive capabilities in this non-perturbative regime.

2.1.5 Electroweak Theory

Although electromagnetic interactions had been described highly successfully by QED, there was a strong motivation for a theoretical unification with the weak interactions. These are the interactions which mediate neutrino processes (no electromagnetic or strong charge) and flavour changing quark processes. Some of the mediators, the $W^{\pm}$ bosons, also possess electric charge, these are the mediators of the so-called weak charged current interactions e.g

$$d \rightarrow u + e + \overline{\nu}_e$$

$$\nu_\mu N \rightarrow \mu^- X$$

while the other weak gauge boson, the Z^0, mediates the weak neutral current interactions;

$$eN \rightarrow eX$$

$$\overline{\nu}_\mu N \rightarrow \overline{\nu}_\mu X$$

Both electromagnetic and some weak interactions involve electric charge and the prediction of the W boson mass was based on the assumption that the interactions were fundamentally similar, the observed differences in strength and range being due to the massive nature of the exchange boson for weak processes. However, there had been problems trying to incorporate these massive mediators into a similar renormalisable gauge invariant formalism as that of QED.

The resulting theory based upon the work of Glashow, Salam and Weinberg is based on a *Broken* SU(2)×U(1) symmetry.

The SU(2) group represents a local gauge invariance with respect to weak isotopic spin, under which the leptons and quark transform as their well known doublets. The generators are the 3 components of weak isospin $I^{\pm}, I_3$. The U(1) is a phase transformation as in QED but now with respect to weak hypercharge;

$$Y = I_3 + Q \tag{2.10}$$

Associated with the unbroken SU(2)×U(1) generators are 4 massless gauge bosons. However, of the observed gauge bosons, $W^{\pm}$, γ, Z^0, 3 are massive.

The most favoured solution to this problem is the Higgs mechanism of spontaneous symmetry breaking [4] which postulates the existence of a complex scalar field with a non zero vacuum expectation value mediated by 4 bosons which manifests itself at the energies so far probed by the massive results of its interaction with the massless gauge bosons of electroweak, the massive W and Z particles and the massless photon, and the Higgs particle, yet to be discovered.

The validity of the theory was proven by its successful prediction of the masses of the W and Z particles discovered at CERN [3].

2.1.6 Summary of the Standard Model

The successes of the standard model cannot be overemphasised. It is hoped that some of the attractiveness of the consistency of the treatment has been highlighted. This is summarised in Figure 2.3.

The recent high precision tests of the model at LEP [5] have experimentally confirmed the predictions of the Standard Model to a degree of accuracy never before attained. The

	LOCAL SYMMETRY	CURRENT	GROUP GENERATOR	ASSOCIATED GAUGE FIELD	INTERACTION
QED	U(1) of of electro-magnetism	J^μ	$\int d^3x J^0 = Q$ Electric charge	A_μ Photon	Electromagnetic $eJ^\mu A_\mu$
QCD	SU(3) color	J^μ_a	$\int d^3x J^\mu_a = Q_a$ 8 color charges	A^a_μ 8 massless gluons	Quark-Gluon $g_s J^\mu_a A^a_\mu$
ELECTROWEAK	SU(2) Weak isospin	J^μ	$\int d^3x J^0_{+,-,3} = I_{+,-,3}$	$W^{+,-,3}_\mu$ 3 massless bosons	Charged current $\frac{g}{\sqrt{2}} J^\mu_{+,-} W^{+,-}_\mu$ Neutral current $g J^\mu_3 W^3_\mu$ *
	U(1) Weak hypercharge	J^μ	$\int d^3x J^\mu = Y$	B_μ Massless gauge field	$\frac{1}{2} g' J^\mu B_\mu$ *

* Broken symmetry. $\Longrightarrow$

Massive $W^\pm$, Z^0, massless γ.

Table 2.3: The Local Symmetries of the Standard Model

top quark, which must exist if the standard model is correct, and the Higgs boson, whose existence is predicted in the currently most favoured mechanism for generating mass and not critical to the survival of the theory, have yet to be discovered but no significant anomalies in standard model predictions have been detected either.

2.2 Limitations of the Standard Model

As it stands there are 25 [6] independent free parameters implicit in the Standard Model. These include the masses of all the fundamental particles, the values of the coupling constants, the mixing angles representing the degree to which strong eigenstates differ from those which couple to electroweak and the phase δ of CP violating effects. The theory in no way predicts their values.

Other outstanding questions concern the various appearances of 3-fold divisions within the representations of the fundamental particles. There are 3 distinct 'families' of both quarks and leptons, each comprising a doublet of particles. Especially with respect to the leptons, a muon appears to simply be a heavy electron, the tau lepton an even heavier electron. The query arises that these mass differences could be the low energy manifestations of a broken symmetry just as the broken symmetry of electroweak provides a mass generation mechanism for the gauge bosons.

There is also no clear reason as to why there are 3 color states of quarks or why the fundamental quarks should carry electric charge of $\frac{1}{3}$ or $\frac{2}{3}$ that of the fundamental leptons.

No explanation is implicit in the standard model.

2.3 Compositeness

There are many competing models which aim to extend the theory and provide solutions to the unanswered questions, *e.g*, Supersymmetry and GUT's [1]. This text discusses composite models.

Although there are many different scenarios [6] these models all share the common assumption that quarks, leptons and perhaps even gauge bosons are bound states of several constituents.

The main attraction of such models is obvious, a proliferation of 'fundamental' particles has historically preceded the uncovering of yet another layer of substructure and accom-

panying reduction in arbitrary parameters and forced assumptions. The obvious examples being uncovering different layers of structure to the atom and the eventual identification of the many baryons and mesons as bound states of quarks.

Composite models assume that although the 'fundamental' particles are point-like at the energies so far probed they are in fact bound states confined by a very strong force. Different models assign different characteristics (and names) to the constituent particles, but *preon* is as good as any. A simple form of a composite extension to the standard model is one which postulates another gauge force similar to the strong and electroweak forces. This new confining force couples to a new internal quantum number, say 'hypercolor' assigned to the preons. Quarks and leptons are hypercolorless objects in the same way as baryons and mesons are colorless states. The symmetry of the standard model is therefore extended but the form of the new gauge group is highly arbitrary. There is also the possibility that current techniques are not applicable to this 'new' physics but postulating some form of the interaction is necessary if any useful work is to be done in the search for first signs of compositeness.

This immediately implies the existence of a 'Confinement Scale' or 'Compositeness Scale', Λ_c where the typical size of the bound states is $\mathcal{O}(\Lambda_c^{-1})$.

The magnitude of Λ_c must be much larger than the resulting bound states or else compositeness would have been manifest at energies already probed. Although this is different from the case with hadrons, models can be constructed with this feature [15].

It must be emphasised that there is, as yet, no experimental evidence which indicates that quarks, leptons or bosons are composite bodies and therefore it is virtually impossible to formulate any stringent theoretical framework for the model. However, one of the most interesting studies which takes place at any facility offering the chance to probe matter to a new energy scale is the search for evidence of substructure and limits have been set for several candidate models. This are are summarised in the next section.

2.4 Experimental Searches for Compositeness

There have been a variety of experimental results which can be used to set limits on parameters relevant to compositeness, see for example [6]. Here only the techniques which have produced the most stringent limits to date are discussed.

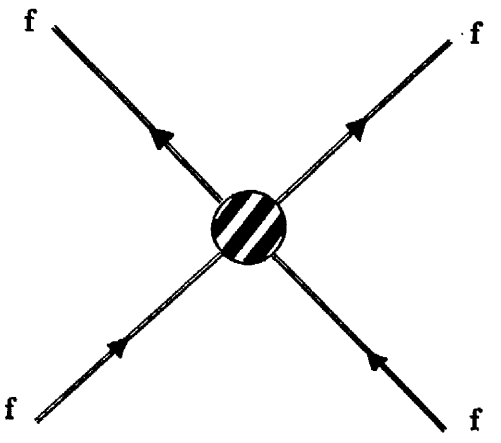

Figure 2.3: Four Fermion Contact Interaction Diagram.

A more exhaustive listing of limits set by various experiments can be found in [12]

2.4.1 Contact Interactions

The best limits on the magnitude of Λ_c have been set from studying contact interactions.

At energy scales much below Λ_c, the new interaction which mediates the binding of the particle constituents will have an effect on the effective interactions between fermions due to constituent exchange. The situation is analogous to low energy meson exchange between nucleons.

If the four fermions are identical, the magnitude of the effective interaction is model independent while for processes of the form

$$ee\mu\mu,\ ee\tau\tau,\ qqq'q'$$

contact interactions will appear in the models where the two fermions have constituents in common.

The experimental cross sections can then be compared with those predicted by the standard model [14, 19, 21] and the limits on agreement can be interpreted as limits on the magnitude of Λ_c.

The lower limits for Λ_c derived from such searches are summarized in Table 2.4 [11]. The most interesting numbers should be considered as those derived for the model inde-

$\Lambda^{+}_{LL}(eeee)$	$> 1.4\ TeV$, CL = 95%
$\Lambda^{-}_{LL}(eeee)$	$> 3.3\ TeV$, CL = 95%
$\Lambda^{+}_{LL}(qqqq)$	$> 0.7\ TeV$, CL = 95%
$\Lambda^{-}_{LL}(qqqq)$	$> 0.7\ TeV$, CL = 95%
$\Lambda^{+}_{LL}(ee\mu\mu)$	$> 4.4\ TeV$, CL = 95%
$\Lambda^{-}_{LL}(ee\mu\mu)$	$> 2.1\ TeV$, CL = 95%
$\Lambda^{+}_{LL}(ee\tau\tau)$	$> 2.2\ TeV$, CL = 95%
$\Lambda^{-}_{LL}(ee\tau\tau)$	$> 3.2\ TeV$, CL = 95%
$\Lambda^{+}_{LL}(eeqq)$	$> 0.9\ TeV$, CL = 95%
$\Lambda^{-}_{LL}(eeqq)$	$> 1.7\ TeV$, CL = 95%
$\Lambda^{+}_{LL}(\mu\nu_{\mu}e\nu_{e})$	$> 3.1\ TeV$, CL = 90%
$\Lambda^{-}_{LL}(\mu\nu_{\mu}e\nu_{e})$	$> 3.1\ TeV$, CL = 90%
where;	
$\Lambda = \Lambda^{\pm}_{LL}$	$(\eta_{LL},\ \eta_{RR},\ \eta_{LR} = (\pm 1, 0, 0)$

Table 2.4: Experimental limits on Λ_c.

pendent parameters.

2.4.2 New Particles

Arguably the most convincing evidence for the substructure of quarks and leptons would be the discovery of a relevant excited state.

The searches for excited leptons have looked for both pair produced excited states (If $E_{CM} > 2m_{l^*}$) via their normal gauge couplings, or single production. The former is a more reliable limit since the parameter λ ($=\frac{m_{l^*}}{\Lambda}$ - Λ is the characteristic scale of the excitation) representing the ll^* transition coupling to the gauge field has to be introduced when considering single production.

The current mass limits for excited leptons are summarised in Table 2.5 [16, 17].

$e^{*\pm}$
$m > 86GeV$, CL = 95% (if $\lambda_Z = 1$)
$m > 90.2GeV$, CL = 95% (if $\lambda_\gamma = 1$)
$m > 44.9GeV$, CL = 95% (from $e^{*+}e^{*-}$)
$\mu^{*\pm}$
$m > 86GeV$, CL = 95% (if $\lambda_Z = 1$)
$m > 44.6GeV$, CL = 95% (from $\mu^{*+}\mu^{*-}$)
$\tau^{*\pm}$
$m > 72GeV$, CL = 95% (if $\lambda_Z = 1$)
$m > 41.2GeV$, CL = 95% (from $\tau^{*+}\tau^{*-}$)

Table 2.5: Lower Limits on Excited Lepton Masses.($\lambda = \frac{m(l^*)}{\Lambda}$).

Chapter 3

Production of Excited Leptons at ep Colliders

In the previous section the concept of excited leptons was introduced as a typical consequence of composite models and the current experimental limits, dominated by the e^+e^- LEP results, given.

In this chapter the prospects for producing an excited electron at an ep collider are discussed. The expected production mechanisms are outlined and a realistic SU(2)×U(1) model introduced. This is then used to derive production cross sections for HERA energies.

The benefits of studying the $e^* \rightarrow e\gamma$ decay mode are discussed and the background processes introduced.

3.1 Production Mechanisms

A typical electron-proton collision at HERA energies is shown in Figure 3.1. Because of the high momentum transfers available at HERA it is essentially an electron-quark collider.

Several kinematical variables are useful quantities to use when studying HERA interactions;

$$s \equiv (p_e + p_p)^2 \simeq 4E_eE_p \tag{3.1}$$

is the centre of mass energy squared of the colliding particles.

$$Q^2 \equiv -q^2 = -(p_e - p_l)^2 \simeq 4E_eE_l \sin^2\frac{\theta_l}{2} \tag{3.2}$$

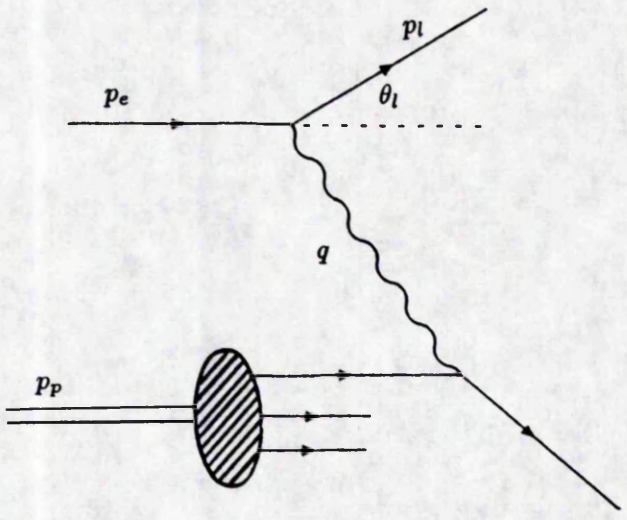

Figure 3.1: Typical electron-proton interaction at HERA

is the momentum transfer squared of the electron to the proton.

$$W^2 = (q + p_p)^2 = Q^2\frac{(1-x)}{x} + m_p^2 \tag{3.3}$$

is the mass squared of the resultant hadronic system.

$$m_p\nu \equiv p_p{\cdot}q \simeq 2E_p(E_e - E_l\cos^2\frac{\theta_l}{2}) \tag{3.4}$$

where ν is the energy of the current in the target rest frame. The dimensionless scaling variables, Bjorken x and y [22], given by

$$x \equiv \frac{Q^2}{2p_p{\cdot}q} = \frac{Q^2}{2m_p\nu} \simeq \frac{E_eE_l\sin^2\frac{\theta_l}{2}}{E_p(E_e - E_l\cos^2\frac{\theta_l}{2})} \tag{3.5}$$

$$y \equiv \frac{p_p{\cdot}q}{p_p{\cdot}p_e} = \frac{2p_p{\cdot}q}{s} = \frac{\nu}{\nu_{max}} \simeq \frac{E_e - E_l\cos^2\frac{\theta_l}{2}}{E_e} \tag{3.6}$$

x can be identified as the fraction of the proton momentum carried by the struck quark, and y as the fractional energy loss of the lepton in rest frame of the proton.

The production of excited electrons in ep collisions is expected via single production of e^*'s in either elastic or inelastic scattering processes (see Figure 3.2);

$$ep \rightarrow e^*X$$

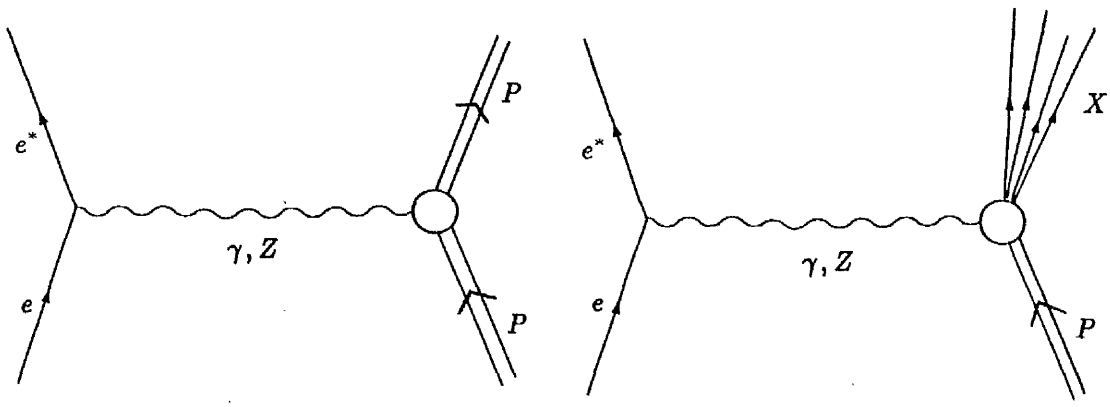

Elastic Production

Inelastic Production

Figure 3.2: Excited electron production processes in ep collisions

The e^* is then expected to decay;

$$e + p \rightarrow e^* + X \rightarrow e + \gamma + X$$

$$e + p \rightarrow e^* + X \rightarrow e + Z^0 + X$$

$$e + p \rightarrow e^* + X \rightarrow \nu_e + W^- + X$$

to either of its normal weak doublet particles depending on the mass and branching ratios.

3.2 Couplings and Models

In the absence of any phenomenology supporting compositeness it is somewhat arbitrary which model one chooses to represent the nature of the binding of the quark and lepton constituents.

The model used in this study [25] assumes that excited electrons have spin and isospin $\frac{1}{2}$ to reduce the number of free parameters. Because the production of excited electrons in the $ep \rightarrow e^*X$ process involves either γ or Z^0 exchanges the unknown $e^*e\gamma$ and e^*eZ^0 couplings have to be included in the expression for production, described by the effective Lagrangian,

$$\mathcal{L}_{eff} = \sum_{V=\gamma,Z,} \frac{e}{\Lambda} \overline{F} \sigma^{\mu\nu} (c_{VFf} - d_{VFf}\gamma_5) f \partial_\mu V_\nu + higher\ corrections. \qquad (3.7)$$

Where $\overline{F}$ and f are the wavefunctions of the excited and normal leptons respectively.

This assumes a magnetic moment type transition from ground to excited state which is necessary to conserve SU(2)×U(1) gauge invariance. Models which preserve this gauge invariance can be used to explain the observation that normal quarks and leptons are much lighter than the naive expectation that their masses be $\mathcal{O}(\Lambda_c)$. Also, such models do not exclude the possibility that excited states relatively light compared to the compositeness scale may exist [6, 23].

Λ is the characteristic scale of the interaction. Though it might be expected that Λ is of $\mathcal{O}(\Lambda_c)$ since if one has reached the energy scales at which the lepton is composite then obviously such interactions will occur, the current limits however [16] still allow the value to be a factor of approximately 10 smaller.

The parameters c_{VFf} and d_{VFf} represent the coupling constants of the boson field ($V = \gamma, Z$) to the excited and ordinary fermions. Several experimental bounds exist on the form of c and d, the most stringent coming from limits set on the magnitude of the electric dipole moment and anomalous magnetic moments of the electron and muon [24]. If either c or d had a sizeable imaginary component then one would observe a CP violating electric dipole moment, whereas there are stringent limits on this not being the case. Also, if either c or d were sizable compared to the other this would lead to an anomalous magnetic moment at order $\frac{m}{M}$, (mass(composite)/mass(constituent)), $\simeq \frac{4\alpha}{\pi}(|c|^2 - |d|^2)\frac{m}{M}$. Limits due to $(g-2)$ measurements imply, to a high degree of accuracy, that

$$|c_{VFf}| = |d_{VFf}|$$

These observations result in the restriction that only one helicity state of the excited electron can couple to its normal partner, thus the excited electron and neutrino, assumed to form the familiar weak doublet

$$L = \begin{pmatrix} \nu_{e^*} \\ e^* \end{pmatrix}$$

couple to the electron doublet

$$l_L = \begin{pmatrix} \nu_e \\ e \end{pmatrix}_L = \frac{1-\gamma_5}{2} \begin{pmatrix} \nu_e \\ e \end{pmatrix}$$

3.3 Production Cross Sections in ep Collisions

There are 3 distinct regions of phase space to be considered when deriving these expressions.

1) Elastic Region

This is elastic scattering off the proton where $W^2 = m_p^2$ and $q^2 = 2m_p\nu$ with no restrictions on Q^2 save the kinematical one and $x = 1$. The differential cross section (for γ exchange) is given by

$$\frac{d\sigma}{dQ^2} = \frac{\pi\alpha^2}{\Lambda^2}\frac{|c_{\gamma e^* e}|^2 + |d_{\gamma e^* e}|^2}{(s-m_p^2)^2 Q^2}\left\{G_M^2(Q^2)(2m_{e^*}^2 - Q^2)(m_{e^*}^2 + Q^2) + \frac{G_E^2(Q^2) + \frac{Q^2}{4m^2{}_p}G_M^2(Q^2)}{1+\frac{Q^2}{4m^2{}_p}}\right.$$
$$\left.\left[4(s-m_p^2)^2 - (m_{e^*}^2 + Q^2)\left(4s - Q^2 - 4m_p^2 + \frac{4m_{e^*}^2 m_p^2}{Q^2}\right)\right]\right\} \quad (3.8)$$

where G_E and G_M are the measured electric and magnetic form factors of the proton.

$$G_E(Q^2) \approx \frac{G_M(Q^2)}{2.79} \approx \left[1 + \frac{Q^2}{0.71\ GeV^2}\right]^{-2} \quad (3.9)$$

2) Low Q^2 region: ($Q^2 < Q_0^2$, $W^2 > (m_p + m_\pi)^2$)

This region is dominated by resonance scattering off the proton, i.e, the production of proton resonant states such as $\Delta(1236)$, $N^*(1520)$, $N^*(1688)$ and their subsequent decays to nucleon plus pion.

The expression for the differential cross section utilises the experimentally measured structure functions. The differential cross section due to photon exchange is then given by

$$\frac{d\sigma}{dx dQ^2} = \frac{2\pi\alpha^2}{\Lambda^2}\frac{|c_{\gamma e^* e}|^2 + |d_{\gamma e^* e}|^2}{(s-m_p{}^2)^2 x^2 Q^2}\cdot$$
$$F_2(x,Q^2)\left\{m_{e^*}^2(m_{e^*}^2 + Q^2)\left(\frac{1}{x} - \frac{2xm_p^2}{Q^2}\right) + 2x(s-m_p^2)^2 - 2(m_p^2 + Q^2)(s-m_p^2)\right\} \quad (3.10)$$

where $F_2(x,Q^2)$ is the proton structure function which basically parameterises the probability of finding a particular quark (antiquark) carrying a fraction x of the

proton's momentum when probed to a scale Q^2;

$$F_2(x,Q^2) = \sum_{q=u,d...} Q_q^2 . \left\{ xq(x,Q^2) + x\bar{q}(x,Q^2) \right\} \tag{3.11}$$

3) Deep Inelastic Region: $(Q^2 > Q_0^2\ ,\ W^2 > (m_p + m_\pi)^2)$

This is the region in Q^2 covered by perturbative QCD techniques and the parton model is valid, thus the integrated cross section is given by ;

$$\sigma(e^- p \to e^* X) = \int_{\hat{s}_{min}/s}^{1} dx \int_{Q_0^2}^{sx-m_{e^*}^2} dQ^2 \sum_q q(x,Q^2) \frac{d\hat{\sigma}}{dQ^2}(eq \to e^* q'; \hat{s} = sx) \tag{3.12}$$

$q(x,Q^2)$ - effective quark distribution.

$\frac{d\hat{\sigma}}{dQ^2 dx}$ - differential cross section.

where

$$\frac{d\hat{\sigma}}{dQ^2}(ep \to e^* q') = \frac{2\pi\alpha^2}{\hat{s}^2\Lambda^2} Q^2 \sum_{V,V'}$$

$$\left\{ \left[2\hat{s}^2 - (Q^2 + m_{e^*}^2)(2\hat{s} - m_{e^*}^2) \right] A_4 \pm m_{e^*}^2 (2\hat{s} - Q^2 - m_{e^*}^2) A_5 \right\} D_V(t) D_{V'}(t)^* \tag{3.13}$$

where the plus (minus) terms correspond to scattering off quarks (antiquarks) and the A_4, A_5 terms are functions of the coupling constants c and d and electroweak couplings (see [18]). $D_V(t)$ and $D_{V'}(t)^*$ represent the gauge fields and Q_0 the cutoff of several GeV^2 where the parton model is no longer valid.

3.4 Prospects for HERA

At HERA one has a 30 GeV electron beam colliding with a 820 GeV proton beam. Using equation 3.1 one obtains

$$\sqrt{s} \simeq 314\ GeV$$

Using the models and cross sections previously introduced Hagiwara et al. [18] derived the results shown in Figure 3.3 for single e^* production at HERA energies. The calculations used the quark distribution Set 1 of Duke and Owens [30] and the structure functions obtained by Brasse et al. [29]. The Q_0^2 cutoff used is 5 GeV^2 and $\Lambda = 1000GeV$

Two important observations can be made . Firstly, the low Q^2 resonance scattering and elastic dominance in the production. This t-channel enhancement is due to the massless photon exchange contribution [21]. Also, see Fig. 3.4, the magnitude of the production cross section is very dependent on the scale of the interaction Λ.

It can be concluded however that even with the relatively stringent requirement that $\Lambda \approx \mathcal{O}(\Lambda_c)$ the prospects of producing excited electrons at the HERA collider, should they exist in the not too exotic form discussed here, are very good. For an integrated luminosity of 100 pb^{-1} ($\equiv$ 1 year's design running) one might expect 10 200 GeV excited electrons to be produced.

3.4.1 The Decay $e^* \rightarrow e\gamma$

The aim of the work presented here is to investigate the prospects of setting new composite limits at HERA using the $e^* \rightarrow e\gamma$ decay process. The motivation is obvious. Because of the low Q^2 dominance to the production cross section such a decay will possess the highly distinctive signature of a high p_T ($\mathcal{O}(m_{e^*})$) electron-photon pair. The hadronic remnants will tend to be a negligibly scattered proton (elastic) or nucleon plus pion (quasi-elastic) final state, or a struck quark jet dominated by low-Q^2 processes in the case of deep inelastic production. Thus these events will be characterised by a large energy $e\gamma$ pair and very little else to be expected in a detector.

In the rest frame of the excited electron the decay angular distribution is of the form

$$\frac{d\Gamma}{d\cos\theta} \sim (1 + \cos\theta) \tag{3.14}$$

where θ is the angle of the decay electron in the e^* rest frame with respect to the incoming electron beam. The distribution is not uniform as one would usually expect for a spin $\frac{1}{2}$ particle because of the $\frac{1}{2}(1-\gamma_5)$ nature of the coupling of the e^* to vector field and normal electron.

At e^* masses greater than m_W one would would also expect a finite width for the decay to W and Z bosons. Here the branching ratios for the various electroweak gauge decay

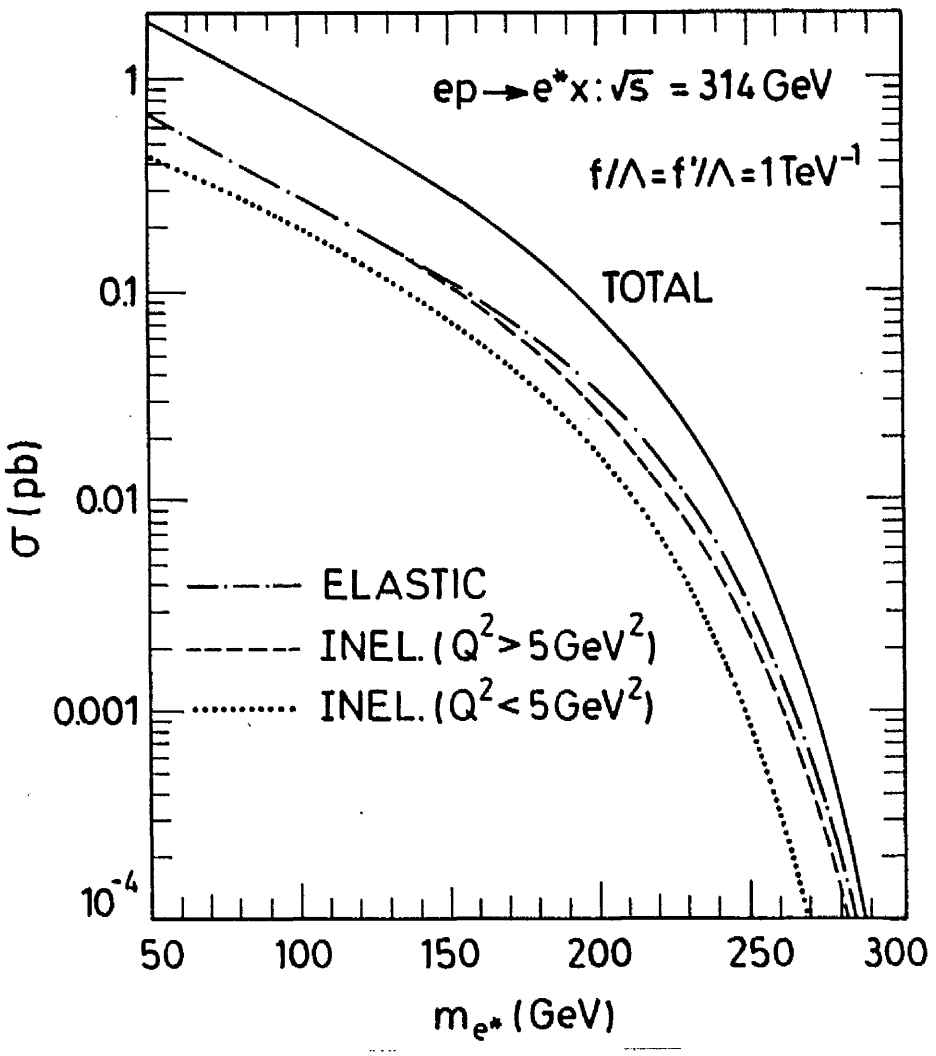

Figure 3.3: Total production cross section vs e^* mass in HERA ep collisions with magnetic transition couplings. ($c_{VFf} = d_{VFf} = \frac{1}{2}$)

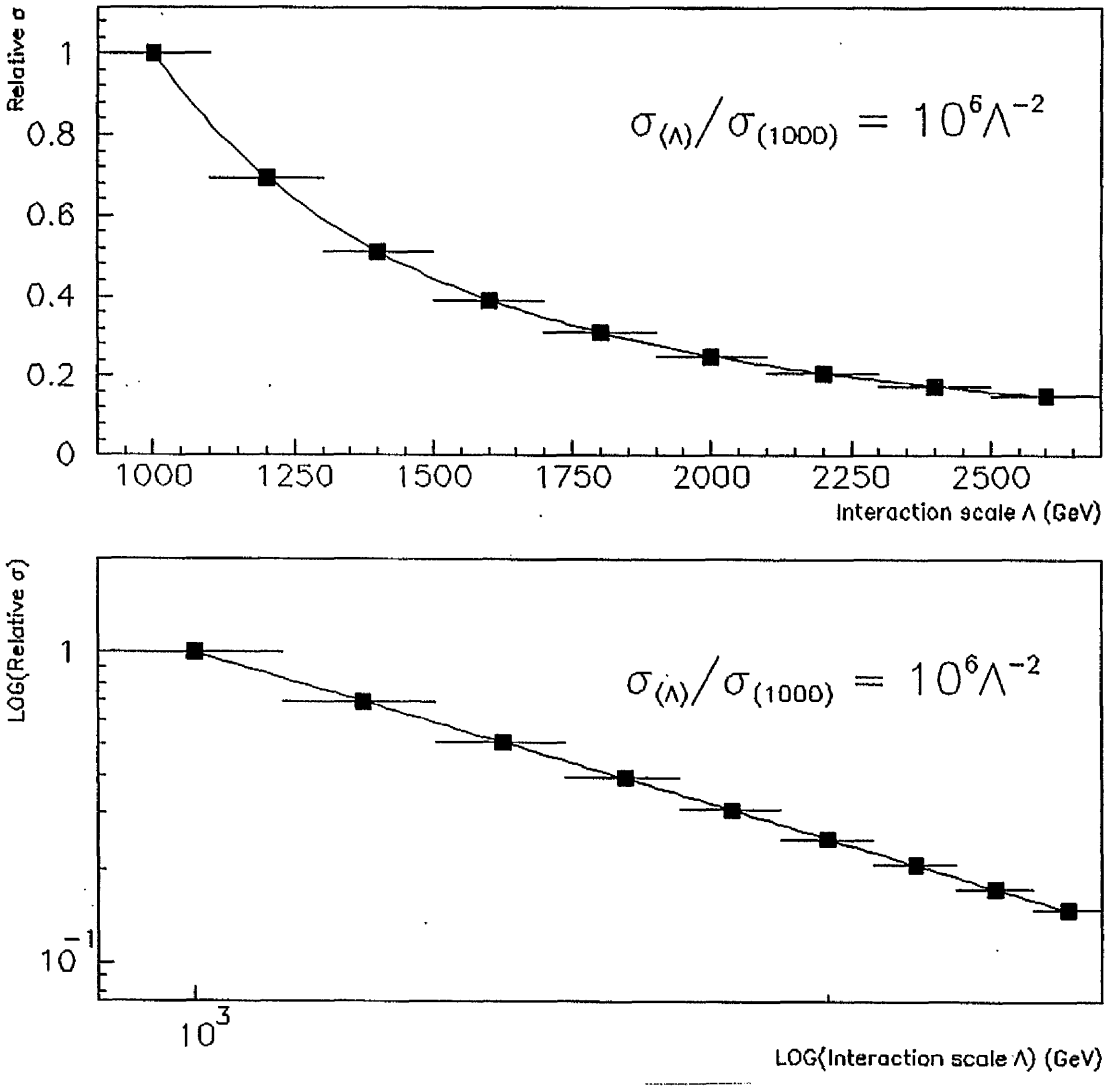

Figure 3.4: Relative e^* Production Cross Section as a function of scale of the interaction Λ.

channels given by [20] are used. The partial widths are

$$\Gamma(e^* \to e\gamma) = \frac{\alpha e_e^2}{4}\frac{m_{e^*}^3}{\Lambda^2} \tag{3.15}$$

$$\Gamma(e^* \to eZ^0) = \frac{\alpha\left[I_3^e - e_e \sin^2\theta_W\right]^2}{\sin^2 2\theta_W}\frac{m_{e^*}^3}{\Lambda^2}\left(1 - \frac{m_Z^2}{m_{e^*}^2}\right)^2\left(1 + \frac{m_Z^2}{2m_{e^*}^2}\right) \tag{3.16}$$

$$\Gamma(e^* \to \nu_e W^-) = \frac{\alpha}{8\sin^2\theta_W}\frac{m_{e^*}^3}{\Lambda^2}\left(1 - \frac{m_W^2}{m_{e^*}^2}\right)^2\left(1 + \frac{m_W^2}{2m_{e^*}^2}\right) \tag{3.17}$$

Decay mode	Fraction($\frac{\Gamma_i}{\Gamma}$)
e^+e^-	3.21 %
$\mu^+\mu^-$	3.36 %
$\tau^+\tau^-$	3.33 %
$\nu\bar{\nu}$	19.2 %
$e^\pm\mu^\mp$	< 2.2 %
hadrons	70.9 %

Table 3.1: Relative partial widths of Z^0 decay modes.

Decay mode	Fraction ($\frac{\Gamma_i}{\Gamma}$)
$e^-\bar{\nu}$	10.0 %
$e^-\bar{\nu}\gamma$	< 1.0 %
$\mu^-\bar{\nu}$	10.0 %
$\tau^-\bar{\nu}$	10.2 %

Table 3.2: Relative partial widths of W^- decay modes.

The resulting variation in branching ratio with e^* mass is shown in Figure 3.5.

Although the $e^* \to e\gamma$ process is no longer the dominant decay mode as e^* mass increases if one wants to study the eZ^0 and $\nu_e W^-$ decay products, the branching ratios of the Z^0 and W^- must also be considered (see Tables 3.2, 3.1) [12]. It can be readily seen from these figures that the branching ratios of Z and W bosons to anything as clean as a $e\gamma$ final state are such that $e^* \to e\gamma$ appears to remain the least problematic event signature to study.

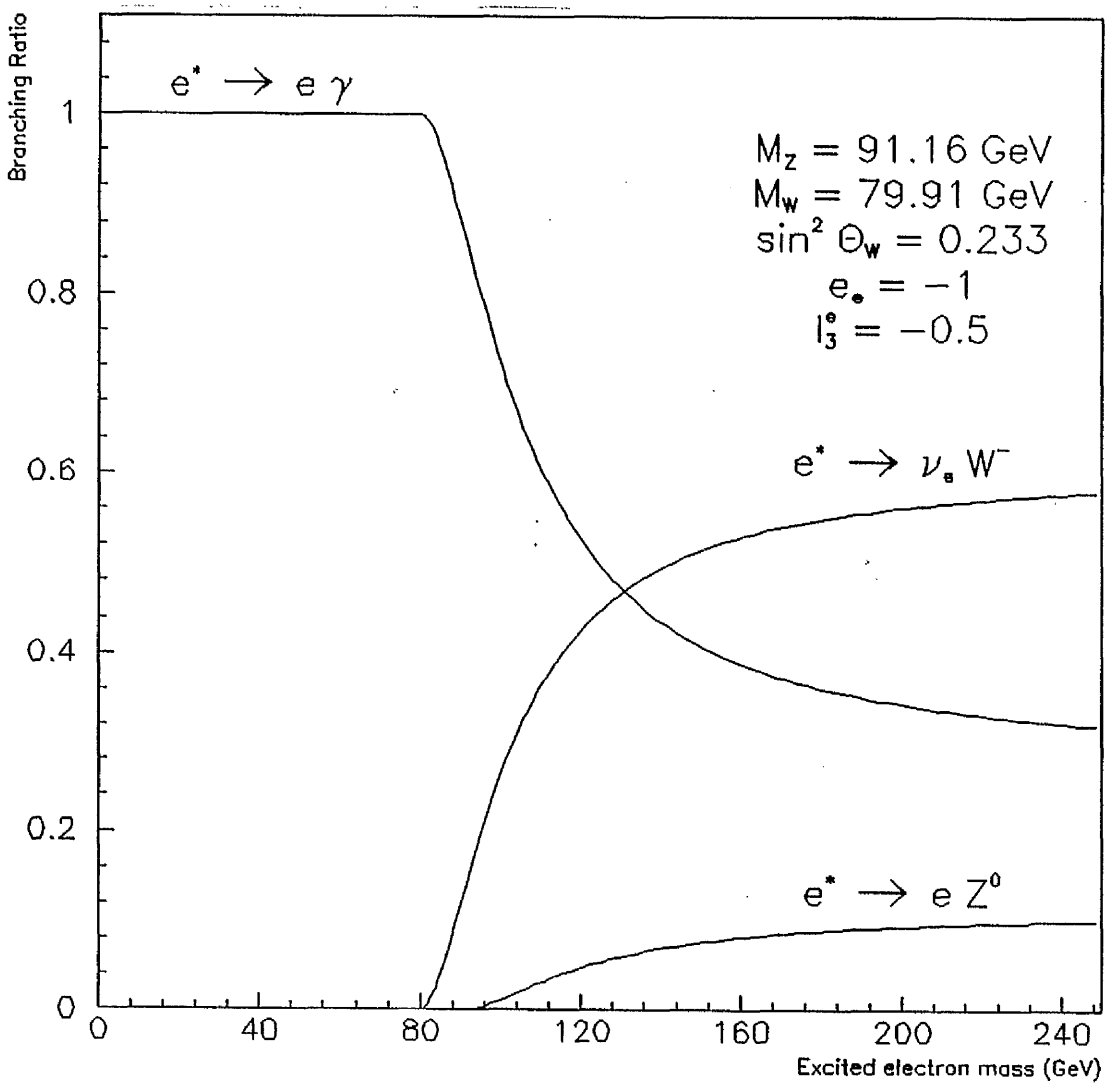

Figure 3.5: Branching ratios for the processes $e^* \to e\gamma$, $e^* \to eZ^0$ and $e^* \to \nu_e W^-$ as a function of e^* mass.

3.4.2 Background Processes

Processes which yield a candidate high p_T electron photon pair are the background sources to e^* physics at HERA.

There are two main event classes to be considered.

Deep Inelastic Neutral Current Scattering

This is in itself a major source of physics interest at HERA.

The generic form of neutral current DIS (see Figure 3.1) is

$$e + q \xrightarrow{\gamma, Z^0} e + X \tag{3.18}$$

where X represents the quark jet fragments.

Depending on the kinematics of the interaction [22] the scattered electron could well have a large p_T.

Decay photon candidates from the decay of short lived, high energy mesons at the interaction point are possible. For example, the decay $\pi^0 \rightarrow \gamma\gamma$ may give rise to a high energy photon candidate cluster since the opening angle between the decay products is so small in the lab, the energies are so much greater than m_{π^0}, that the overlapping photon showers in the calorimeter are indistinguishable from one produced by a single particle.

Thus the tails of DIS distributions could well be e^* candidate events.

Wide Angle Bremsstrahlung

This is a process of the form

$$e + p \rightarrow e + X + \gamma \tag{3.19}$$

The electron radiates a real photon in the presence of the accelerating electromagnetic field of the proton, the virtual electron so produced is brought back on mass shell by the absorbtion of a virtual photon radiated from the proton. These processes are illustrated in Figure 3.6 for both initial and final state bremsstrahlung.

The process can be visualized in terms of two q^2 components (Fig. 3.7) where q_1 represents the 4-momentum of the off mass shell electron state and q_2 the momentum

transfer of the virtual photon radiated by the proton. The cross section is dominated by $q_1,\ q_2 \rightarrow 0$ processes, high rate bremsstrahlung where the electron, photon and hadronic system remain in the beam-pipe. However should q_2 be large the photon remains in the beampipe while the electron, hadronic system emerge into the detector. This is known as *radiative corrections* and is important to understand in accurate structure function measurements since the 4-momentum of the electron has effectively been distorted in a non measurable way.

The situation of most interest for e^* studies is when q_1 becomes finite since the electron and photon are now emitted at wide angles while the proton remnant remains in the beampipe, this is wide angle bremsstrahlung or quasi real Compton since the rate is dominated by $q_2 \rightarrow 0$ processes.

These events are particularly important background since the off mass shell virtual electron state is kinematically indistinguishable from an s-channel excited electron. In e^+e^- colliders the equivalent events are known as radiative Bhabha.

. At HERA the proton beam introduces complications into the calculations since, because it is a composite body, there are effects due to anomalous magnetic moment, electromagnetic form factors and inelastic contributions which have to be taken into account in the cross section evaluations.

Thus, there are the same 3 phase space contributions to the quasi-real Compton cross-sections at HERA [28].

- Elastic - $ep \rightarrow ep\gamma$

  The proton is hardly deflected and the electron and photon come off at effectively 180° opening angle in the lab.

- Quasi-Elastic - $ep \rightarrow eX\gamma$, $(M_p + m_\pi) \leq W \leq 2\ GeV$

  The region is saturated by the low Q^2 production of the 3 resonances $\Delta(1236)$, $N^*(1520)$ and $N^*(1688)$. The subsequent decay to nucleon plus pion will be well contained in the beam-pipe and the final state observed in a detector is virtually the same as for the elastic case.

- Deep Inelastic - $ep \rightarrow eX\gamma$

The contribution to the full wide angle bremsstrahlung cross section from this source is very small compared with the previous two since the cross section falls off rapidly with W, the mass of the resulting hadronic system, for low Q^2 processes.

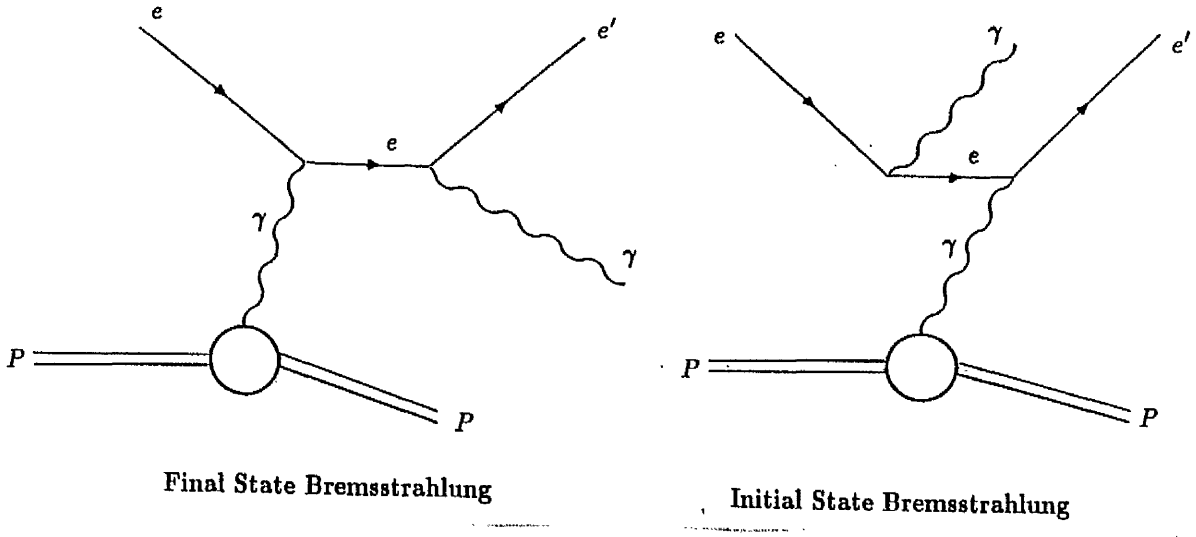

Figure 3.6: Bremsstrahlung processes at HERA.

There remains also the possibility that photoproduction and beam-wall, beam-gas events could be sources of background.

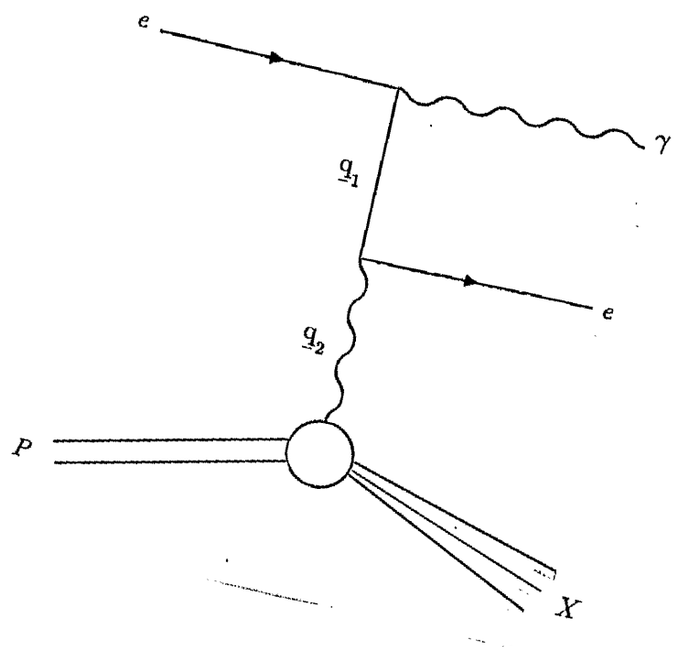

Figure 3.7: The two q^2 components of the bremsstrahlung process.

Chapter 4

HERA and the H1 detector

4.1 HERA

HERA (**H**adron **E**lectron **R**ing **A**ccelerator) is a 6.3 km collider built at DESY (Deutsches Elektronen Synchrotron) Hamburg. First collisions are expected in early 1992 [7].

The storage rings are mounted with the proton ring sitting above the electron ring in the same HERA tunnel. They accelerate electrons to 30 GeV and protons to 820 GeV. The beams are brought together in 3 straight regions for head-on collisions. The design luminosity is $1.5 \times 10^{31}\ cm^{-1}\ sec^{-1}$ per interaction point.

Because of the energy required for the proton beam the bending and focussing dipole and quadrapole magnets of the proton ring are superconducting and kept at liquid helium temperatures.

The injection scheme is shown in Figure 4.1 The proton production starts with the injection of negative hydrogen ions from LINAC IIIinto the proton synchrotron DESY III. Here the ions are stripped of the two electrons and the protons accelerated to 7.5 GeV before injection into PETRA II where they are taken up to 40 GeV. The HERA ring is filled by three injections of 40 GeV protons from PETRA II.

In one straight section of the HERA proton storage ring two r.f systems accelerate the protons to 820 GeV. During the injection period ($\approx$ 20 $mins$) two 52 MHz cavities act to reduce bunch length. Then four 208 MHz cavities are switched on which compress the bunches further and accelerate the beam from 40 GeV to 820 Gev in $\approx$ 10 $mins$.

Electrons are accelerated by the chain LINAC I (220 MeV),
DESY II (9 GeV) and finally PETRA II which injects electrons at 14 GeV into the HERA

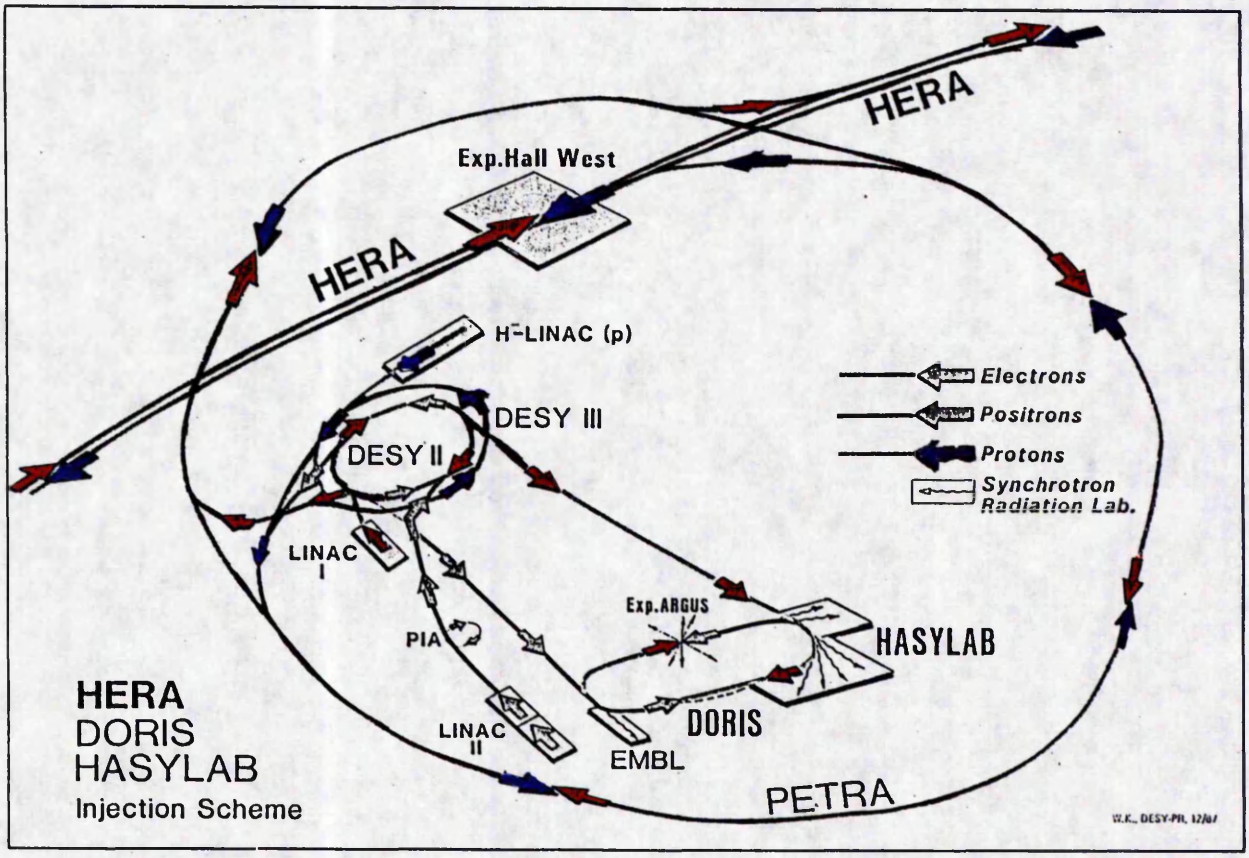

Figure 4.1: The Injector Chain for HERA

ring.

The electrons are then accelerated by means of 16 superconducting niobium r.f cavities and 82 normal conducting cavities, all operating at 500 MHz.

The three interaction regions are occupied by experimental halls. In two the major experiments H1 and ZEUS are installed.

4.2 Detector Design Considerations

With the physics considerations in mind, the detectors at HERA have to incorporate some common general features.

- A high degree of hermiticity is essential for the study of non-interacting particles such as neutrinos, the presence of which (as typified by an imbalance in detected transverse energy) is common in exotic physics processes. A neutrino is also present in all charged current deep inelastic scattering events.

- Excellent energy flow measurements are required. In particular for the inclusive cross section measurements for deep inelastic physics. Uncertainties in energy flow cause migration from x, Q^2 bins and thus affect the accuracy to which structure functions can be measured.

  Thus, energy resolution and granularity for all calorimeters must be optimised.

- Since much of the physics at HERA depends on the properties of the scattered electron, emphasis must be placed on electron identification and energy resolution.

- Muon identification is important in the consideration of good detector hermicity.

  The presence of muons, which are unlikely to be contained by calorimetry since the production of electromagnetic showers is inversely related to the mass of the particle ($m_\mu \approx 200 m_e$), characterizes many postulated new physics processes and heavy flavour physics, for example the b quark decay, $b \xrightarrow{W^-} c + \nu_\mu + \mu^-$.

- Finally, the design has to take into account the unusual feature of HERA among other colliders in that the laboratory frame is *not* the rest frame of the collisions.

  Because of the large energy imbalance in the proton direction, most of the particles produced will be forward going in the lab.

Therefore, it is essential that highly accurate tracking and calorimetry is available in the forward (proton direction) region of the detector if individual tracks are to be resolved in high multiplicity jets of particles.

4.3 The H1 Detector

The experiment designed to meet these requirements by the H1 Collaboration is shown in Figures 4.2 and 4.3. [8, 9]

4.3.1 The Superconducting Solenoid

Essential to particle identification is the presence of an axial magnetic field since this provides charge determination (direction of curvature in the field), and momentum measurements. The momentum component perpendicular to $\vec{B}$ is given by

$$p_T = 0.3BQR. \tag{4.1}$$

B - magnitude of field in $Tesla$

Q - signed Charge

R - radius of curvature of track in m

When used in conjunction with the accurate coordinate measurements from the tracking devices this can be used to define the entire momentum vector.

The field is maintained by means of a solenoid located outside the calorimetry and tracking. This minimizes the amount of material a particle traverses before accurate energy measurements are carried out in the calorimeter. Since tracker performance at HERA energies requires a large uniform magnetic field in the tracker volume, a superconducting solenoid is used.

This maintains an average axial field of 1.2 T in the tracker volume. The homogeneity of the field is $\Delta B_z < \pm 3\%$ over the region.

The coil is wound directly inside an aluminium alloy cylinder. Pipes around this cylinder cool the coil by the circulation of 2-phase Helium. The arrangement and its associated insulation is contained in a stainless steel vacuum vessel.

In order to achieve $\int B.dl \approx 0$ along the beam axis a compensating magnet is required.

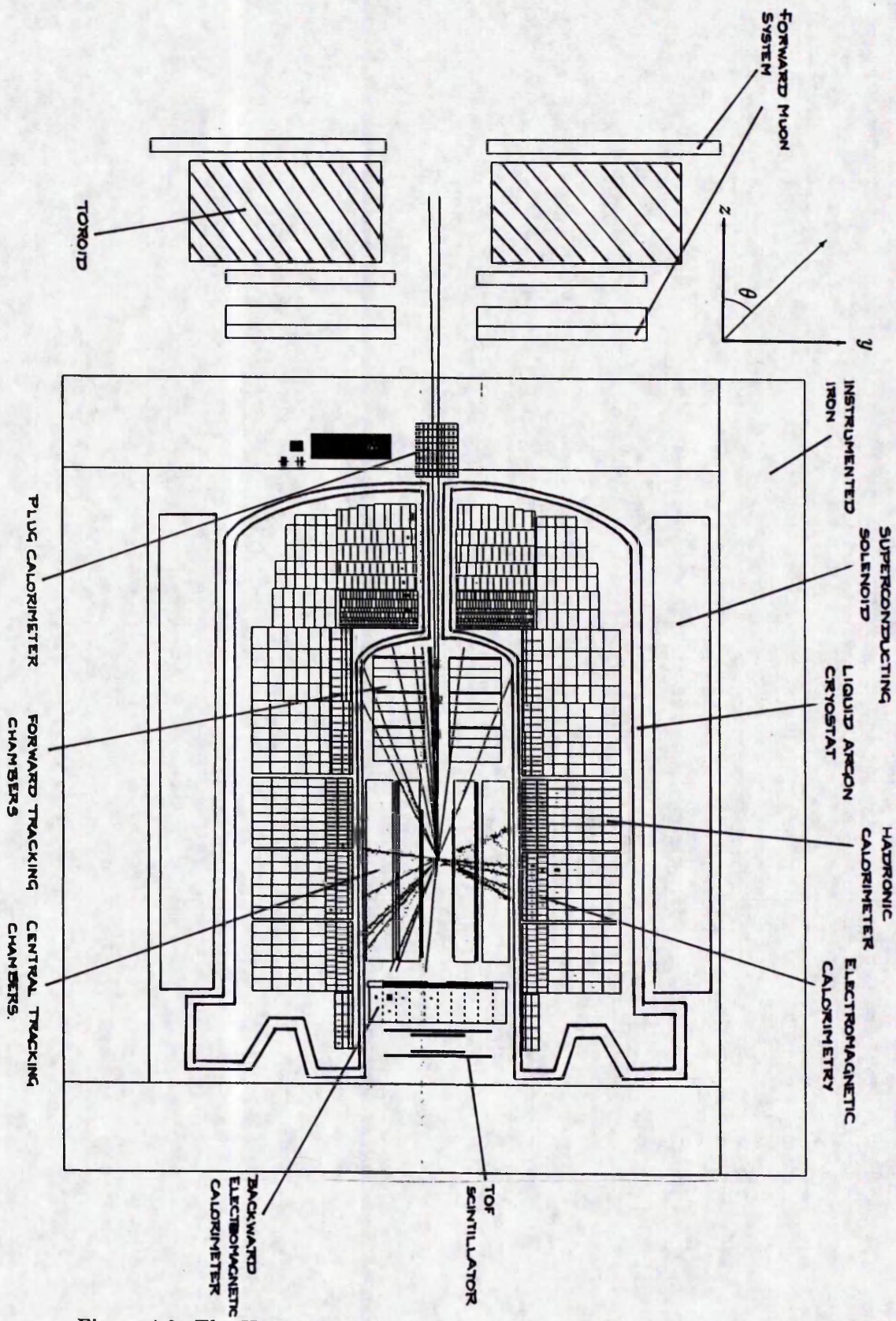

Figure 4.2: The H1 Detector shown side on with a vertical cut along the beam.

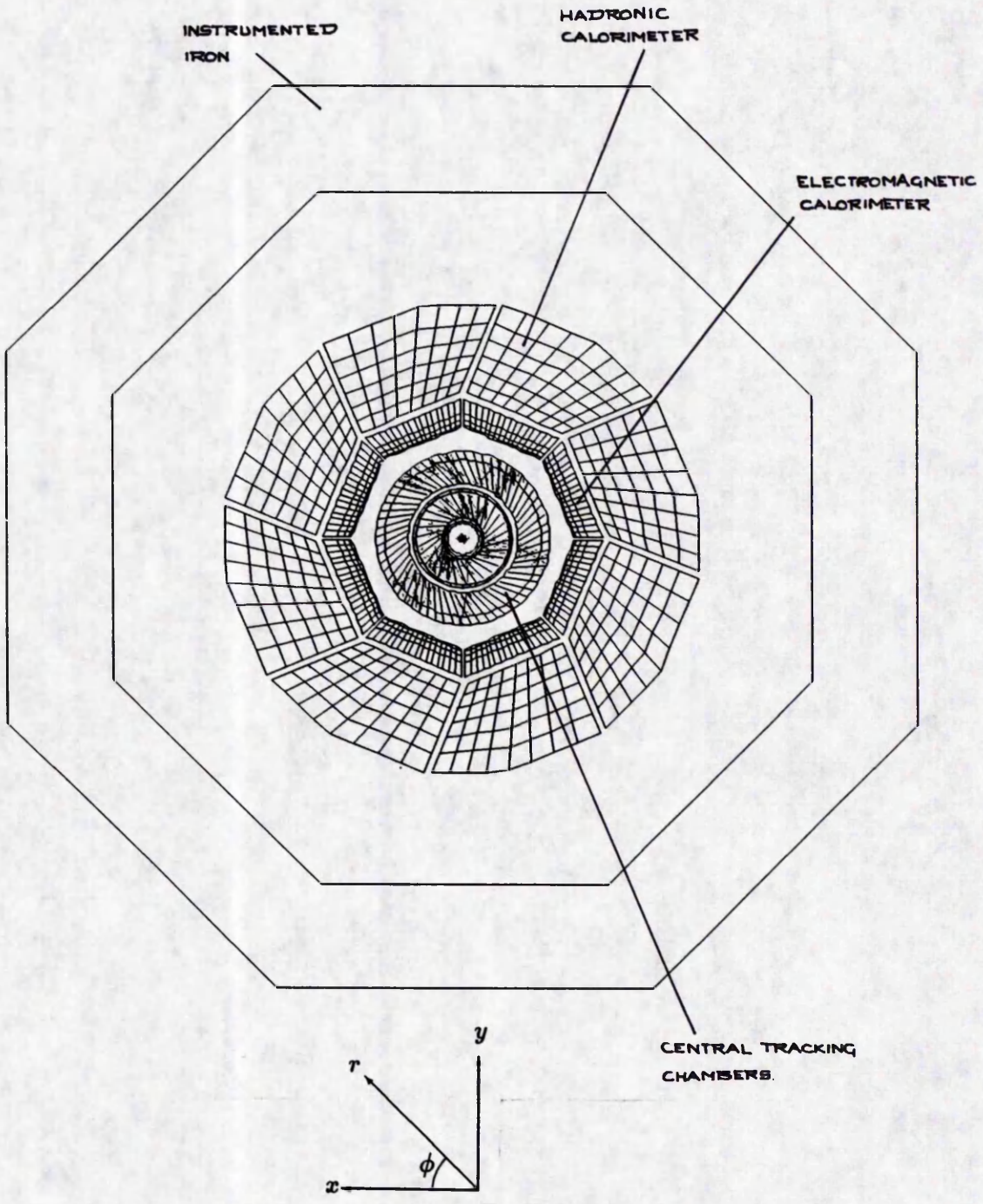

Figure 4.3: The H1 Detector shown end on with a vertical cut transverse to the beam

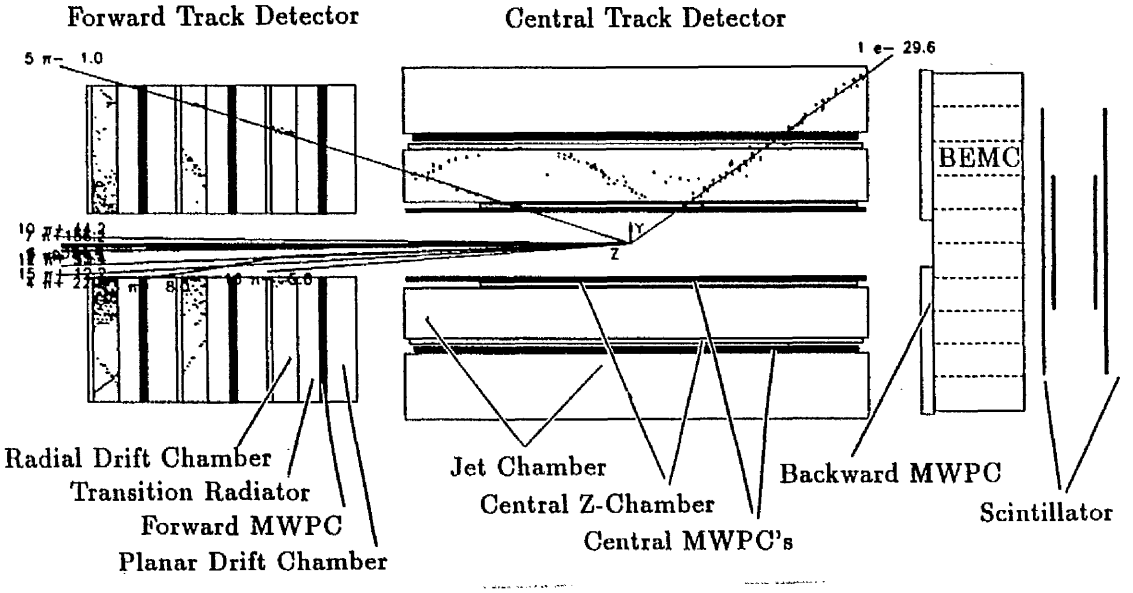

Figure 4.4: The H1 Tracking System

4.3.2 Tracking

The main aims of the H1 tracking arrangement are;

- Good momentum and multi-track resolution.
- Improvement of calorimeter e/π discrimination by incorporation of electron identification capabilities.
- The provision of fast triggering capabilities.

An important class of events studied at HERA is high Q^2, x deep inelastic scattering since this extends into a previously unattained momentum transfer regime. Event kinematics at HERA are such that most jet particles are going to be found at polar angles $< 30°$ due to the boost quark fragments receive in the proton direction. In order that tracking performance is not degraded in this region of high track density the H1 tracking is divided into separate central and forward tracking detectors (see Figure 4.4) with more emphasis placed on jet resolution in the design of the latter.

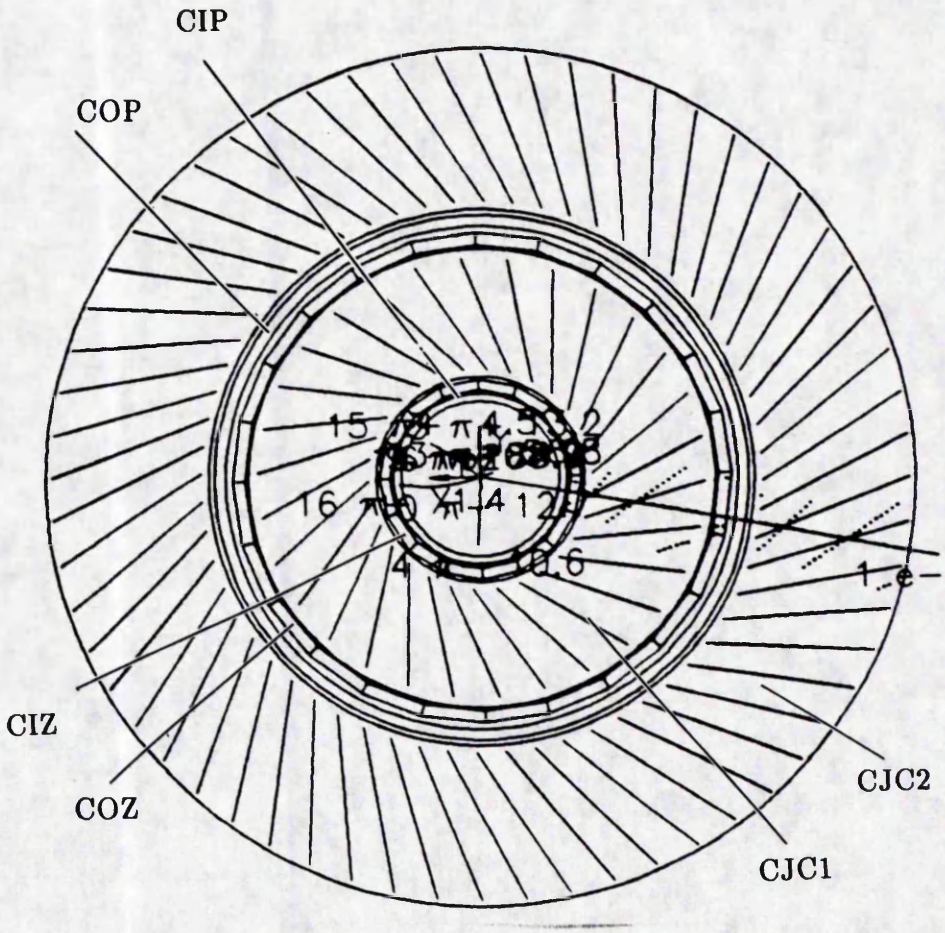

Figure 4.5: Profile of the Central Tracker showing the cell structure and Supercells in the CJC.

The Central Tracking Detector

The tasks of accurate drift measurement of $r\phi$ for charge and momentum determination, and z for θ measurements of event topologies and kinematics, are separated in the central tracker.

Accurate $r\phi$ is provided by the Central Jet Chamber (CJC). This is a cylindrical drift chamber around the beam axis with the sense wires running parallel to the beam in two so called superlayers of cells (see Figure 4.5) to form the CJC1 and CJC2 chambers.

The planes of the cells are tilted by $\approx 30°$ with respect to the radial direction so even the stiffest ($p_T > 2\ GeV$) tracks traverse a sense plane about 5 times. This results in a relatively simple determination of t_0 as well as drift velocity and Lorentz angle for

calibration purposes.

The sense wires are read out at both ends for a charge division measurement of z and dE/dx for lepton identification.

Located radially before CJC1 and between CJC1 and CJC2 are the inner and outer z-chambers respectively. These are drift chambers with the sense wires stretched perpendicular to the beam-pipe in a polygon around a cylinder, providing accurate z measurement by drift distance.

The inner z-chamber (CIZ) consists of 16 azimuthal sectors, 4 sense wires deep in r and 15 cells in the z direction. The outer z-chamber (COZ) consists of 24 drift cells, 4 sense wires deep. Both sets of sense wires are read out independently at each end for charge division measurements.

The Forward Tracker

The design of the forward tracker aims to optimise several functions of the detector in this important region.

It uses two designs of drift chamber, radial and planar, to solve the difficult problem of pattern recognition and to achieve good momentum and angular resolution of tracks, at their densest in this region. Electron identification is made possible by transition radiators. When a charged particle crosses an interface between materials with different dielectric or magnetic properties the associated electric field has to change and the resulting redistribution of charge in the material gives rise to transition radiation, primarily in the form of X-rays. The properties of the radiation emitted such as the total energy or width of the distribution can be used to distinguish electrons and hadrons. The emitted X-rays then pass into the radial chambers where they are detected and used in the e/π discrimination process.

The tracker is constructed from 3 identical *supermodules*. Each supermodule contains one planar module, followed by a MWPC plane, transition radiator and finally a radial module, i.e 3 $\times$ (P + MWPC + TR + R). For good track linking between the forward and central tracker it is important to have good space-point resolution at the face of the forward tracker closest to the interaction point. Thus a planar comes first. The MWPC's come next to optimise the geometric trigger efficiency, followed by the transition radiator-radial configuration.

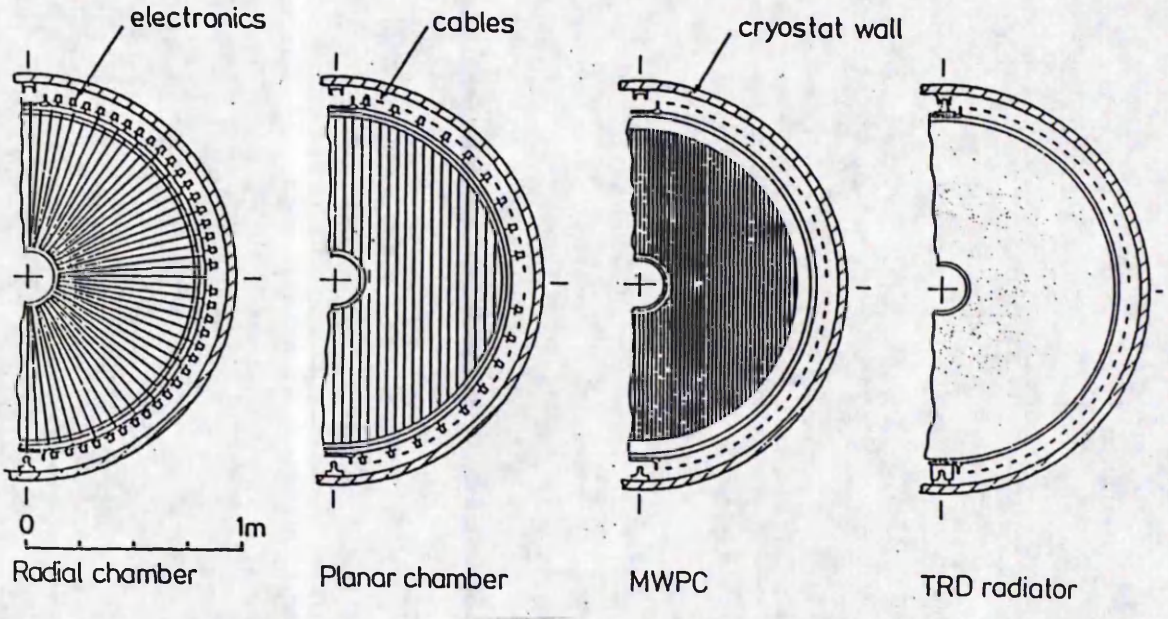

Figure 4.6: Axial view of one wire plane of the components in a supermodule.

Multiwire proportional chambers (MWPC's) provide beam crossing information and triggers (see Figure 4.6).

The radial chambers have sense wires radiating outward from the beam-pipe and consist of 48 ϕ cells or wedges. Drift times can be used to derive accurate azimuthal angle if r is known accurately. Rough r is available from charge division. Each module is twelve sense wires deep in z which aids the pattern recognition while the accurate measurement of the variation of ϕ with z over the full extent of the forward tracker provides precise momentum measurements using track curvature in the magnetic field. The design also has the advantage of having the smallest drift cell size where the beam-wall, synchrotron background will be highest close to the beam-pipe.

However, a more accurate r is required if one is to use drift times to define ϕ well. Also, if hits are registered in only 2 of the 3 radial chambers positioned at increasing z over the forward tracking region accurate momentum measurements are not possible. Therefore planar chambers are included.

Each planar module consists of 3 drift chambers. Each chamber consists of 32 parallel

drift cells (Figure 4.6) 4 sense wires deep. Adjacent chambers in each module are oriented at 60° with respect to one another. This results in good θ measurement by drift time and therefore momentum, r and z-vertex information. The wires are readout at one end only.

Polypropylene transition radiators are located on the face of each radial chamber closest to the interaction region. The radial chambers are used detect the X-rays emitted by charged particles as they pass through the radiator.

The Trigger Proportional Chambers

Associated with the tracking system are several MWPC's. In the forward and central regions these chambers are not read out wire by wire to assist in the reconstruction of an event but by pads which provide fast trigger readout and are segmented in a such a way as to form *rays* emanating from the interaction region. Their purpose is threefold.

1. Vertex reconstruction along the beam axis to discriminate beam-wall and beam-gas backgrounds.

2. Provision of a topological track trigger for low multiplicity events using the ray readout segmentation.

3. Independent determination of bunch crossing time t_0

In the central region there are 2 cylindrical MWPC's both consisting of a double layer of sense wires running parallel to the beam-line. Inside CJC1 and the CIZ is the Central Inner Proportional Chamber (CIP), while radially between CJC2 and the COZ is the Central Outer Proportional Chamber (COP). The chambers are read out by $z\phi$ cathode pads perpendicular to the beam-line to provide a fast z-vertex trigger based on 'roads' emanating from the interaction region.

In the forward region there are 3 sets of MWPC's, one in each supermodule (Figure 4.6). Each chamber consists of a double layer of sense wires (spacing 4 mm) with wires in adjacent layers offset by half a drift cell to provide a maximum drift time of 50 ns. This time resolution is enough to uniquely associate the track to its the beam crossing. An $r\phi$ pad readout extends the fast z-vertex trigger to the forward region.

In the backward region the Backward Proportional Chamber is located, similar to the forward MWPC's, but with 4 wire planes oriented at 45° with respect to each other. This

Detector	Component	Design Resolution
Central Tracker ($35° \leq \theta \leq 145°$)	Central Jet Chamber	$\sigma_{r\phi} = 100\ \mu m$ $\sigma_z = 24\ mm$ $\sigma_{\frac{dE}{dx}} = 6\%$ $\sigma_{two-track} = 2.5\ mm$
	Central Z Chambers	$\sigma_z \leq 350\ \mu m$ $\sigma_{r\phi}(CIZ) = 10\ mm$ $\sigma_{r\phi}(COZ) = 25\ mm$ $\sigma_{two-track} \approx 3.5\ mm$
Forward Tracker ($5° \leq \theta \leq 25°$)	3× Supermodule Configuration	$\frac{\sigma_p}{p} \leq 0.003p$ $\sigma_{\theta\phi} \leq 1\ mrad$
Backward ($152° \leq \theta \leq 175°$)	2× MWPC's	$\sigma_{space-point} = 2\ mm$

Table 4.1: Performance Parameters of the H1 Tracking System

forms the backward tracking detector. Wire readout allows accurate x and y coordinate measurement to measure charged particles, mainly single electrons from the high rate low x, Q^2 deep inelastic scattering events. These chambers also form part of the track trigger with the central and forward MWPC's.

The resolutions of the tracking system can be found in Table (4.1)

Scintillation Counters

Between the backward electromagnetic calorimeter and the iron structure is a double layer of scintillator walls. Their function is to provide a veto trigger based on time-of-flight (TOF) information. Photomultiplier readout provides the necessary time resolution.

4.3.3 Calorimetry

Energy measurement at H1 is conducted by sampling calorimeters, devices which periodically sample the development of showers. Absorbers which enhance the showering process are sandwiched with active regions which sample the energy loss between. The sampling

calorimeters are of two types, electromagnetic and hadronic, the construction differing due to the different production mechanisms and characteristics of the initiated showers.

An electromagnetic shower is the result of bremsstrahlung and pair production interactions within a material. High energy electrons will undergo bremsstrahlung processes on passage through material, the photons so produced are most likely to undergo pair production at high energies and thus there is a proliferation of electromagnetic particles (shower). Once the energy of these particles falls below a certain critical value ionisation losses become the dominant source of energy dissipation and the showering ceases. The important parameter to consider here is the radiation length of a material $X_{\mathbf{rad}}$, that is the distance over which a high energy electron loses all but a factor e of its energy through bremsstrahlung processes. The longitudinal development of an electromagnetic shower scales with $X_{\mathbf{rad}}$. The rate of energy loss as a function of $X_{\mathbf{rad}}$ rises until $\approx 5X_{\mathbf{rad}}$, reflecting the increasing number of shower particles, after which it falls rapidly as energy falls below that at which ionisation becomes dominant. So an electromagnetic shower is contained within approximately $20X_{\mathbf{rad}}$. Since radiation length is roughly proportional to $\frac{1}{Z^2}$ where Z is the atomic number of the traversed material, an electromagnetic shower is best contained by an absorber with high Z. The number of shower particles after a given radiation length is a function of the energy of the primary particle as is the longitudinal development of the shower.

Hadronic energy loss on traversing a medium is a more complicated matter. About half the incident energy is passed to fast secondaries which go on to have further interactions, some goes into nuclear production of π^0's which decay to $\gamma\gamma$ and initiate electromagnetic showers and some into nuclear binding energy and neutrino production when breaking up nucleii. The longitudinal development of a hadronic shower scales with $\lambda_{\mathbf{int}}$, the nuclear interaction length. For high Z absorbers $\lambda_{\mathbf{int}}$ is of order 10's larger than $X_{\mathbf{rad}}$. Because the showering mechanism is different to the electromagnetic case the rate of energy loss for a hadron initiated shower decreases with increasing $\lambda_{\mathbf{int}}$ from the very start of the shower which can be contained in $\approx 7\lambda_{\mathbf{int}}$. Resolution of hadronic calorimeters is subject to all the same considerations as electromagnetic but there is also the significant, $\approx 20\%$, energy loss due to undetectable nuclear binding energy and neutrino production. Therefore, for a given active material the scaling factors used to convert ionisation to energy values are different for electromagnetic and hadronic initiated showers and the electromagnetic component of

Region	θ coverage	Electromagnetic Calorimetry	Hadronic Calorimetry
Forward	$4° < \theta < 20°$	Liquid Argon Lead Absorber	Liquid Argon Steel Absorber
Central	$20° < \theta < 150°$	Liquid Argon Lead Absorber	Liquid Argon Steel Absorber
Backward	$152° < \theta < 176°$	Pb/Scintillator Sandwich with photodiode readout	-
Very Forward	$12.5\ mrad \leq \theta \leq 60\ mrad$	-	Cu sandwiched with Si detectors.

Table 4.2: The H1 Calorimetry

hadronic showers resulting from π^0 decays must be identified and scaled separately. This is the problem of calorimeter compensation. The solution adopted by the H1 experiment is an online software compensation technique based on fine longitudinal segmentation of the calorimeter. Because of the small size of $X_{\mathbf{rad}}$ relative to $\lambda_{\mathbf{int}}$ for a given absorber, the electromagnetic component is distinguishable as a large energy deposition over a small traversed $\lambda_{\mathbf{int}}$. Any such candidates are scaled by a different calibration constant and then summed with the hadronic component over both calorimeters to yield a final energy measurement.

Hadrons generally deposit most of their energy in the hadronic calorimeter and are thus distinguishable from electrons. However, there is a long tail to the energy deposition distribution in the electromagnetic calorimeter corresponding to the situation where an interaction produces a π^0 which undergoes an electromagnetic decay. There is a small probability that the interaction takes place at the very beginning of the calorimeter in which case this is not possible and one has the situation of a pion being mis-identified as an electron.

The H1 calorimetry is based on a large liquid argon (LAr) calorimeter, backed up by an iron tail catcher and complemented by a warm electromagnetic backward calorimeter and a very forward plug calorimeter (Table 4.2)

Hadronic energy leakage out of the calorimeter is tagged and measured by the iron tail catcher.

The plug calorimeter in the very forward direction reduces energy leakage through the beam-hole as much as possible.

The LAr Calorimetry

Liquid argon calorimeters have advantages for stable long term operation and simple calibration. The response is homogenous for all detector elements and is very stable with time. Fine granularity and detailed longitudinal segmentation can be achieved and need only be limited by the number of electronic channels available to the readout system. LAr calorimeters are therefore well suited to e/π separation and energy flow measurements.

The LAr system consists of electromagnetic and hadronic calorimetry in the forward and central regions of the detector.

The basic unit of the calorimeter structure is the stack (Figure 4.7), the size of which is limited by the acceptable tolerances on absorber and active region thickness dictated by required energy resolutions. A typical stack comprises 2.4 mm lead absorber plates in the electromagnetic part, 12 mm stainless steel plates in the hadronic part with gaps for active LAr and readout between.

The stacks are assembled into 8-fold segmented rings (wheels) of calorimeter which sit around, and in front of, the tracker and beam-pipe. All LAr wheels share a common cryostat to improve hermiticity and reduce conversions and scattering of particles in the cryostat walls.

The orientation of the absorber plates is such that the incidence of a particle coming from the interaction point is as close as possible to the normal and not more than 45° since energy resolution is degraded as incidence moves away from 90°. Thus the plates are vertical in the forward direction, forward barrel part and backward barrel part, and horizontal in the central barrel part. These zones correspond to physically separated rings of stacks.

The containment of this system varies from $20 - 30$ $X_{\mathbf{rad}}$ for the electromagnetic calorimetry and from $4 - 9$ $\lambda_{\mathbf{int}}$ for the hadron calorimetry, the exact numbers in each region dependant on the maximum energy expected.

Particles traversing the LAr gap ionize it and the generated free charge carriers are separated and collected by a high voltage maintained across the gap (up to 3 kV). The charge signal is generated by electrons drifting to the anode and collected onto pad read-

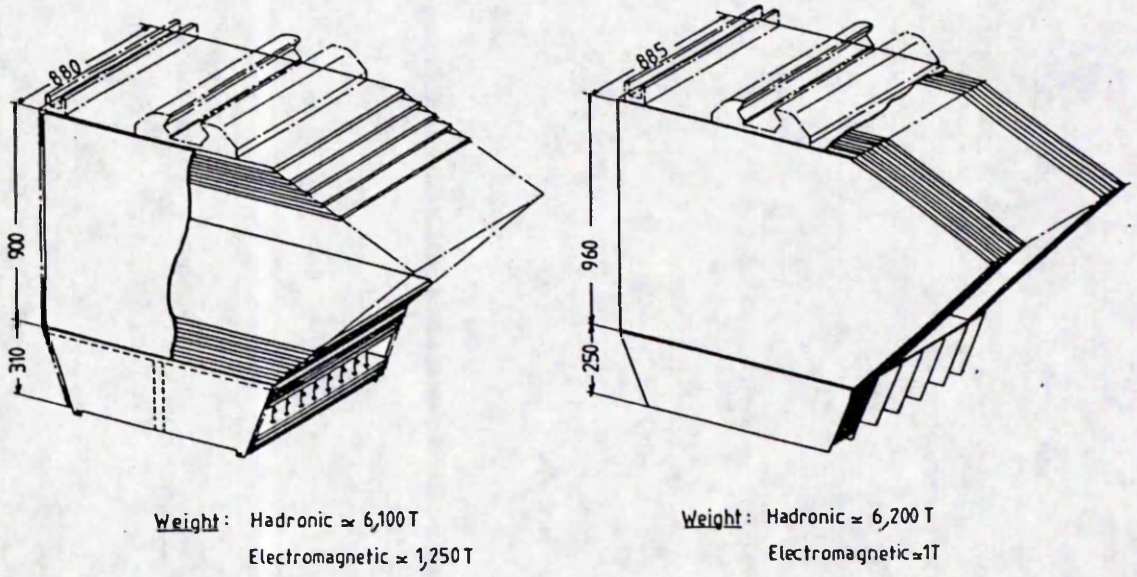

Figure 4.7: LAr stacks from the barrel region showing horizontal and vertical plate orientation

out structures. For good particle identification and e/π discrimination fine granularity of readout is necessary to discern the different longitudinal and transverse shower developments which distinguish the different particles. The pads are independent units inserted into the gaps between the absorber plates. The basic dimensions are $\approx 2 \times$ the Molière radius (4.3 cm) for the electromagnetic pads, doubled for the hadronic pads. Twice the Molière radius being a measure of the lateral distance out from the centre of a shower within which one expects 95% of shower particles to be contained.

The readout system associates sets of pads to form projective towers in ϕ and pseudo-projective towers in θ (Figure 4.8). It is also segmented longitudinally for e/π discrimination.

Backward Calorimeter

This is a lead/scintillator sandwich of, apart from a few edge towers, identical square towers. The plate orientation is vertical and each square is read out symmetrically at all four sides by wavelength shifter (WLS) bars.

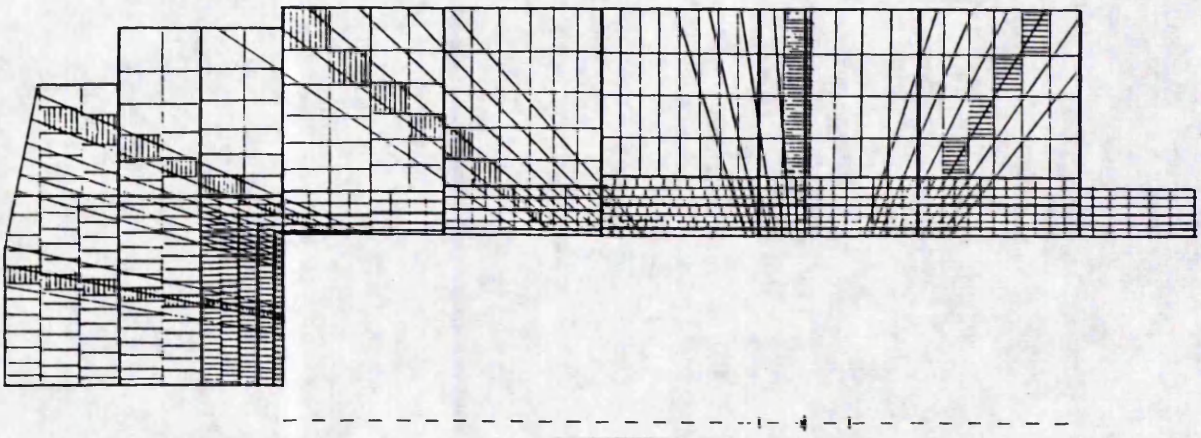

Figure 4.8: Longitudinal and transverse tower segmentation in the LAr calorimetry. The shaded areas show the pads which are grouped together in readout to form pseudo projective towers. The thicker lines represent the longitudinal segmentation in the electromagnetic calorimeter.

The resolution expected is

$$\frac{\sigma_{E_e}}{E_e} = \frac{13\%}{\sqrt{E}} + 1\%$$

Plug Calorimeter

This covers the angular region

$$12.5\ mrad \leq \theta \leq 60\ mrad$$

and consists of square towers of copper absorber sandwiched with silicon detectors. The purpose of the calorimeter is to minimise the missing transverse energy due to hadrons emitted close to the beam hole, therefore the design maximises angular resolution

$$\sigma_\theta < 5\ mrad$$

Electromagnetic Energy Resolution	$\frac{\sigma}{E} < \frac{10\%}{\sqrt{E}} (\theta < 152°)$
Hadronic Energy Resolution	$\frac{\sigma}{E} \approx \frac{55\%}{\sqrt{E}} (\theta < 120°)$
Angular resolution of jet directions	$< 10\ mrad (\theta < 20°)$
e/π rejection	$\leq 10^{-3}$

Table 4.3: Design Resolutions of the LAr Calorimetry

while retaining a moderate energy resolution

$$\frac{\sigma}{E} = \frac{100\%}{\sqrt{E_h}}.$$

4.3.4 Iron Structure and Magnetic Field

The iron structure around the superconducting solenoid serves as a flux return for the magnetic field and provides the absorber material for the tail catcher calorimetry and for muon identification.

The structure is divided into 3 sections, the base plate which carries the solenoid, LAr calorimeter and trackers, and two barrel structures with end plates.

For the purposes of calorimetry and muon identification the iron is laminated. In these gaps streamer chambers are placed.

4.3.5 Iron Instrumentation and Muon Detection

The limited streamer tubes form two components;

1. Muon Chambers.

   High energy muons will always reach the muon chambers. Momentum measurements can be made by the precise determination of track coordinates to yield the magnitude of track curvature in the magnetic field inside the yoke and along the beam direction.

   Muon detection is carried out by 3(2) double layers of streamer tube chambers in the region $25° < \theta < 130°$ ($5° < \theta < 25°$).

   In the barrel region the double layers are located in front of the iron, at 30 *cm* iron depth and between the yoke and the outer concrete shielding. The chambers are oriented parallel to the beam-line. In the endcaps the tubes are oriented vertically. There is no double layer outside the yoke since this region is covered by the forward muon detector.

2. Tail catcher calorimetry.

   The energy of high momentum hadrons leaking out of the back of the hadron calorimeter is longitudinally sampled using pulse height information of 3-fold longitudinally segmented towers and pad readout. 11 single 18 *mm* layers of chambers are inserted between 10 7.5 *cm* sampling layers of iron. The readout structure forms an extension of the calorimeter tower structure.

Drift distances	$\sigma_{drift} \leq 250\mu m$
Momentum	$0.23 \quad (25\ GeV/c) \leq \frac{\sigma_p}{p} \leq 0.32 \quad (150\ GeV/c)$
Position	$\sigma_{\theta,\phi} \leq 0.5\ mrad$

Table 4.4: Design Resolutions of the Forward Muon System

The expected hadronic energy resolution is

$$\frac{\sigma_E}{E} \sim \frac{110\%}{\sqrt{E}}$$

This is a tolerable figure given the small fraction of hadronic energy which leaks out of the liquid Argon.

The Forward Muon Detector

In the extreme forward direction muon momenta are expected to be high and no longer accurately measurable by the central tracker and instrumented iron since track curvature in the solenoidal field is slight. Therefore a forward muon spectrometer has been constructed to cover production angles $3° < \theta < 17°$.

This consists of 6 layers of drift chamber located on either side of an iron toroid bending magnet 1.2 m long, providing a field strength of 1.5 T. In 4 chambers (Θ chambers) the drift direction is radial to provide accurate θ and therefore momentum measurement. In the other 2 (Φ chambers) the drift direction is azimuthal for accurate ϕ measurement. The resolutions of the apparatus are summarised in Table 4.4.

4.3.6 Trigger

Most of the interactions expected are not beam-beam physics, but background interactions due to synchrotron radiation from the electron beam, beam-gas collisions, off momentum beam-wall collisions and cosmics. The very high beam currents and small ep cross sections at HERA accentuate the problem.

Table 4.5 illustrates some estimated rates for interesting events. The expected rate of neutral current deep inelastic physics is at best $3Hz$. This can be compared with the estimated background rates in Table 4.6, e.g, $9 \times 10^3\ s^{-1}m^{-1}$ for beam-residual gas interactions. It is clear that background, low Q^2 DIS and photoproduction events rather than the more interesting physics will be the dominant source of triggers at H1.

Process	Cuts	Rate (Hz)	Rate per bunch crossing
NC	$Q^2 \geq 3$ GeV^2	3	3×10^{-7}
	$Q^2 \geq 5000$ GeV^2	10^{-4}	10^{-11}
CC	$Q^2 All$	3×10^{-3}	3×10^{-10}
	$Q^2 \geq 5000$ GeV^2	5×10^{-4}	5×10^{-11}
Photo– production	All	10^3	10^{-4}
	$Visible$	10^2	10^{-5}
	$\Theta_{jet} \geq 5.7°$, $E_{jet} \geq 10$	1	10^{-7}
$ep \rightarrow ep + e + e-$	$W_{e^+e^-} \geq 1$		
	$\Theta(e^+, e^-) \geq 2.6°$	0.14	1.4×10^{-8}
	$\Theta(e^+, e^-) \geq 30°$	8.0×10^{-3}	8.0×10^{-10}
$ep \rightarrow ep + \gamma$	$8° \leq \Theta(e, \gamma) \leq 172°$	4.3×10^{-3}	4.3×10^{-10}
$ep \rightarrow ep + \rho$	$5° \leq \Theta(\pi^+, \pi^-) \leq 175°$	56	5.6×10^{-6}
$\rho \rightarrow \pi^+\pi^-$	$30° \leq \Theta(\pi^+, \pi^-) \leq 150°$	16	1.6×10^{-6}
$ep \rightarrow ep + \rho$	$5° \leq \Theta(e^+, e^-) \leq 175°$	2.6×10^{-3}	2.6×10^{-10}
$\rho \rightarrow e^+e^-$	$30° \leq \Theta(e^+, e^-) \leq 150°$	0.73×10^{-3}	0.73×10^{-10}
$ep \rightarrow ep + J/\psi$	$5° \leq \Theta(e^+, e^-) \leq 175°$	1.0×10^{-2}	1.0×10^{-9}
$J/\psi \rightarrow e^+e^-$	$30° \leq \Theta(e^+, e^-) \leq 150°$	0.3×10^{-2}	0.3×10^{-9}
$ep \rightarrow ep + c\bar{c}$	$45° \leq \Theta_{jet} \leq 135°$	2×10^{-2}	2×10^{-9}
$c \rightarrow jet$	$p_\perp(jet) \geq 4$		
$\bar{c} \rightarrow jet$			

Table 4.5: Physics event rates ($\mathcal{L} = 2 \times 10^{31}\ cm^{-2}\ sec^{-1}$)

Source	Calculated Rate	Simulations	
		$\Sigma E_\perp \geq 10\,GeV$	$\Sigma E_\perp \geq 1\,GeV$ $+ MWPC\ z - vertex$
lost protons	$3 \times 10^5 s^{-1} m^{-1}$		
lost electrons	$1 \times 10^3 s^{-1} m^{-1}$		
p – air ($10^{-9} Torr$)	$9 \times 10^3 s^{-1} m^{-1}$	$90 s^{-1}$	$2 \times 10^3 s^{-1}$
synchrotron radiation	$1 \times 10^8 s^{-1}$		
photons $\pm 2.5m$			
cosmic rays	$3 \times 10^3 s^{-1}$		$0.1 s^{-1}$

Table 4.6: Background rates assuming $10^{-9} Torr$.

Thus the challenge of the H1 trigger system must be to accept all interesting physics and calibration events utilising the loosest possible threshold cuts while preventing background from completely swamping the data acquisition system. The maximum rate at which events can be recorded is $5Hz$. It must also be able to make decisions about the usefulness of beam-crossings occurring every 96 *nsec*.

The solution adopted has 2 important features;

1. The trigger has 4 levels corresponding to different decision times and levels of sophistication of information available to the trigger logic. The aim being to reject background at the earliest possible time and so minimise dead time.
2. The information coming from individual subdetectors is closely correlated in structure for ease of logical combination.

Calorimeter Triggers

Calorimeter signals can provide (for larger energy depositions) unique beam crossing determination for the trigger since the shaped pulses pass through zero at a precisely determined time after the beam crossing, therefore the trigger can distinguish signals not coming from beam-beam t_0's.

As previously explained, the calorimeter is read out in a tower format. This is utilised to provide trigger signals at several levels of solid angle granularity by grouping them into trigger towers and big towers. The geometrical energy deposition information can be compared with energy thresholds at first level or combined with other detector trigger information for more sophisticated triggering operations.

MWPC Triggers

These provide z-vertex and forward ray track triggers.

The forward ray trigger is available at first level because of the projective ray structure of the MWPC pad readout. The segmentation of the rays match the trigger towers of the calorimeter. In particular big-rays are formed to match very closely the acceptance of the big-towers of the calorimeter.

The z-vertex trigger is a significant peak in an event by event histogram of z intercept at the beam axis of all possible hit combinations in the CIP and COP or CIP and first forward MWPC. The associated logic is hardwired therefore available at first level.

The backward MWPC's do not yet have any trigger function.

Drift Chamber Triggers

The central jet chamber provides a $r-\phi$ trigger using CJC1 and the first 8 wires in depth of CJC2. Shift registers convert drift times into space points and this information is used to construct all possible combinations of 'roads' emanating from the beam-pipe. The distance of closest approach (DCA) of each road to the beam axis is then reconstructed. This is particularly effective in rejecting beam-wall backgrounds.

The central z-chambers are used to form a more precise z-vertex trigger than the MWPC's. All hit combinations in the CIZ and COZ are reconstructed to form a z-vertex histogram and the significance of the peak, depending on the total number of tracks in the event *etc*, determined.

Muon Triggers

The aim is to retain all events which contain candidate muons. Trigger readout is eventually to be via pads in the instrumented iron read out as rays to match the trigger tower and ray structure of the calorimeter and MWPC's. Therefore a muon trigger need only comprise coincidences between these and calorimeter trigger towers and inner track rays. Initially however, muon chamber signals will be clocked at $20MHz$ yielding $2mm$ strip readout for the trigger.

Scintillator Triggers

The TOF veto is crucial in rejecting backgrounds due to interactions of the proton beam upstream of the detector. The BEMC's are not generally capable of determining in which direction a particle passed through them and therefore the double layer of scintillator is used to distinguish particles arriving from the interaction point from those produced in an interaction with material downstream of the detector. Since, for a given bunch, particles produced at the interaction point travel approximately 4 m further than any produced downstream of the BEMC's there is a time of flight difference for arrival at the scintillator, the background particles arrive earlier than the time expected from the information given by the HERA rf system.

The trigger is used to veto whole events.

The Level 1 Trigger

This is dead time-less: that is the data is not read out by the DAQ until *after* a level 1 trigger occurs.

This is achieved since the trigger is based on hard wired logic working on data pipelined into shift registers at least 25 beam crossings deep, i.e. L1 trigger decision is expected a little after 2 μsec after the relevant t_0. When a trigger decision is made all front end data is frozen and dead time starts. The trigger data is in the form of up to 64 sub triggers which are 'OR'ed to form an L1 trigger.

The Level 2 Trigger

This is still a hardware trigger but, because it consists of more sophisticated logic and electronics, L2 has an associated dead-time of ≈ 21 μs. The main function of L2 is to sharpen cuts made at L1. Event rejection at L2 initiates overwriting of the shift registers. When this is complete the detector is again ready for an L1 trigger and dead time ends. An L2 keep signal initiates the read-in of sub-detector information to local event memory buffers and extends dead time.

The Level 3 Trigger

This is a software trigger with online processors operating on the restricted data generated by the L1 and L2 triggers. The general aim of L3 is to sharpen cuts made by these earlier triggers using more sophisticated trigger operations on the data and combining of subdetector information. The aim of L3 is to reject most events well before the 800 μs required to complete the read-in initiated by L2 is completed. In some cases L3 may be activated after a L1 keep. A rejection of the event at L3 will release the L1 freeze on data taking and end dead time.

The Level 4 Trigger

This is an online filter farm which works in isolation from the rest of the trigger and is thus, in the strictest terms part of the data acquisition. A Level 4 keep signal is responsible for dumping the entire event onto tape for later physics analysis. The processors have access to the entire event data and carry out pattern recognition operations. For example, beam-wall and beam-gas backgrounds are expected to be filtered effectively at this

stage by looking for illegal vertices *etc.* Events need not be accepted by L4 in the order in which they occurred in time due to the varying amounts of data generated by events which result in different processing times, but this is not problematic since a unique event number is associated with each event.

4.3.7 Data Acquisition and Slow Controls

Somehow the detector must be able to take raw digitisations from detectors coming from L2 triggers expected at a 100 Hz rate, decide whether or not the event is of any physics interest and dump the large amount of data onto a computer for subsequent physics analysis. If this data is to be useful, the performance of the individual subdetectors and operating conditions must also be continually monitored in order that any malfunctions and problems are spotted and corrected as soon as possible.

This is the role of the data acquisition (DAQ) system (Figure 4.9).

The processor bus system is VME. The data flow possesses a tree structure with each subdetector and the trigger having its own branch, necessary for reasons of speed and independent monitoring of subdetectors. Each of these independent branches has a dedicated MACII monitoring computer. These perform stand alone control and DAQ in the branch for set-up, calibration and debugging. They also monitor and control the subdetector support systems such as high voltage, gas and cryogenics.

The data has to undergo processing for data compression, formatting, filtering, *etc.* and therefore data buffers, computer memories on the data bus, are necessary to minimise the dead time associated with these tasks.

The subdetector information is brought together for event building. The memories which hold the subdetector data from one event are connected to each other and to a central processor (MIPS R3000 risc based VMEbus array) which comprises the online filter farm of the L4 trigger and carries out any monitoring requiring data from more than one subdetector.

If the event survives an L4 trigger the data is passed to the data logger buffer where it is prepared for transfer to the DESY IBM over optical fibres. The maximum rate at which data can be transferred is $\approx 1.6 MBytes\ s^{-1}$ or 5 events s^{-1}.

All the monitoring computers and a central multi-user computer are connected via an Ethernet Local Area Network (LAN). While the detector is data taking the software

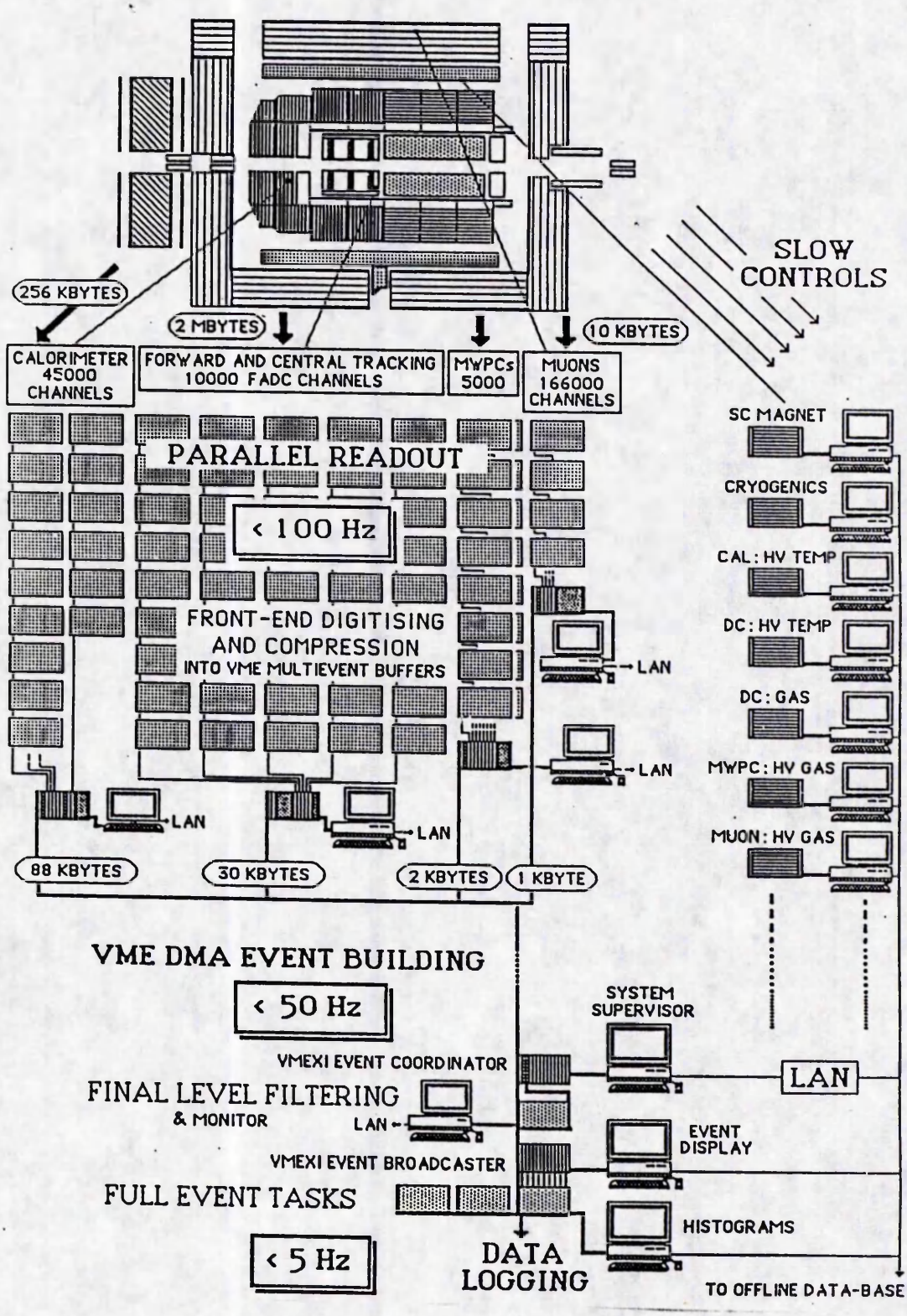

Figure 4.9: H1 Online Data Acquisition and Controls System.

running on these machines will provide clear up-to-date information to the shift crew in the form of histograms of gas pressures, H.V, resolutions *etc.* Therefore problems can be immediately spotted. The operator is able to debug and control the detector and trigger online via the central or subdetector computers and LAN.

Chapter 5

The Simulation Software

Before confident quantitative results can be obtained from the real data to be taken by H1 extensive simulation studies of the data are necessary. This is especially important in areas such as exotic searches where one must demonstrate that what may well be small deviations from standard model distributions are not merely due to backgrounds or detector effects.

In this chapter the need for simulation studies is first discussed and the technique of Monte Carlo techniques introduced.

The generator Monte Carlo programs used for excited electron signal and background studies and the H1 detector simulation Monte Carlos H1PSI and H1SIM are described.

Finally, a brief overview of the H1 software suite is given and data management conventions within the collaboration briefly introduced.

5.1 The Need for Simulation

The aim of any high energy experiment is to be able, with maximum efficiency, to take the measured 4-vectors and particle identification from the detector for any event and extrapolate from these back to the kinematics and nature of the fundamental interaction which occurred between the beam particles.

However, after the initial interaction, say the production of an excited electron or the fragmentation of the proton into struck quark and spectator di-quark in deep inelastic scattering, there are two important stages to consider when one tries to understand the data the event eventually produces in the detector.

- The particles produced by the fundamental interaction are unlikely to be the same as the particles which emerge into the detector volume. An excited electron will decay essentially at the interaction point reflecting the strength of the new preon confining interaction, the quark and di-quark will fragment into *jets* of particles in deep inelastic scattering.

  Thus it is the decay products, perhaps even third or fourth generation, which enter the detector. Indeed further decays ahead of or in the detector may also occur.

  Theoretical models provide predictions of cross sections for particular initial interactions and subsequent decays to the stable final states. The accepted method of testing theories is to compare these predictions with experimental results. In order to do this the model must somehow be incorporated into a simulation which generates event samples according to its predictions. The characteristics of the expected events can then be studied so that distributions and strategies for isolating signal from backgrounds can be formulated using event characteristics. In this work the excited electron $e\gamma$ decay signature and that of relevant background processes are simulated.

  Simulations are also important for calibration of HERA's operating luminosity. Pure QED processes for example are known to be described very accurately by the theory. Simulated distributions can therefore be directly compared to real data to give integrated luminosity ($\mathcal{L}$) measurements.

  Thus one requires EVENT GENERATOR software.

- Even given a model which completely predicts all cross sections and final state distributions correctly, one still has to take into account the effect of errors introduced into the measurement of the particle 4-vectors by the detector itself.

  The size and complexity of the H1 detector means that a relativistic particle emerging from the beam-pipe is confronted by a large amount of material with which it can interact. Such interactions include pair production from energetic photons, catastrophic nuclear interactions involving hadrons and ionisation losses, and all involve energy loss or momentum change which act to distort the initial 4-vectors of the event.

  Thus the physical presence of the measurement devices necessarily introduces a level

of distortion to the data.

In the previous chapter the various H1 subdetectors were described and note made of the resolutions of each, that is the accuracy to which a specific detector can make the measurement it is there to make. For example, an energy measurement taken by the calorimeter will be of limited accuracy due to uncertainties in

- containment of the shower
- conversion of shower energy to detectable energy
- effiency of read-out
- shower development

and these are all reflected by the subdetector resolution figures.

The finite resolutions of the subdetectors results in a *smearing* of the original 4-vectors.

Thus detector response simulations are required which, as a minimum, take an initial set of 4-vectors and, using subdetector resolutions and secondary interaction probabilities and distributions, yield a set of *smeared* 4-vectors taking into account scattering, effect of the magnetic field on charged particles, gas ionisation for charged tracks, shower development in calorimetry, finite coverage of the detector, cracks in calorimeters and subsequent decays of unstable particles.

This is the function of DETECTOR RESPONSE software.

Apart from providing the foundation on which the physics analysis will be based, simulation studies also fulfill other important functions. At HERA a crucial problem will be how effectively the trigger can distinguish potentially interesting physics events from high rate backgrounds such as beam-wall, beam-gas interactions. Simulations are crucial to this work. Background generator packages simulate interactions of the beams with accelerator components, residual gas, beam-pipe *etc* and these events are passed through detector simulations. The information is used to isolate characteristics of events to be used as online triggers or vetoes.

Data simulation has also been essential in the development of the reconstruction software, a package that will eventually take the raw event data and reconstruct the information as 4-vectors with errors and particle identification. The pattern recognition algorithms for example have been extensively debugged using simulated tracker raw data.

5.2 Monte Carlo Methods

The effects modelled by the simulation software have known distributions derived from the physics of the interactions. Unstable particles have known mean lifetimes, kinematics and cross sections can be calculated from the relevant theory, subdetector resolutions have been experimentally determined and so on. Thus, although one cannot reproduce real data on an event-by-event level one can generate event samples with the same overall distributions (given the model is a good one).

The method by which random numbers are generated according to particular distributions and weightings is known as the **Monte Carlo Method** and is the basis of all the simulation programs (Monte Carlos) used in this work.

5.3 The Generator Programs

The expected backgrounds to an excited electron have been previously introduced (see section 3.4.2). In order that strategies for best isolating the signal from these backgrounds can be developed a suite of Monte Carlo generator programs which simulate each event class is required. In this section these generator programs are described.

5.3.1 JETSET

Although, in theory, all hadronisation processes can be evaluated using QCD, in reality the equations become so complicated at low momentum transfers that they become effectively insoluable (Section 2.1.4).

The soft fragmentation of quarks into hadron jets falls into this regime and so once one has calculated the hard parton level interaction using perturbative methods one is left with the problem of how to treat the resulting hadronisation of the partons. This is carried out by the JETSET [31] Monte Carlo using the Lund phenomenological string model for hadronisation of a multiparton configuration [32].

Using the string model of jet fragmentation (Figure 5.1) the Monte Carlo takes an initial parton configuration and simulates the soft hadronisation into jets of hadrons, with unstable hadrons decaying further.

Because of gluon self interaction, the color force between 2 partons moving away from one another is envisaged as a color flux tube being stretched between them. The energy

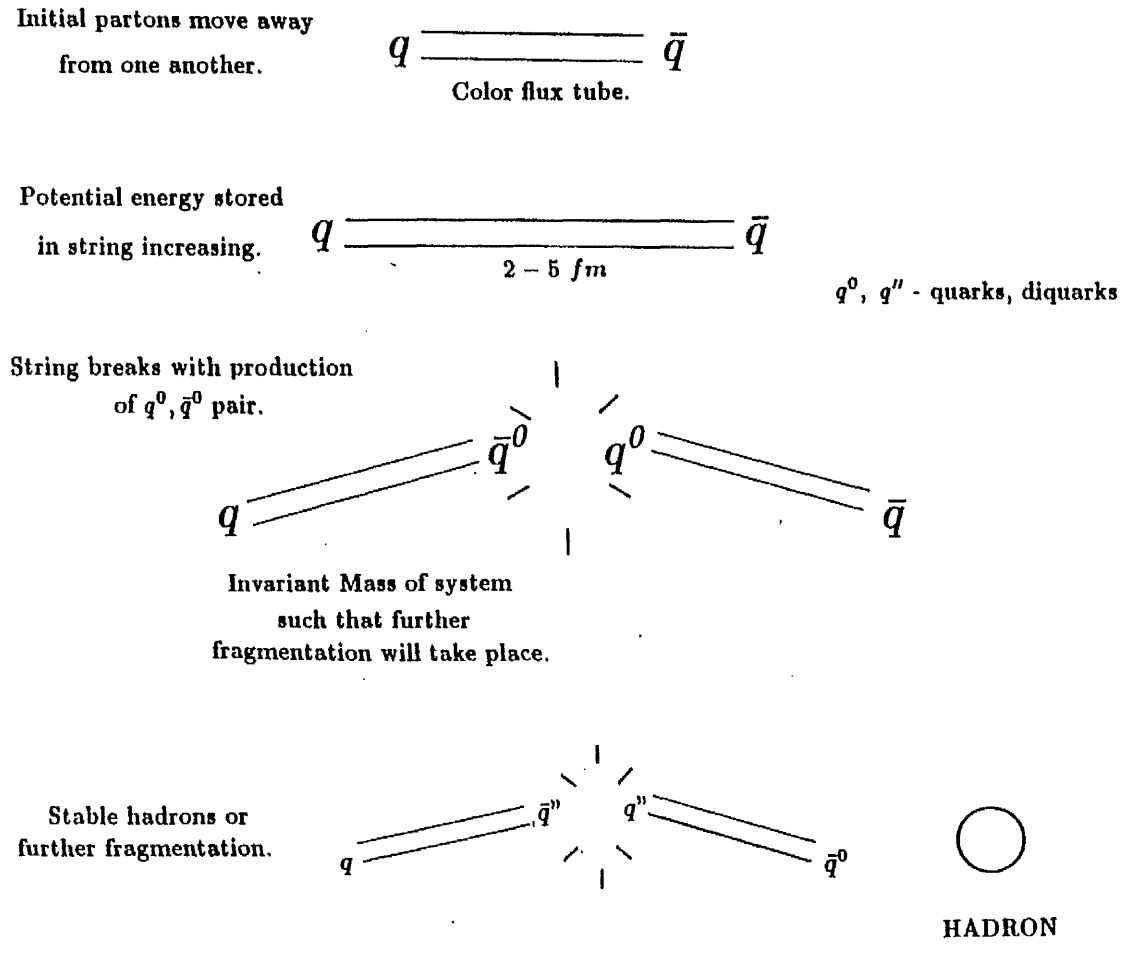

Figure 5.1: Schematic showing the basic process of string fragmentation of partons into hadrons.

density along the string can be estimated;

$$\kappa = \frac{\textbf{Mass of typical Hadron}}{\textbf{Size of typical Hadron}} \approx \frac{1\ GeV}{1\ fm} \approx 1\ Gev\ fm^{-1} \approx 0.2\ Gev^2 \qquad (5.1)$$

Thus, as the partons move apart the potential energy stored in the string increases until, when it is $\approx 2-5\ fm$ long, the string 'breaks' to produce a quark-antiquark (diquark-antidiquark) pair and there are now two parton systems. If any of these have enough invariant mass the string fragmentation continues.

Within this framework the various aspects of jet evolution are modelled and tweaked

to agree, where possible, with known jet phenomenology. These include;

- Suppression of heavy flavours in the quark production mechanism.
- Relative probabilities that a quark-antiquark or diquark-antidiquark pair is produced on the breaking of a string.
- Type of meson (pseudoscalar or vector) or baryon (spin $\frac{1}{2}$ or $\frac{3}{2}$) produced for a given set of quarks.
- Distribution of 4-momentum amongst the jet components.

Specific to HERA, JETSET also models the fragmentation of a baryon target struck quark-spectator quark initial configuration and estimates the weightings for events where the two quark object ends up in the same hadron compared to events where they do not.

Some of the hadrons produced will not be stable with respect to decays and these are implemented according to standard model techniques and phenomenology [12].

5.3.2 LEPTO

This is the Lund Monte Carlo program for deep inelastic lepton-nucleon scattering of the types shown in Figure 5.2.

The hard parton level interaction is generated using standard electroweak theory with some QCD corrections and the resulting parton configuration fragmented using JETSET 6.3. A full listing of the physics switches and cuts available can be found in the long write-up [33], those of particular interest here are summarised in Table (5.1).

A schematic representation of the program structure is shown in Figure 5.3. Once the user has specified any cuts and options the program initializes by calculating cross sections in the kinematic region allowed by the cuts based on the quark-parton model with electroweak matrix elements for the hard scattering, folded with QCD evolved quark structure functions. The integrated cross section over this region can then be calculated to user supplied accuracy. The probability that a specific event might contain higher order QCD processes such as gluon radiation or boson-gluon fusion (Figure 5.2b,c) is also calculated and stored.

Events are subsequently generated weighted by these factors. For each the differential cross section is sampled and a Monte Carlo cross section estimation updated. The accuracy

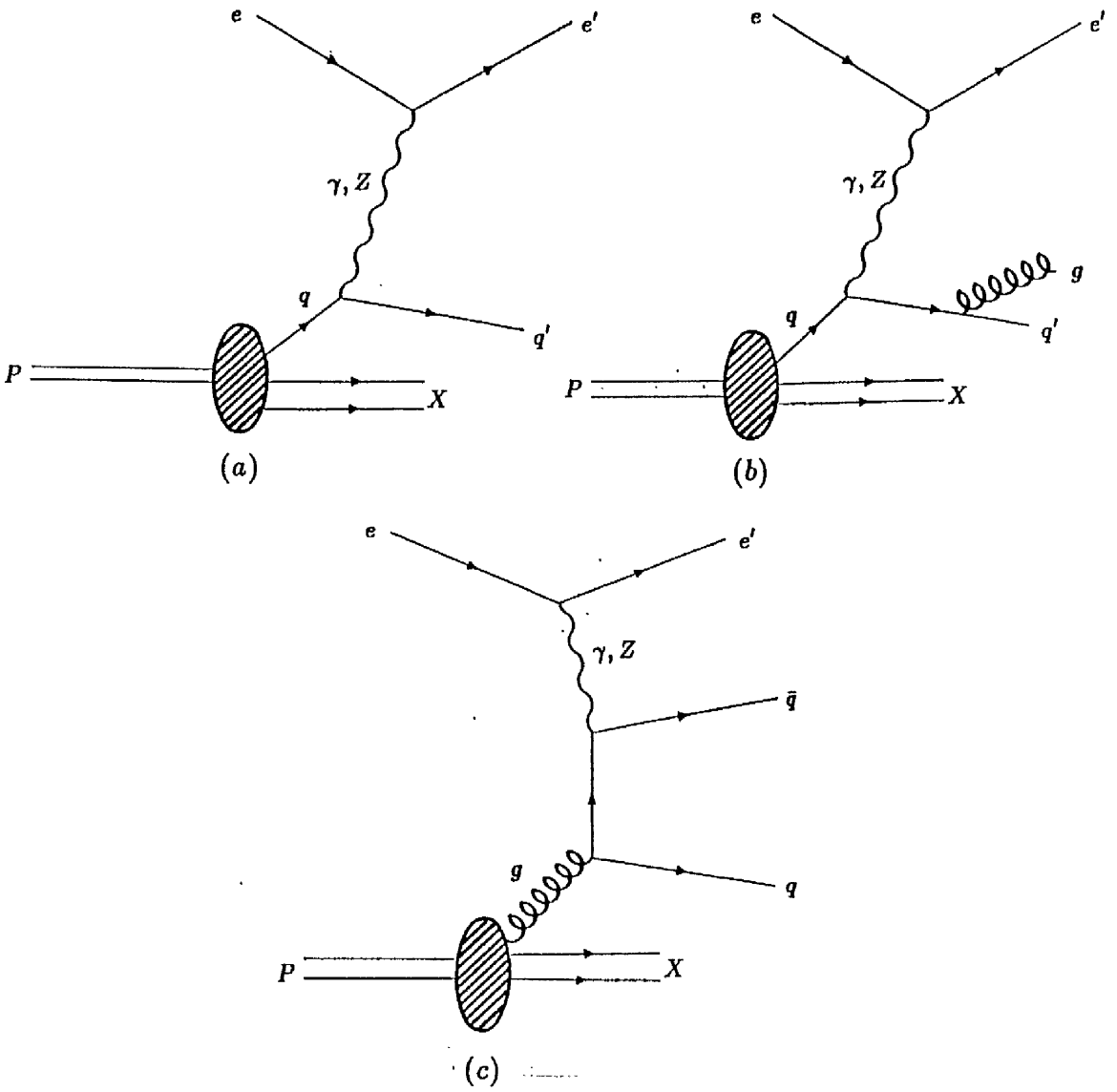

Figure 5.2: Deep Inelastic lepton-nucleon scattering processes generated by LEPTO

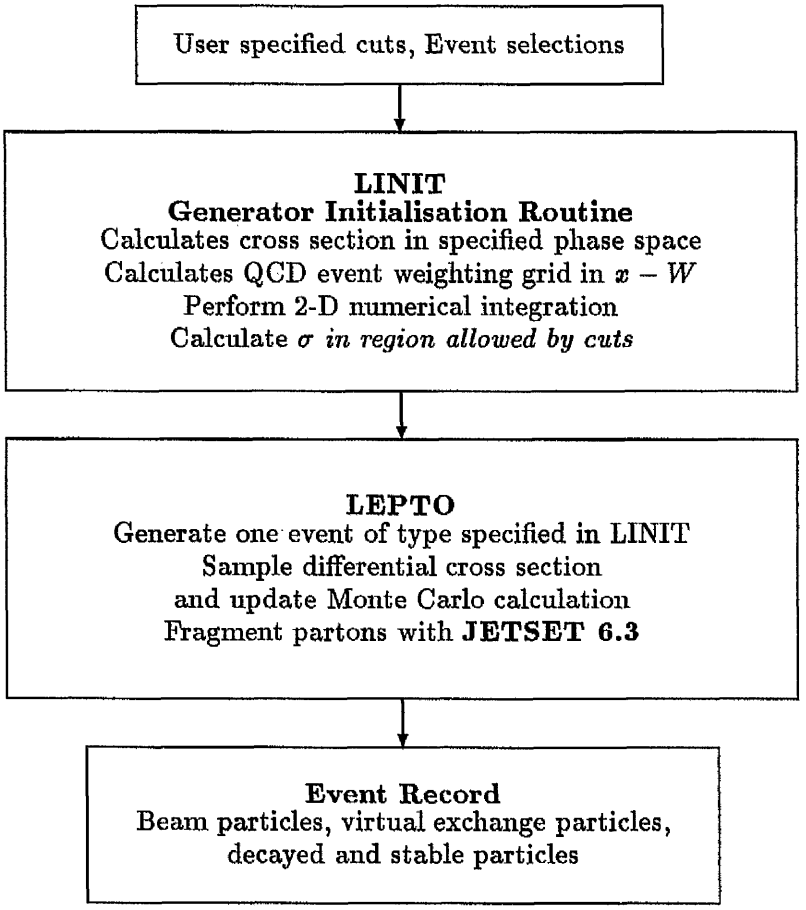

Figure 5.3: Schematic diagram showing structure of LEPTO.

Option	
Beam lepton	Particle, 4-momentum
Beam nucleon	Particle, 4-momentum
Type of Interaction	EM - Pure photon exchange Weak NC - Pure Z^0 exchange Weak CC - $W^{\pm}$ exchange NC - γ, Z^0 with interference
Bjorken x	$0.001 \leq x \leq 1.0$
Bjorken y	$0.00 \leq y \leq 1.0$
Momentum Transfer Q^2	$4.0 \leq Q^2 \leq 1.0 \times 10^8$
Scattered lepton energy	$1.0 \leq E_{l'} \leq 1.0 \times 10^8$
Scattered lepton θ	$0.0 \leq \theta \leq 3.1416$

Table 5.1: Table showing some kinematic and physics user options available in LEPTO.

of this is given by;

$$\frac{\Delta N}{N} = \frac{1}{\sqrt{N}} \tag{5.2}$$

Each generated event is recorded in its entirety. Every particle or jet which took part in the interaction (beam, virtual, quark jet, decayed etc) occupies one line in the event record storing particle type using the PDG particle codes [12], 4-momentum, mass, status and history [31].

5.3.3 COMPOS

This is a Monte Carlo generator for compositeness physics in electron-proton scattering [26, 34]. Leptoquark, leptogluon, excited lepton and quark production are simulated, the excited electron possibilities are summarised in Figure 5.4.

The generator is based heavily on the model used by Hagiwara et al. [18] described in section 3.2. The basic kinematic variables x and Q^2 of generated events are chosen according to the cross sections given in equations 3.8, 3.13 and 3.10 folded, where necessary, with QCD evolved quark structure functions. Only γ exchange is included, excited electrons with spin $\frac{1}{2}$ and magnetic transitions to ordinary electrons are assumed. The excited electron is initially produced on mass shell, then smeared according to a Breit-Wigner

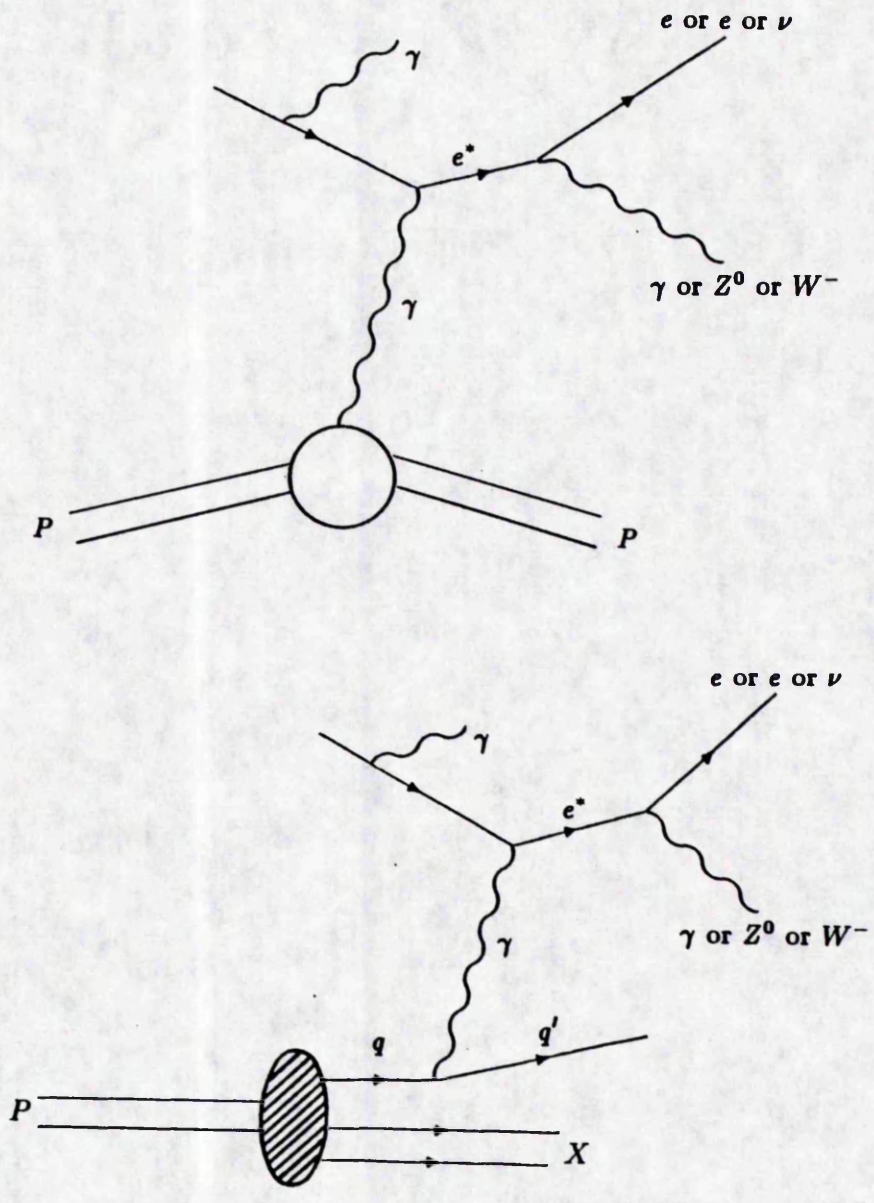

Figure 5.4: Excited Electron events available in COMPOS 1.1.

function to simulate a natural width.

The available run cuts of interest here are shown in Table 5.2.

OPTION	
Beam Lepton	Particle type, momentum
Beam Hadron	Particle type, momentum
Type of exotic particle	LG, LQ, e^*, ν^*, q^*
Mass of exotic particle	GeV
Interaction Scale Λ	GeV
Lepton Bremsstrahlung	On/Off
Decay channel	$e^* \rightarrow e + \gamma$ $e^* \rightarrow e + Z^0$ $e^* \rightarrow \overline{\nu} + W^-$
Production Mechanism	Elastic, inelastic, both
Proton Structure Function Parameterisation	

Table 5.2: Table showing some kinematic and physics user options available in COMPOS.

The structure of the program is very similar to that of LEPTO. The integration of the cross section is performed using a different method and fragmentation is with JETSET 7.3. A cross section value is avaliable only from initialisation.

5.3.4 EPCOMPT

This program generates electron-proton wide angled bremsstrahlung events [35] in electron proton collisions at HERA energies.

The cross sections are derived using the calculations of Courau *et al* [28]. The cross sections are calculated from a convolution of the Compton cross section for the process $e\gamma^* \rightarrow e\gamma$ (γ^*- virtual photon from proton vertex) and the photon spectrum radiated by the proton (Figure 5.5). The latter is dependent on the proton form factors (elastic) and structure functions (inelastic) and thus a slight model dependency is introduced in the inelastic case.

To simplify these calculations one makes the approximation that the Q^2 of the virtual photon is small compared with W^2, the invariant mass squared of the final state $e\gamma$. Since

the important invariant mass range in this study is $> 40\ GeV$ and cross sections are dominated by low Q^2 processes this approximation is valid.

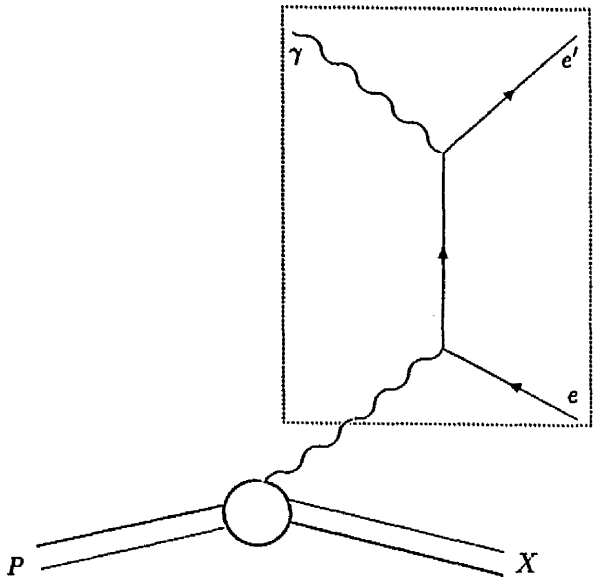

Compton Cross Section $\dfrac{d\sigma}{d\Omega^*}$

Equivalent Photon Approximation (EPA) $\dfrac{dN}{dy\ dQ^2}$

$$\frac{d\sigma^{ep\to e\gamma(X)}}{dy\ dQ^2\ d\Omega^*} = \frac{dN}{dy\ dQ^2}\frac{d\sigma^{\gamma^* e\to e\gamma}}{d\Omega^*} \qquad \left(y = \frac{W^2+Q^2}{s}\right)$$

Figure 5.5: The Wide Angle Bremsstrahlung process factorised into equivalent photon spectrum and Compton scattering components.

5.4 The Detector Response Programs

5.4.1 H1SIM

This is the H1 detailed response Monte Carlo [38]. Its aim is to take a set of generator event 4-vectors and simulate, as well as possible, the physical effect the passage through the detector has on every particle and the subsequent raw data H1 yields for that event. This is done within the framework of the CERN program GEANT 3.14 [37].

There are 3 major stages in the processing of each event.

OPTION	
Beam Particles	Type, momentum
M^2_{min} (virtual electron)	
M^2_{max} (virtual electron)	$(s - m_p)^2$
$\theta(proton)$	$0.0 \leq \theta \leq 3.1416$
$\theta(photon)$	$0.0 \leq \theta \leq 3.1416$
$\theta(electron)$	$0.0 \leq \theta \leq 3.1416$
Energy(electron)	
Energy(photon)	

Table 5.3: Table showing some kinematic and physics user options available in EPCOMPT.

- The Physics Simulation

  Every particle is 'stepped' through small volumes of the detector. For each step physical affects such as bending in the magnetic field, interactions with the material and secondary particle generation are modelled.

  In order that this can be done the program must have access to information regarding the detailed geometry of the detector, the material from which all components are constructed, a mapping of the magnetic field *etc.* All such non-event data is stored in the H1 Database file.

  The end product of this stage are 'HIT BANKS' which store xyz coordinates of exit/entry points energy depositions in each volume, for every particle, primary or secondary.

- The Detector Digitisations

  Given the physics, the next stage is to simulate how this is converted to subdetector output data.

  For this one needs to know where the active and dead material is in the detector, i.e how much of the physics is accessible to the measuring devices, the method and format of readout and the resolutions of the subdetectors. This information is also found in the database.

  This stage outputs 'DIGI BANKS', data that, as exactly as possible, is in the same format as real data. Therefore in the form of channel numbers, wire addresses, ADC

counts *etc.*

- Trigger

  The trigger response for the event is simulated.

  Using only information available at the time of each level, trigger decisions are carried out using software simulation of trigger logic and run conditions selected by the user.

The price paid for the best possible modelling of the physics is reflected in event processing times. Table 5.4 shows average processing time for a typical DIS event on the DESY Central IBM 3090. H1SIM can be run with either full shower production algorithms (GEANT/GHEISHA) or with a degree of parameterisation of the shower development and shapes (ALGORIX and GFLASH options).

Detector Simulation	CPUtime/event	CPUtime (1 hour's data)
H1SIM 2.04 (GEANT/GHEISHA)	250 s	25 hrs
H1SIM 2.04 (ALGORIX)	88 s	8.8 hrs
H1SIM 2.04 (GFLASH)	25 s	2.5 hrs
H1PSI 0.92	0.07 s	25.2 s

Table 5.4: Event processing times (IBM 3090) for various detector response programs.

Using a reasonable rate estimate (Table 4.5) of $\approx 0.1\ Hz$ for a NC DIS event assuming a luminosity of $2 \times 10^{31} cm^{-2} s^{-1}$ it is clear that if one is going to try and study HERA physics using the full Monte Carlo even in its fastest form the processing time required to simulate equivalent data samples is completely restrictive as shown in Table 5.4.

A faster method is obviously needed.

5.4.2 H1PSI

H1 Parameterised **SI**mulation, the fast detector response Monte Carlo [39]. The name is the key to the speed of the program. Where H1SIM tries to model as precisely as possible the detector geometry, materials, physical processes, H1PSI uses *parameterisations* (simplified representations) wherever possible. Using initial conditions the program can therefore make fast predictions of the resulting track, shower characteristics *etc.*

For example, in the central tracking region, approximated by a simplified double cylinder geometry, the program takes the initial 4-vectors of charged particles and uses a

function representing the magnetic field behaviour over the tracker volume to calculate a helix extending out to the calorimeter. Once the helix is defined the number of hits in the tracker is determined. Once all particles (including any secondaries) have been treated, tracks are discarded if the momentum is below some minimum value, there are not enough hits in the tracker to be able to reconstruct or if two fall within the two track resolution one is randomly discarded. The remaining tracks then have the 'true' helix points smeared by a relevant set of parameterised resolutions to produced a set of detector smeared 'reconstructed' tracks.

The output of H1PSI is tuned with output from H1SIM. So, for example, although the physical presence of cracks in the calorimeter (volumes effectively dead as far as measurement is concerned such as cable runs) is not included explicitly in the program their presence is reflected in the width of the Gaussian smeared resolutions the fast simulation uses. If an electron has θ, ϕ such that it passes along a crack in the calorimeter the energy recorded by the calorimeter sits many standard deviations away from the mean of the distribution one would expect from just calorimeter sampling fluctuations *etc.* H1SIM would be aware of this and correct for it. Within H1PSI, which gains speed by including a pointing geometry structure to the detector and no fine detail within these volumes, the presence of a crack in a particular angular region results in a widening of the Gaussian fitted to this resolution distribution. Thus particles passing through the relevant volume return energy measurements smeared by a wider Gaussian resolution rather than considering whether or not they pass through a crack on an event by event basis.

5.5 Summary

The full suite of H1 software simulation and reconstruction programs are shown in Figure 5.6. Included here are the graphics programs EVLOOK and PSILOOK which provide a graphical representation of what events look like in the detector. Also included is H1REC, the reconstruction package whose function it is to take raw data, either from H1 or H1SIM output, and reconstruct tracks, clusters, kinematics in events.

In order that there is complete compatibility for input/output processes from one program to another the collaboration uses the BOS and FPACK data storage and management packages [40]. The analysis work presented here uses the DATMAN data management

package [41] to access information from the Monte Carlo outputs.

Numerical results presented here use H1PSI results. There are several reasons for this. Firstly, a full study of the background processes is impossible using the full Monte Carlo due to the highly restrictive CPU time required to process even a fraction of the required number of events through. At this time there is also no stable version of the reconstruction program H1REC available to the collaboration and thus no track, cluster finding facilities for dealing with H1SIM output. This does not however seriously impede the aim of the work presented here since one is looking for fairly liberal limits on e^* masses and Λ values and not the detailed quantitative analyses which will be required should candidate events actually be found in real data.

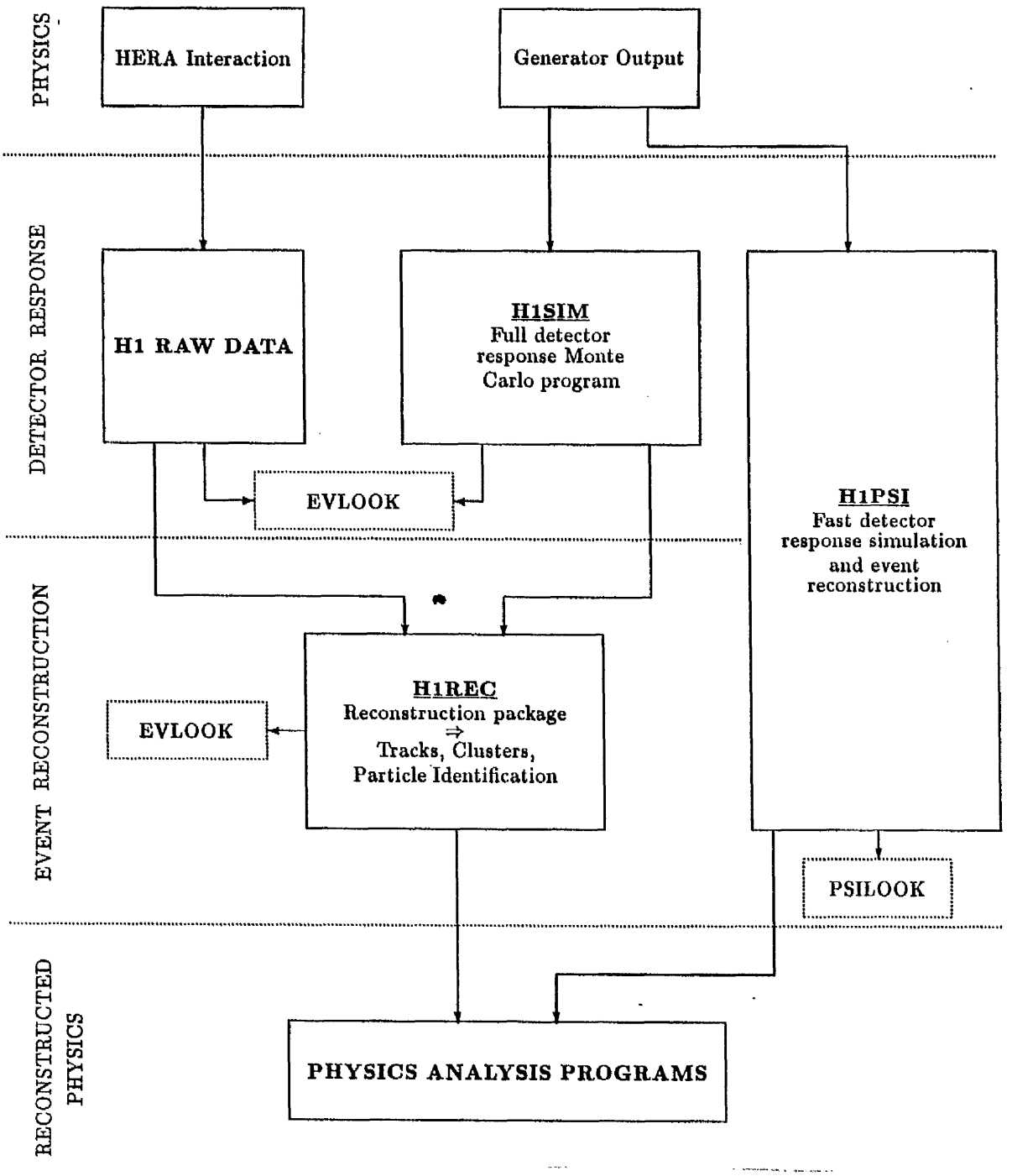

Figure 5.6: Simulation, Reconstruction and Visualisation - The H1 Software Suite

Chapter 6

Event Selection and Cuts

In this chapter a set of event selection criteria and cuts is developed. The aim is to look for an e^* signal over the full range of excited electron masses accessible at HERA rather than specific mass searches. Thus, one aims to reduce wide angle bremsstrahlung and deep inelastic physics without significantly biassing against an e^* signal in the full range 40 to 250 GeV.

At the generator level $e^* \rightarrow e\gamma$ event characteristics are studied and these are used to propose a set of basic event selection criteria. Problematic wide angle bremsstrahlung events are also studied and the differences in final state distributions of these and the e^* events discussed.

Samples of excited electron, wide angle bremsstrahlung and neutral current deep inelastic scattering events are processed by the H1PSI detector Monte Carlo. The events are then passed through a set of cuts utilising the event selection criteria determined from the generator studies.

Signal losses and fake candidate events are discussed and further event selection cuts relevant to each background process added.

6.1 Excited Electrons - Event Characteristics

6.1.1 e^* Production Kinematics

In order to study the kinematics and general features of the signal a sample of 2100 e^* masses in the range $40 - 250$ GeV were simulated using COMPOS and allowed to decay to $e\gamma$. This mass range extends from a slight overlap with the current e^* mass limits, derived

from the most model independent production processes (Table 2.5), over the full range of e^* masses expected to have a potentially discoverable production rate at HERA.

The kinematics of the e^* production is easily understood since the basic interaction is the collision of the beam electron and a virtual photon (Fig. 6.1).

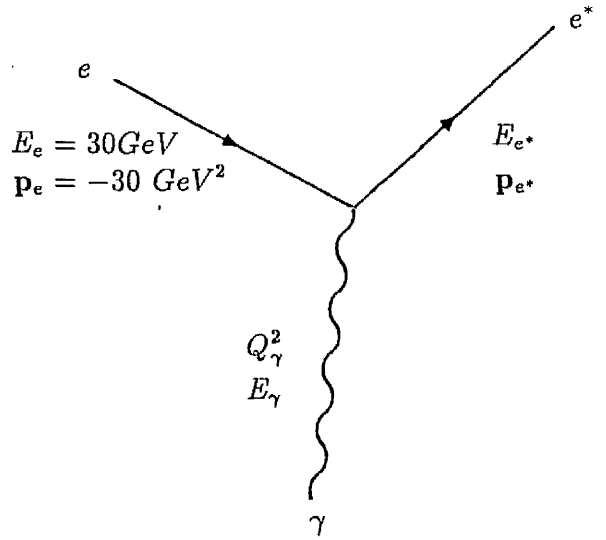

Figure 6.1: $e\gamma \rightarrow e^*$.

The photon is emitted from either the proton (elastic, quasi-elastic) or struck quark (inelastic) vertex. The energy of the virtual photon is limited by kinematics in the case of elastic production, and the x of the struck quark in inelastic production. The energy spectrum reflects the probability distribution of a particular energy photon from a vertex. The process is, as previously discussed (Section 3.4), low Q^2 dominated. This is clearly seen in Figure 6.2 which shows the Q^2 and lab energy distributions of the exchange photons.

Because of this low Q^2 dominance in the cross section the $e\gamma$ collisions can be thought of as effectively head-on and this is useful in deriving some estimates for kinematic limits on the production.

Since the virtual photon flux for a given m_{e^*} is dominated by energies close to production threshold it follows that;

- For $m_{e^*} < 60\ GeV$ the excited electron will tend to be moving along the incident electron direction.
- For $m_{e^*} = 60\ GeV$ the excited electron will be more or less produced at rest in the lab.
- $m_{e^*} > 60\ GeV$ the excited electron is moving along the proton direction.

This can be seen in Figure 6.3 which shows the variation of polar production angle θ with m_{e^*} in the lab frame. The deviations from the beamline are due to finite Q^2 values.

The minimum production energy $E_\gamma^{\min}$ follows from:

$$M^2 = (\Sigma E)^2 - (\Sigma p)^2 = m_{e^*}^2 \tag{6.1}$$

Therefore, in the lab frame

$$\begin{aligned} m_{e^*}^2 &\simeq (E_e + E_\gamma^{min})^2 - (E_\gamma^{min} - E_e)^2 \\ E_\gamma^{min} &= \frac{m_{e^*}^2}{120} = 820x \\ x_{min}(m_{e^*}) &= \frac{m_{e^*}}{98400} \end{aligned} \tag{6.2}$$

since $E_e = 30GeV$, $E_p = 820GeV$ and x is the fraction of the proton energy carried by the photon.

This kinematic constraint is illustrated in Figure 6.4 which shows the relation between production x and m_{e^*} from the generator. The events at $x = 1.0$ correspond to elastic production. The population along increasing x for a constant m_{e^*} reflects the bremsstrahlung-like spectrum of emitted virtual photon energy and corresponds to more energetic e*'s.

The corresponding minimum lab energy of the excited electron is therefore

$$\begin{aligned} E_{e^*}^{min} &= \sqrt{(m_{e^*}^2 + (\Sigma p)^2} \\ &= \sqrt{m_{e^*}^2 + \left(\frac{m_{e^*}^2}{120} - 30\right)^2} \\ &= (E_{e'} + E_{\gamma'})^{min} \end{aligned} \tag{6.3}$$

where e' and γ' are the decay products. This is shown in Figure 6.5.

Although the e^* production itself is a low Q^2 interaction, if a Q^2 is reconstructed from the decay electron as though it were a DIS scattered electron the value is high due to the p_T $\mathcal{O}(m_{e^*})$ gained from the e^* decay.

Since $Q^2 \approx (\Sigma p_T)^2$ it is possible to estimate the maximum reconstructed Q^2 from the decay electron for a particular m_{e^*}. Again assuming $Q^2(\text{virtual photon}) \approx 0$ one sees the greatest p_T when the decay products are emitted at $\theta = 90^o$ in the e^* rest frame, i.e $\Sigma p_T = m_{e^*}$. In this case

$$Q^2_{\max}(m_{e^*}) = m_{e^*}^2 \tag{6.4}$$

Figure 6.6 shows the variation of reconstructed Q^2 with excited electron mass. The population as a function of Q^2 for a given m_{e^*} is related to θ^* the decay angle relative to

the electron beam direction in the e^* rest frame. Over 95% of the decay electrons have a reconstructed $Q^2 > 100GeV^2$. Therefore excited electron events are distinguishable from the highest rate deep inelastic physics by a simple minimum Q^2 cut. This makes the DIS background signal significantly more generatable one since

$$\sigma_{[Q^2>4]} \approx 150,000\ pb$$

$$\sigma_{[Q^2>100]} \approx 5,000\ pb$$

using LEPTO 5.2.

The low Q^2 region of deep inelastic physics is also that most prone to photoproduction and beam-wall, beam-gas backgrounds since these processes too will be dominated by final state particles with low p_T. Thus excluding such events from consideration effectively excludes also the unpredictable and hard to anticipate and generate background sources.

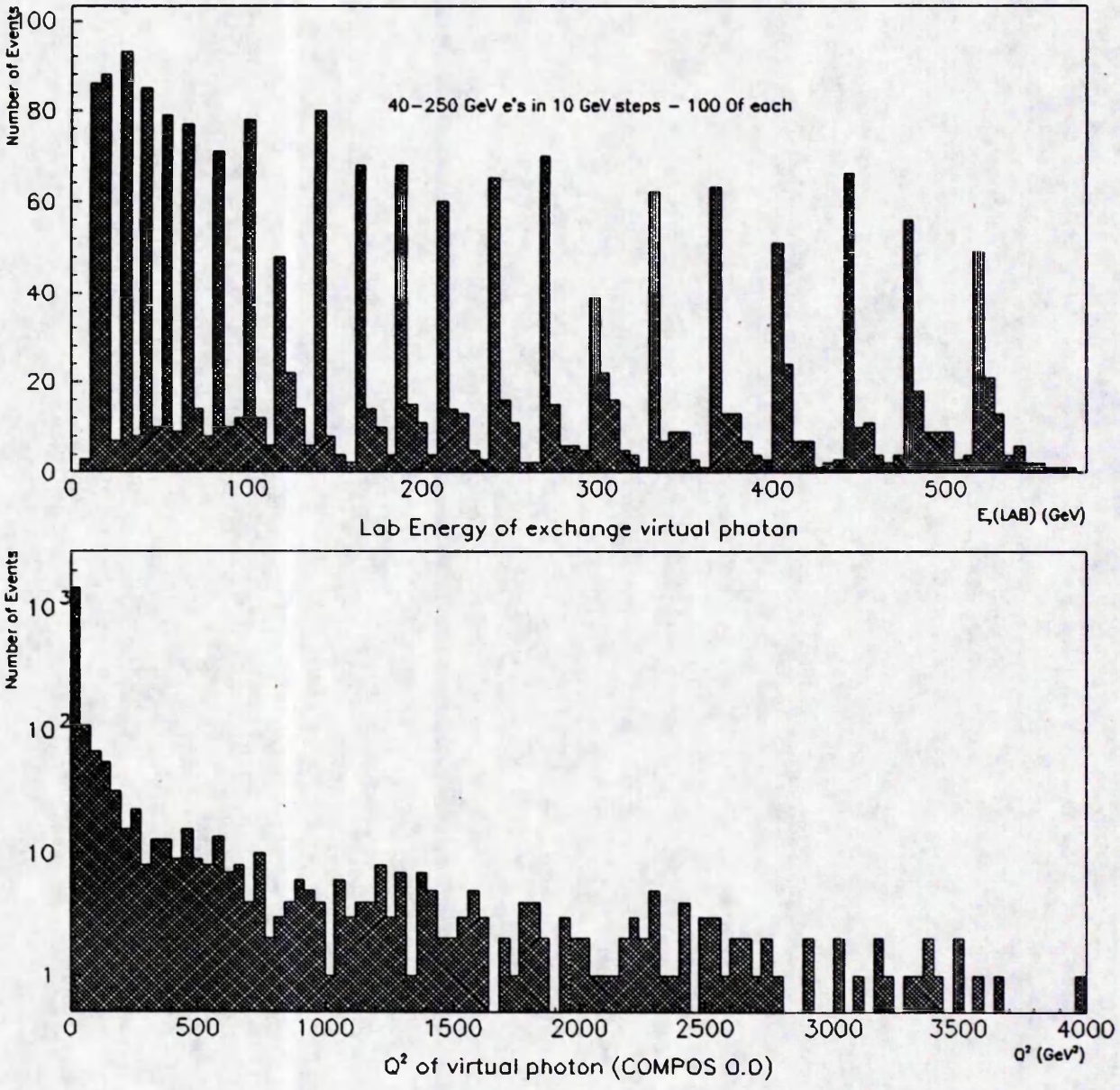

Figure 6.2: Properties of the virtual exchange photon.

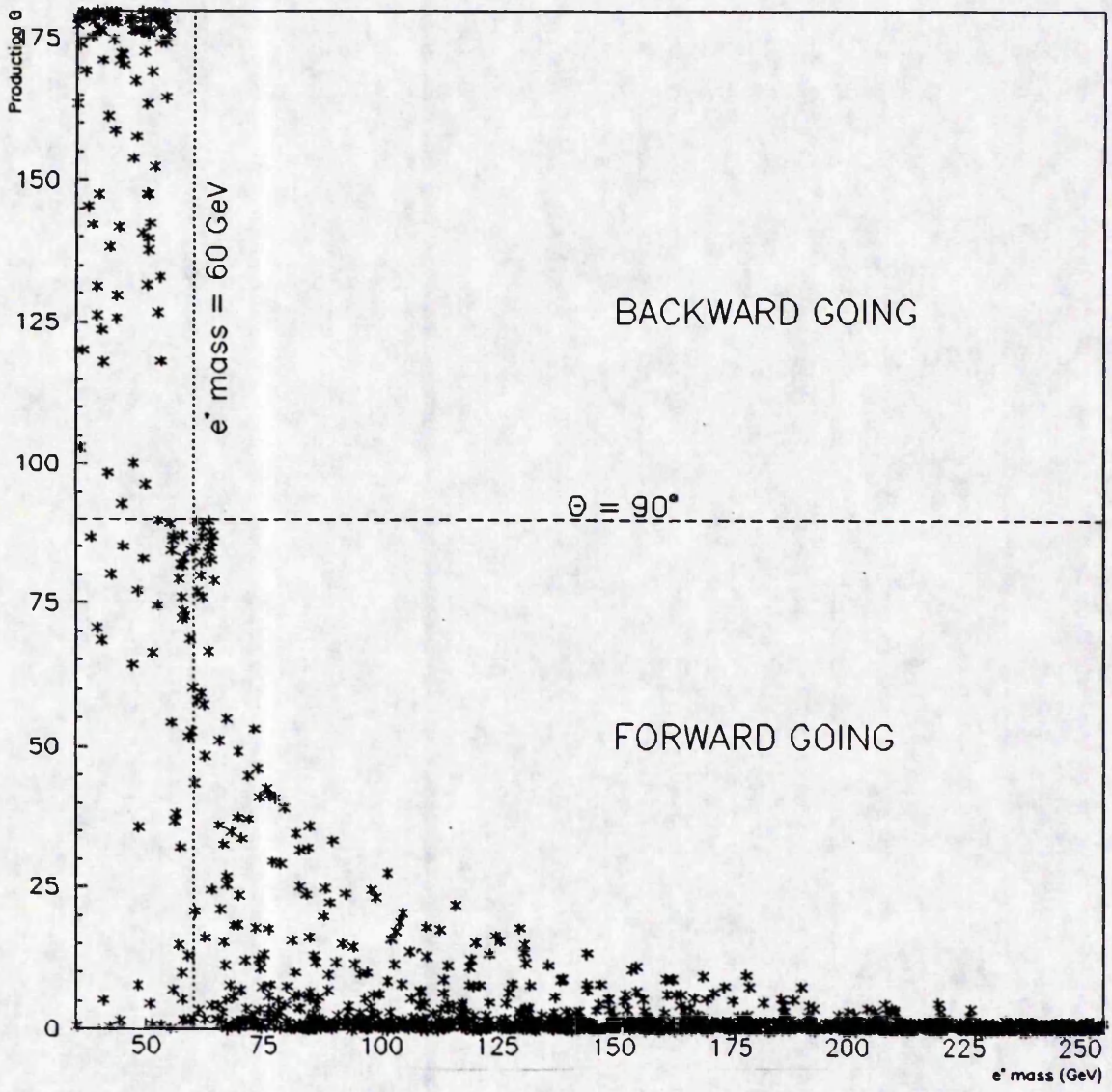

Figure 6.3: Variation of production θ_{lab} with excited electron mass.

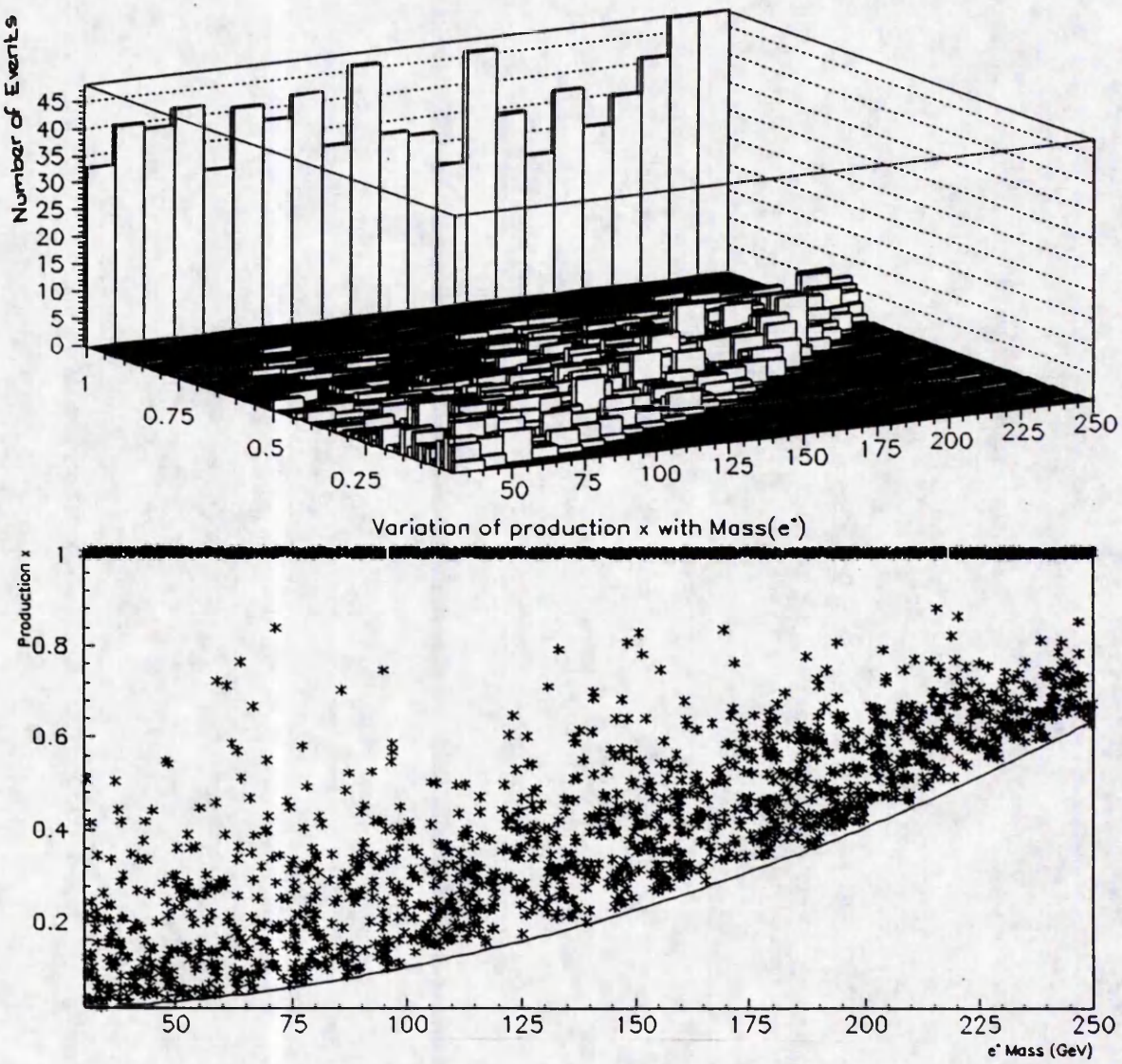

Figure 6.4: Variation of production x with excited electron mass showing kinematic limit on minimum x.

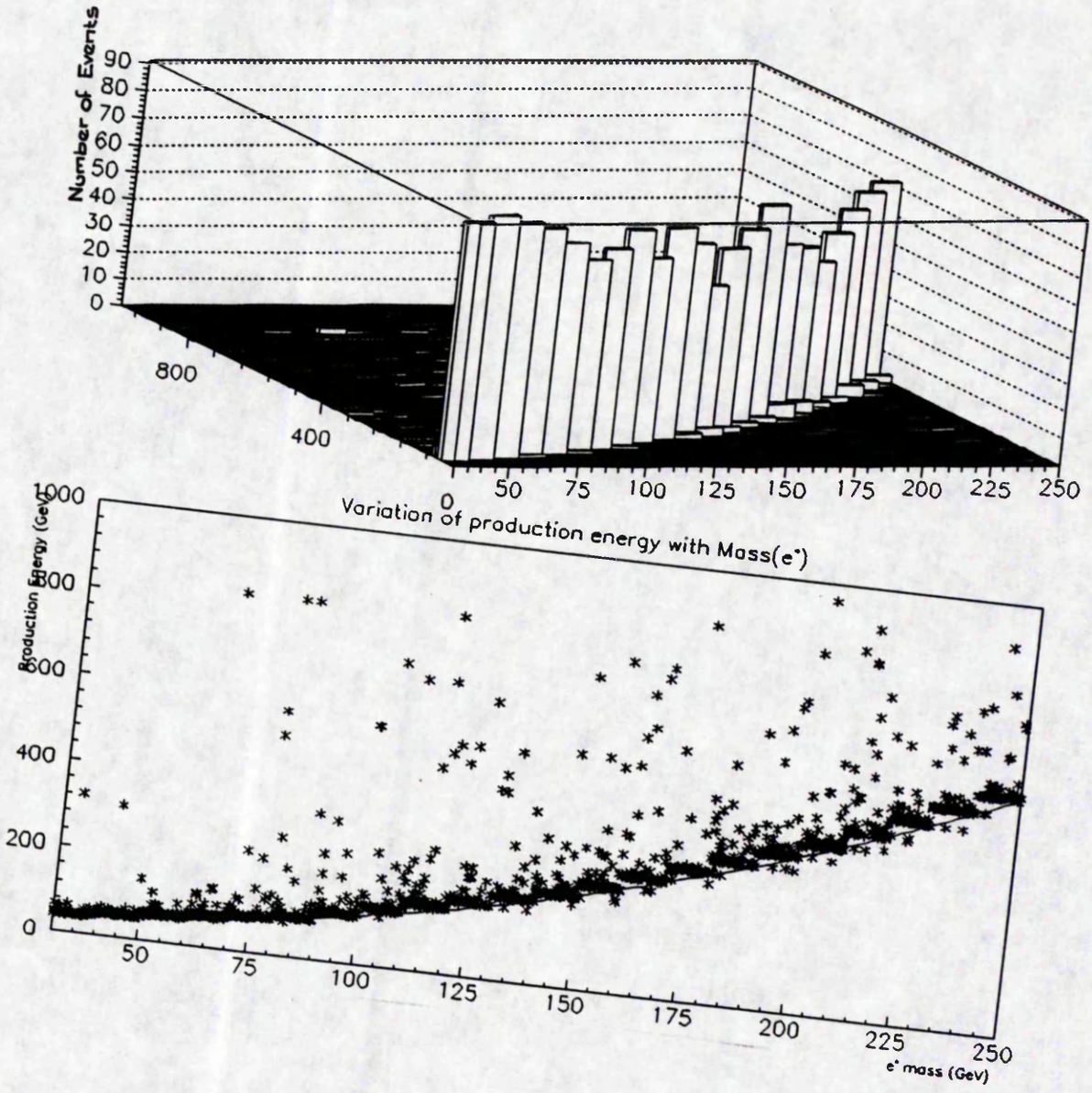

Figure 6.5: Variation of e^* lab energy with m_{e^*} showing kinematic limit on minimum energy.

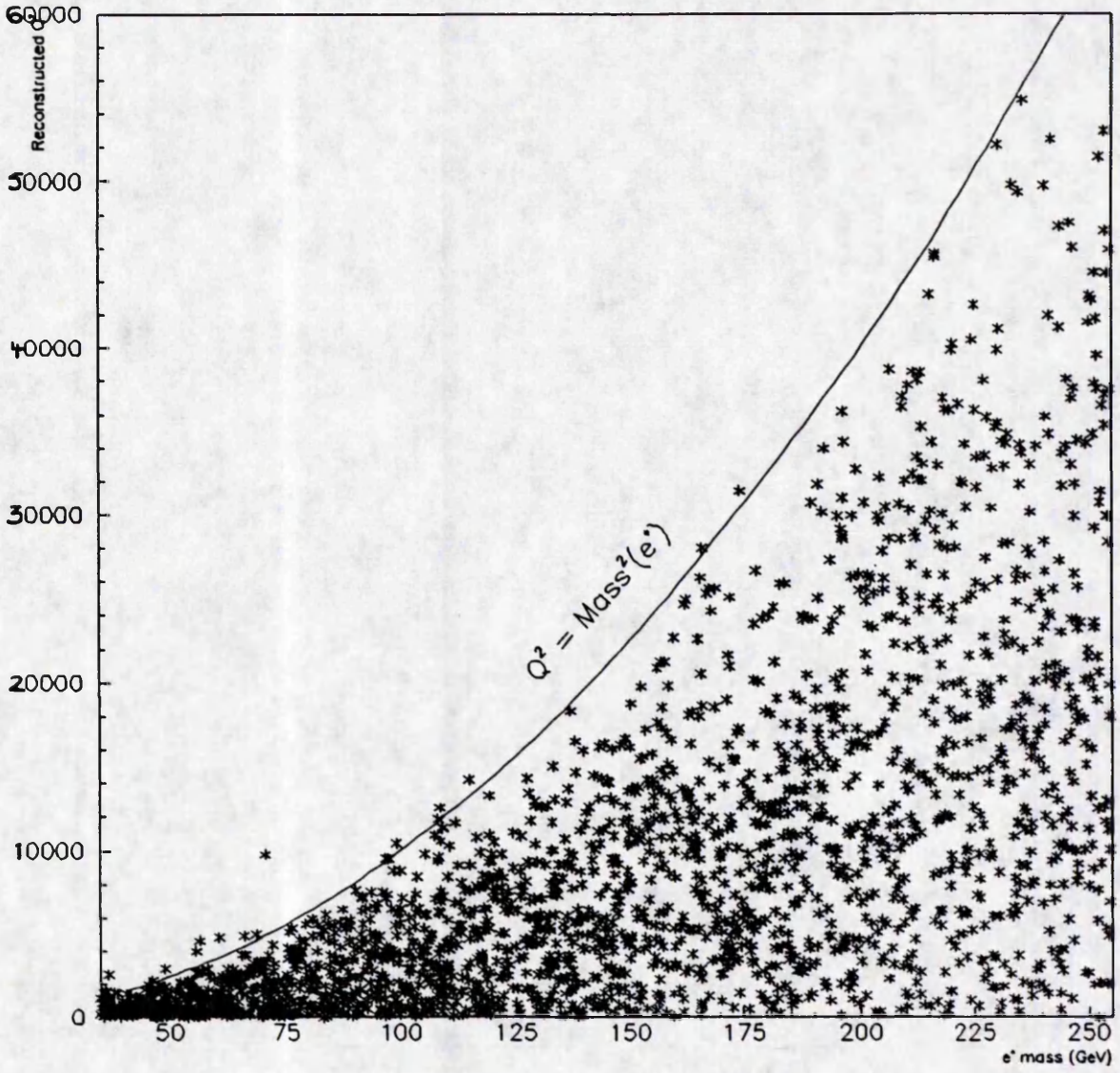

Figure 6.6: Variation of Q^2 reconstructed from decay electron with excited electron mass.

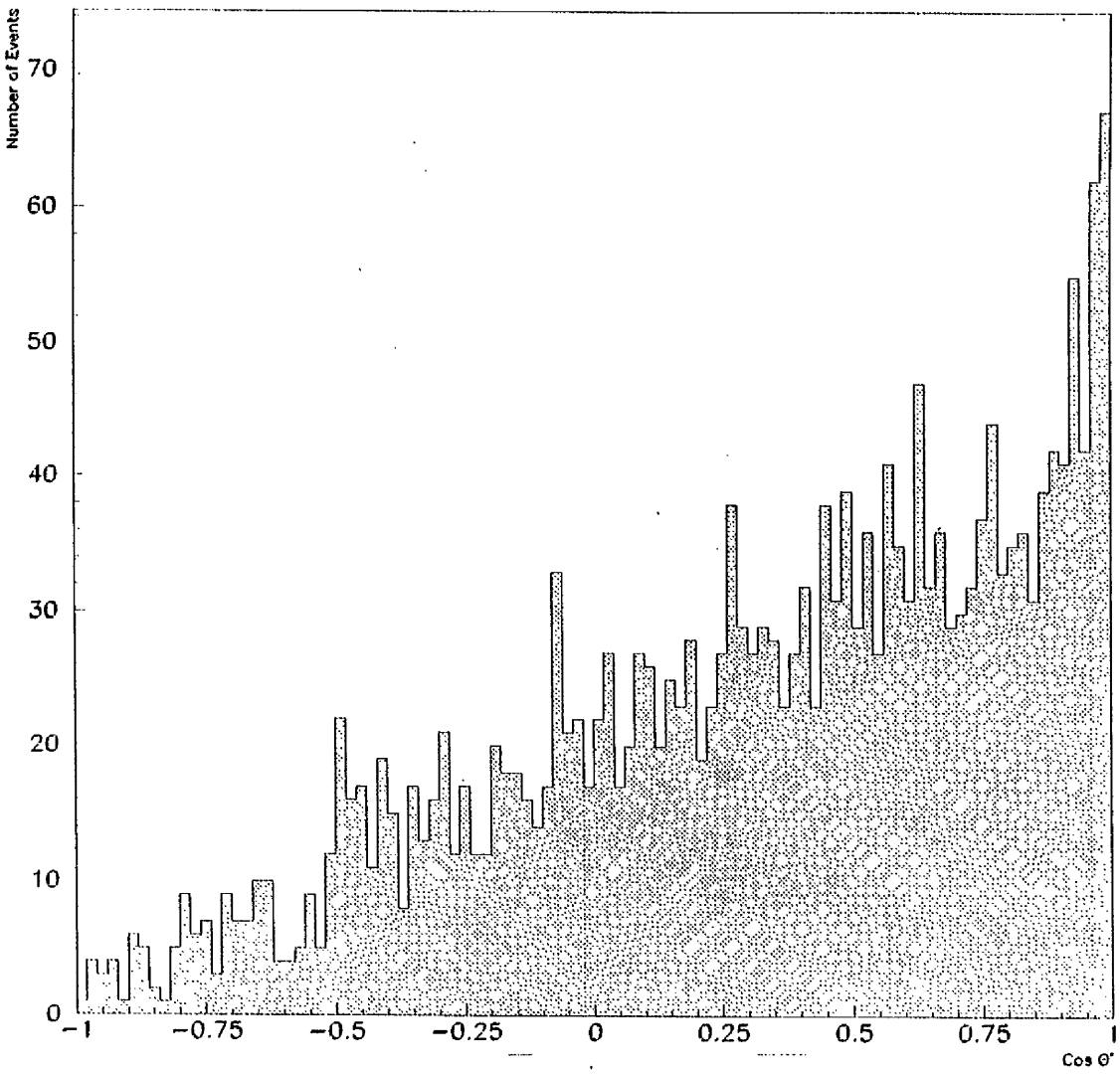

Figure 6.7: The $(1 + \cos\theta^*)$ decay angular distribution of an excited electron in its rest frame.

With these distributions in mind, and the $(1 + \cos\theta^*)$ decay angular distribution of the e^* in its rest frame with θ^* relative to the electron beam direction (Fig. 6.7), the distributions of the decay products can be understood.

6.1.2 The $e\gamma$ Decay Products

The lab energy, polar and azimuthal angle distributions of the electron and photon decay particles are shown in Figures 6.8, 6.9, 6.10. The energy of the decay products is high, typically $> 15\ GeV$. The distribution of decay product θ over the mass range of interest is peaked in the forward, proton, direction for both electrons and photons. At masses above 60 GeV, i.e most of the events in the sample, the excited electron is produced moving in the proton direction therefore boosting the decay products forward. The tendency of the decay electrons to be preferentially emitted in the beam electron direction results in the observed distribution being less forward peaked than that of the photons.

The distribution is, as is to be expected, uniform in ϕ.

In the rest frame of the excited electron the decay products obviously come off back to back in ϕ. However, the ϕ separation in the lab will depend on the Q^2 of the exchange photon, since this effectively provides the e^* with p_T, and therefore on the 4-momentum of the e^* in the lab. Figure 6.11 shows the azimuthal angle between the decay electron and photon in the lab. The distribution is strongly peaked at 180° due to the near beam axis direction of motion of the e^*'s and low Q^2 dominance in the production process.

6.1.3 Invariant Mass

To reconstruct the excited electron state from the decay products the invariant mass of the system is calculated. This makes use of the fact that, if a particle is produced on mass shell $(E^2 - p^2 = m^2)$, then any subsequent system of particles resulting from its decay will have the same invariant mass, the mass of the excited electron in this case.

Thus taking the decay electron and photon the reconstructed invariant mass of the system is given by

$$M^2_{\mathbf{inv}} = 4E_e E_\gamma \sin^2\left(\frac{\theta}{2}\right) \tag{6.5}$$

where θ is the opening angle between the decay particle 4-vectors given by

$$\begin{aligned} |\mathbf{p}_e||\mathbf{p}_\gamma| \cos\theta &= \mathbf{p}_e \cdot \mathbf{p}_\gamma \\ \cos\theta \simeq & \frac{\mathbf{p}_e \cdot \mathbf{p}_\gamma}{E_e E_\gamma} \end{aligned} \tag{6.6}$$

Figure 6.12 shows the invariant masses reconstructed from the decay products using these expressions for the sample of e^*'s generated in sets of 100 at 10 GeV mass intervals.

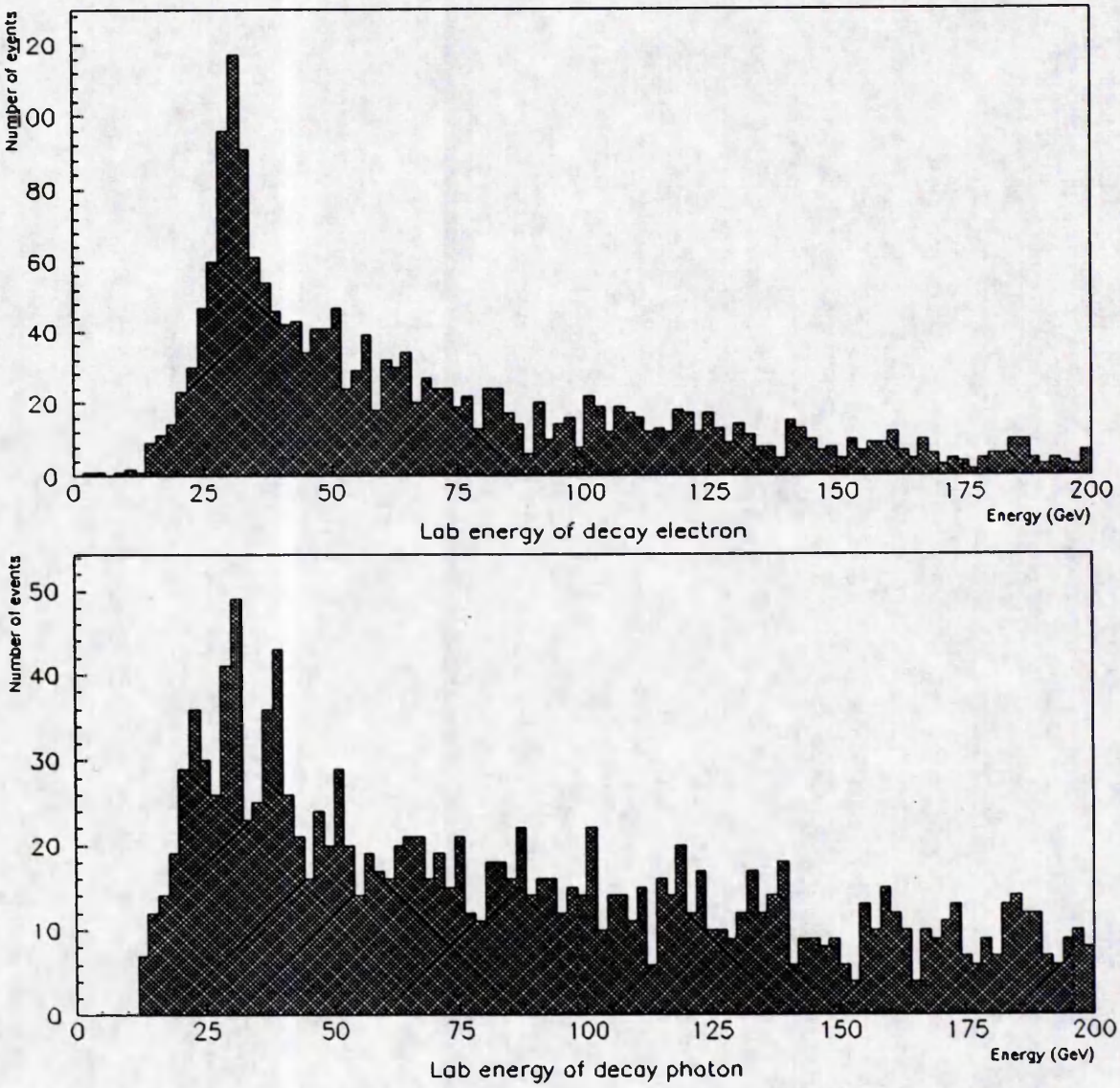

Figure 6.8: The lab energy distributions of the $e^* \rightarrow e\gamma$ decay particles

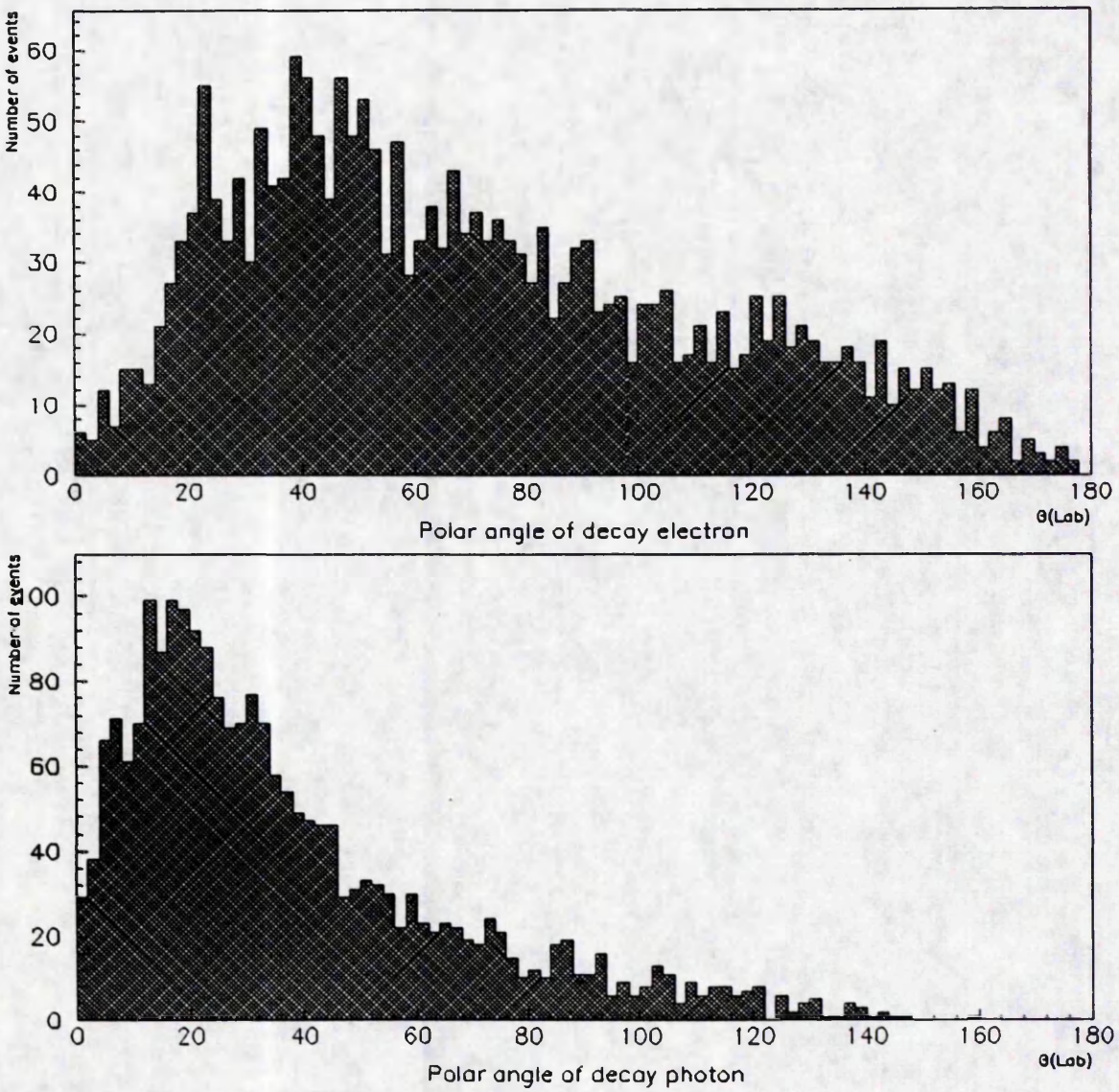

Figure 6.9: The polar angle distributions of the $e^* \rightarrow e\gamma$ decay particles

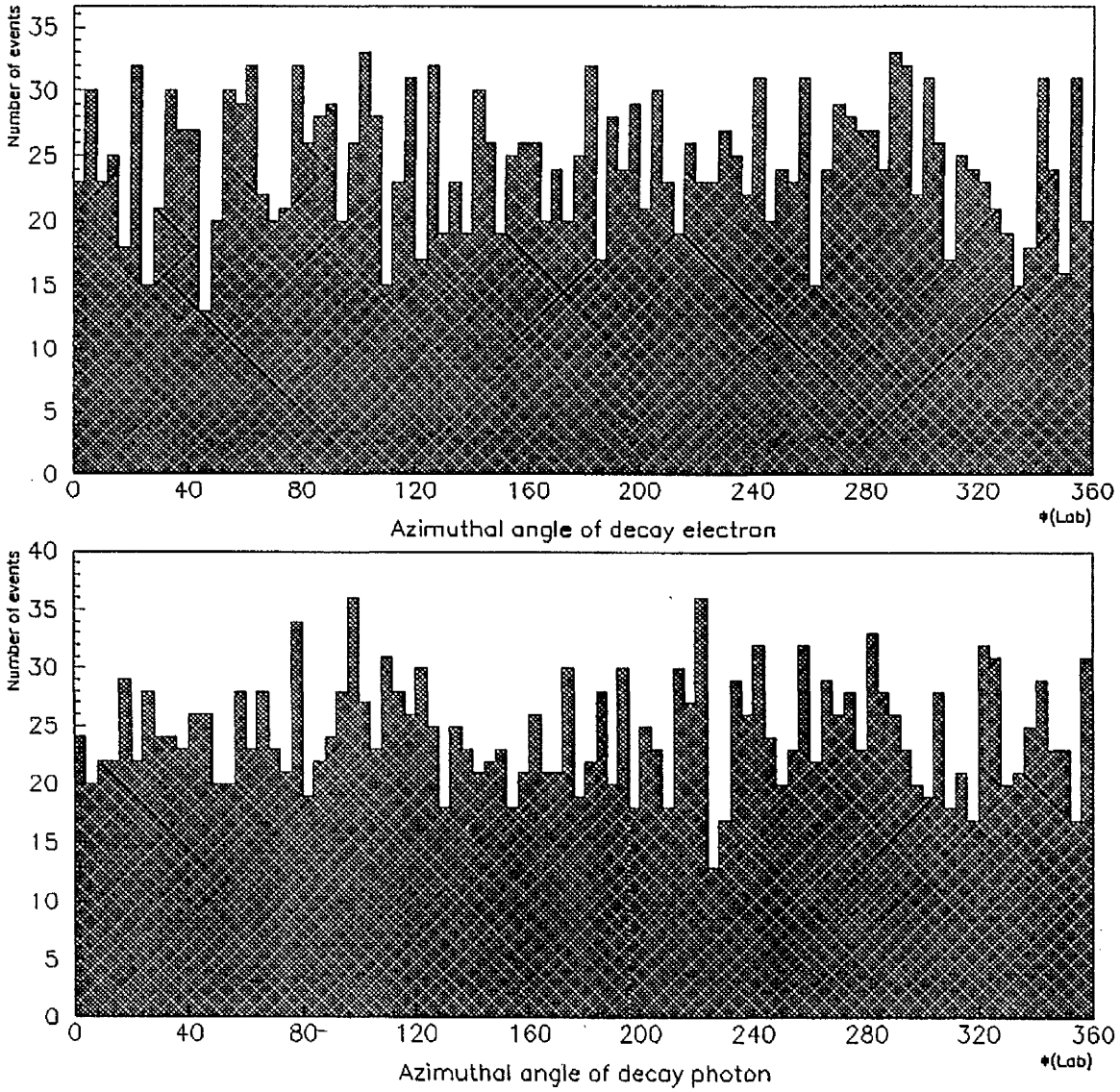

Figure 6.10: The azimuthal angle distributions of the $e^* \rightarrow e\gamma$ decay particles

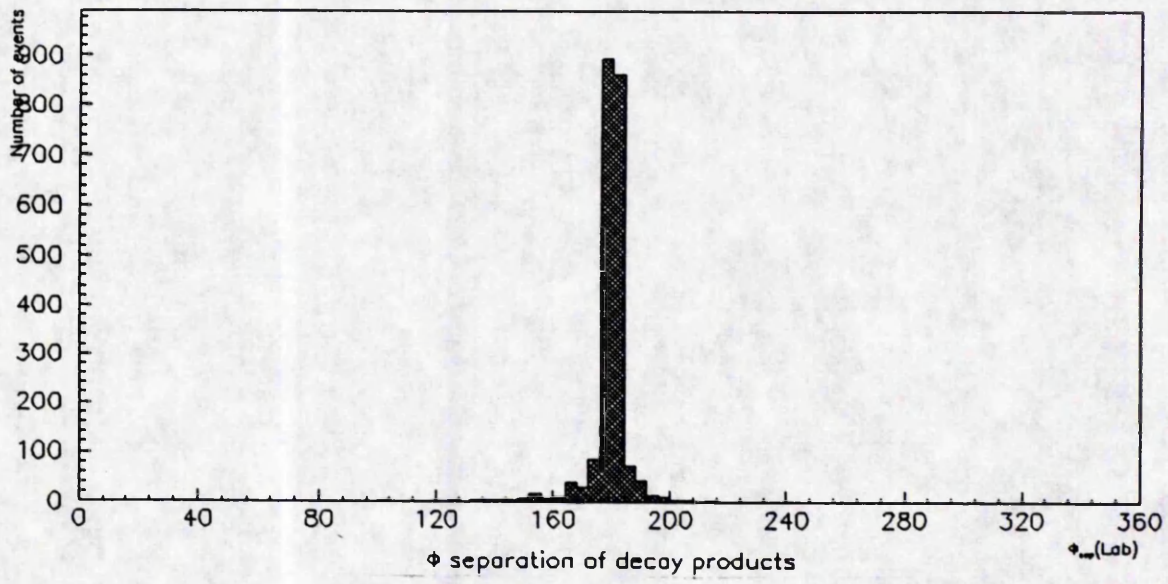

Figure 6.11: The azimuthal angle separation of the $e^* \rightarrow e\gamma$ decay particles

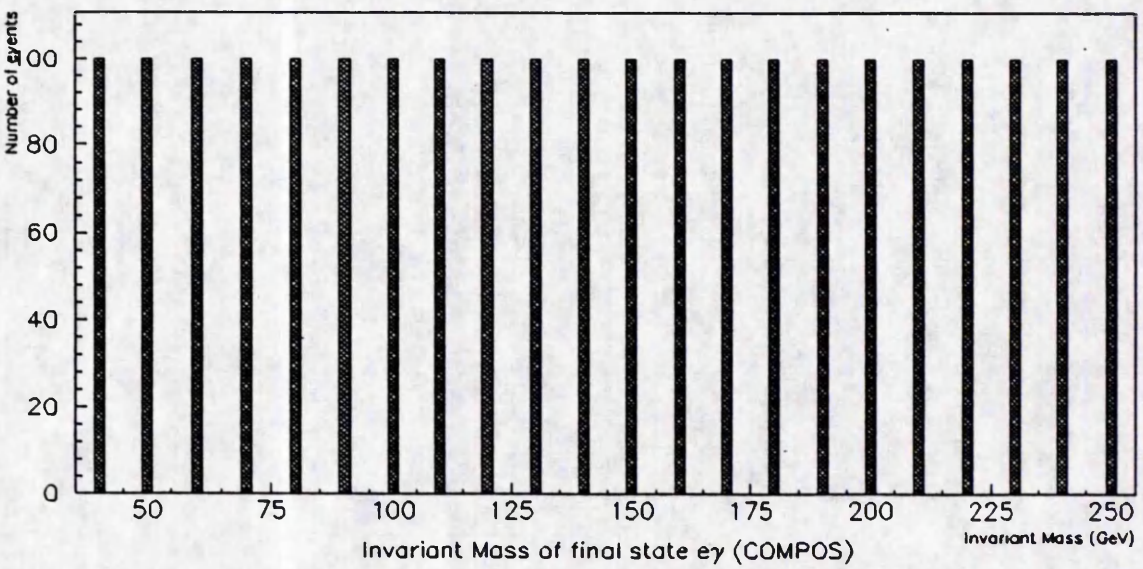

Figure 6.12: Reconstructed Invariant Mass of the $e\gamma$ decay particles

6.1.4 Basic Event Selection Criteria

Using these results therefore one has several basic selection criteria for e^* candidate events;

- Two energetic ($E >\sim 15\ GeV$) electromagnetic clusters.
- One cluster identified as electron.
- Other cluster identified as photon.
- $120° < |\phi_{\mathbf{sep}}(e\gamma)| < 240°$.
- Large opening angle between the electron and photon.
- Reconstructed invariant mass $> \approx 40\ GeV$.

6.2 A Comment on Final State Distributions

As has been discussed previously, there is no way to tell an e^* from a bremsstrahlung event reconstructing to the same invariant mass on an event by event basis. However, given a sample of similar events, i.e of the same $e\gamma$ final state invariant mass, then distinct differences in the distributions between the two types of events become apparent.

Datasets (2000 events in each) were generated with COMPOS and EPCOMPT for e^* ($M(e^*) = 40,\ 80,\ 120,\ 160\ GeV$) and wide angle bremsstrahlung events ($M_{\mathbf{inv}}(e\gamma) = 40,\ 80,\ 120,\ 160\ GeV$) to directly compare the distributions for final states corresponding to the same e^* mass candidate.

The distributions of polar angle, energy and opening angle of the electron and photon are shown in Figures 6.13 - 6.17 for 2000 events of each $M_{\mathbf{inv}}$.

These distributions are very different for the e^* and bremsstrahlung events. The differences can be exploited to improve the signal to background ratio when looking for a specific mass excited electron or when there is a possible candidate in the data sample yielded by the selections developed in this study. However, since this work deals with a general search procedure, cuts which would significantly improve resolutions for specific e^* masses, for example looking for 120 GeV candidate by requiring $E_\gamma > 50\ GeV$ and $E_e < 100\ GeV$, (Figures 6.15, 6.16), would be very effective in reducing bremsstrahlung backgrounds of the same reconstructed invariant mass but would also seriously degrade signal from e^*'s of any other masses.

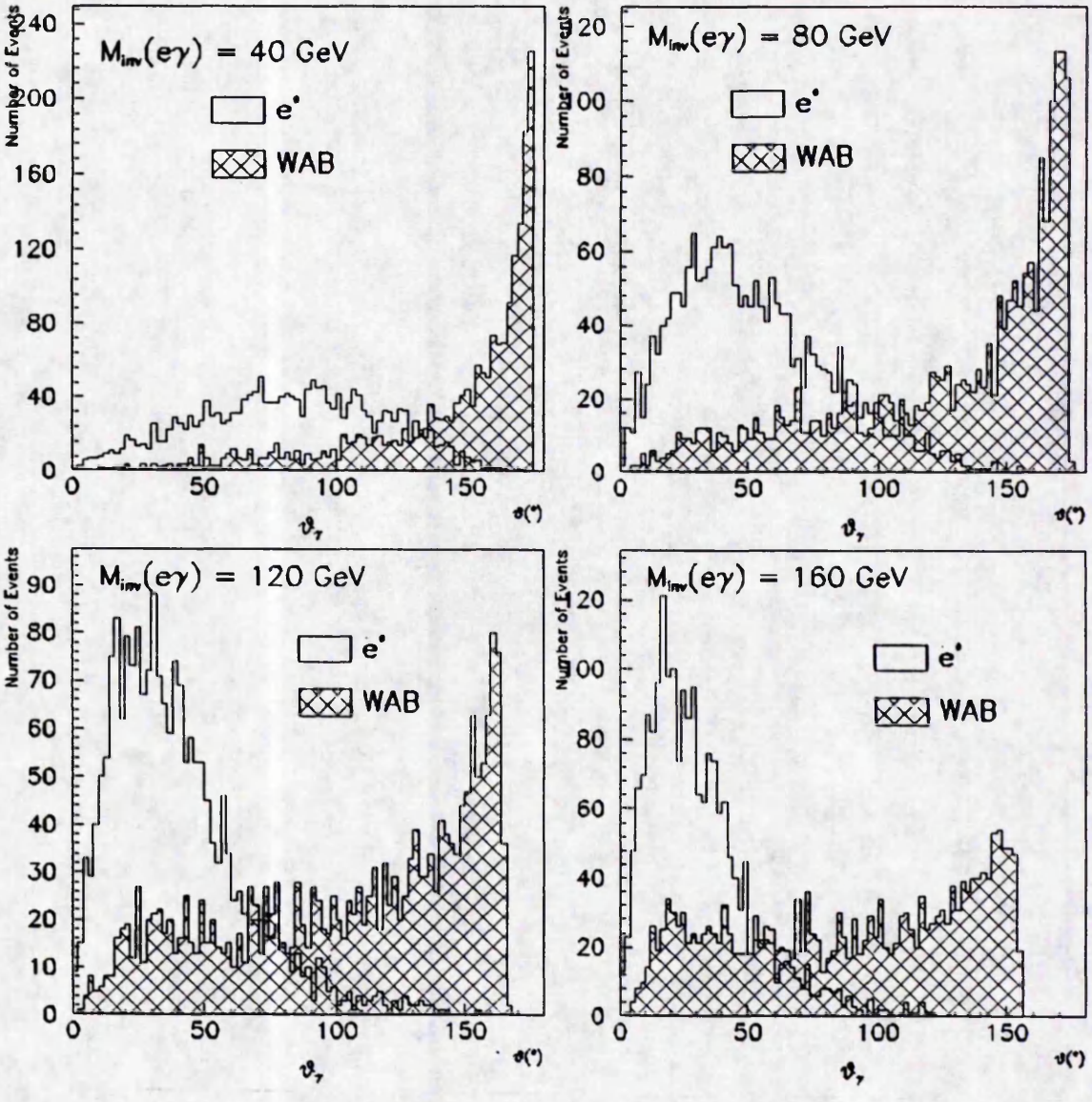

Figure 6.13: Polar angle distributions of final state photons in e^* and wide angle bremsstrahlung events.

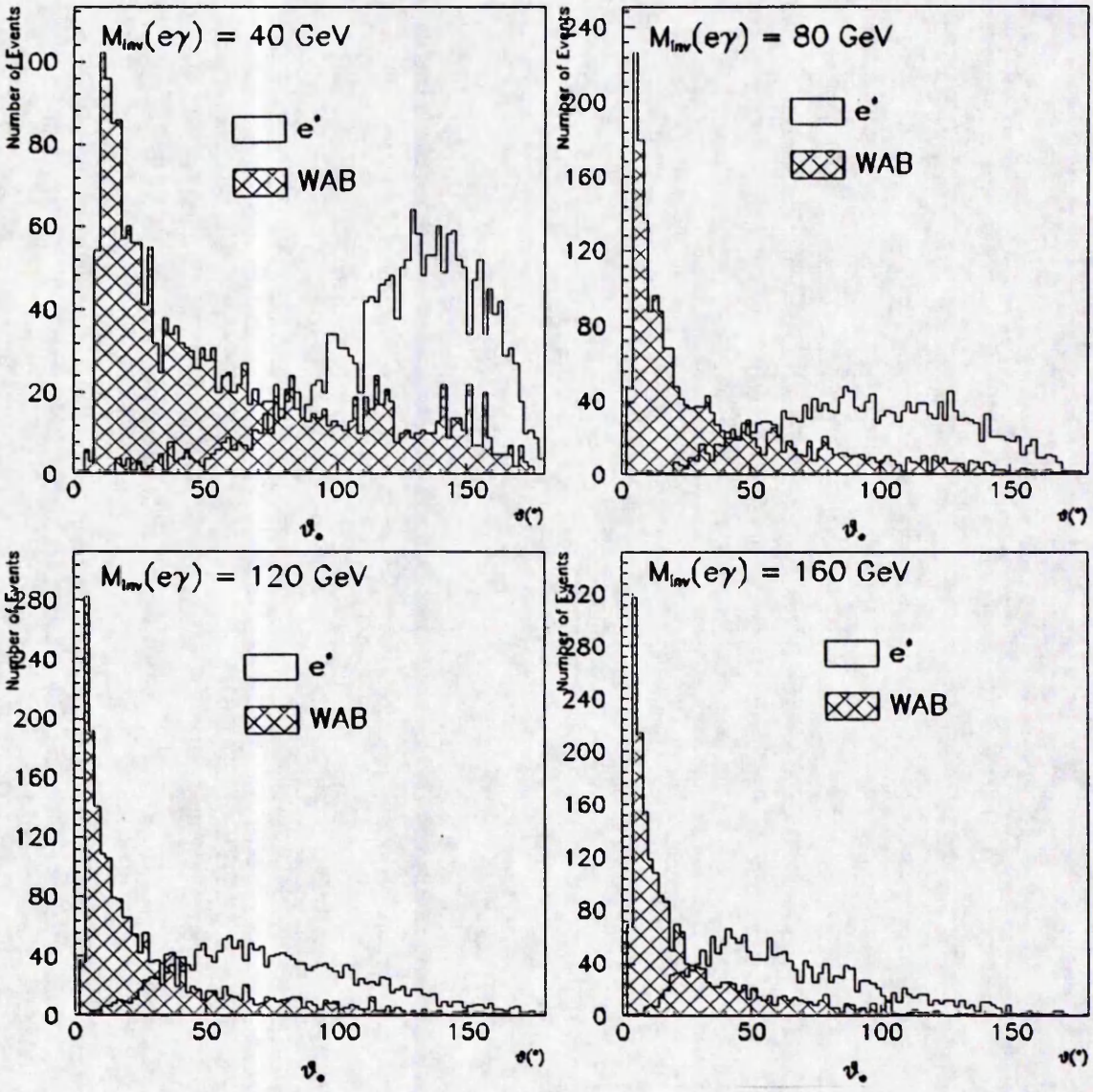

Figure 6.14: Polar angle distributions of final state electrons in e^* and wide angle bremsstrahlung events.

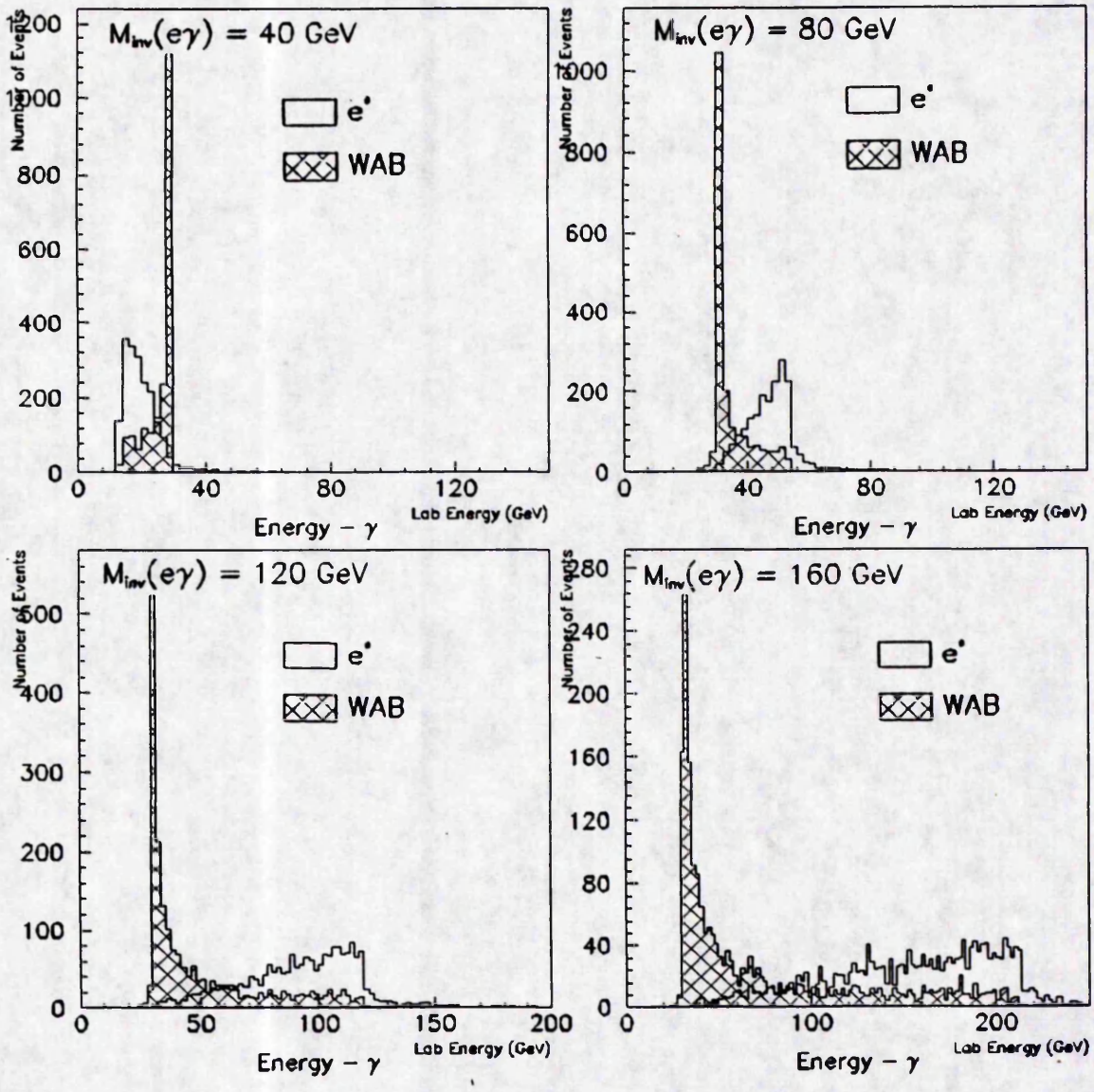

Figure 6.15: Energy distributions of final state photons in e^* and wide angle bremsstrahlung events.

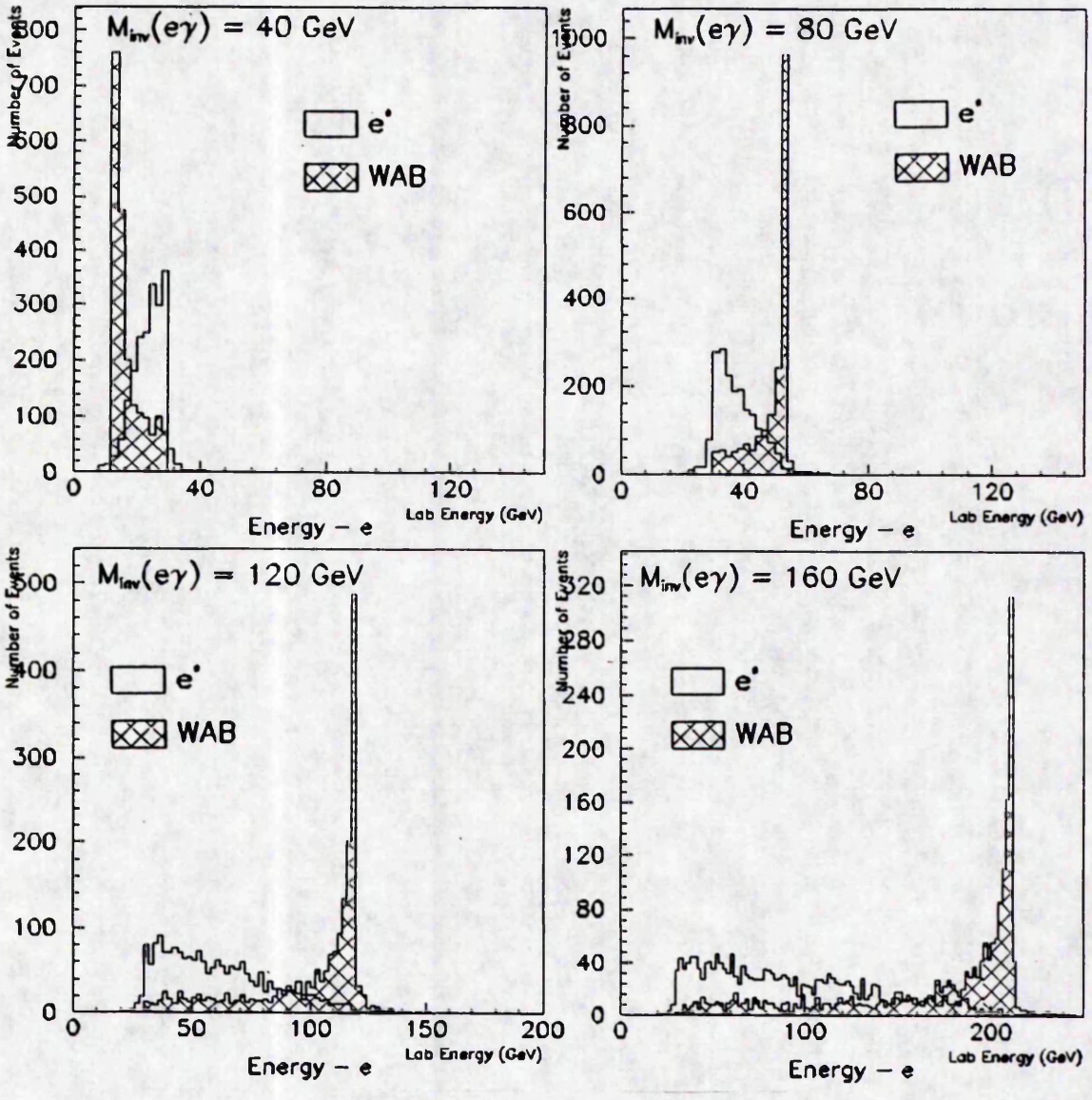

Figure 6.16: Energy distributions of final state electrons in e^* and wide angle bremsstrahlung events.

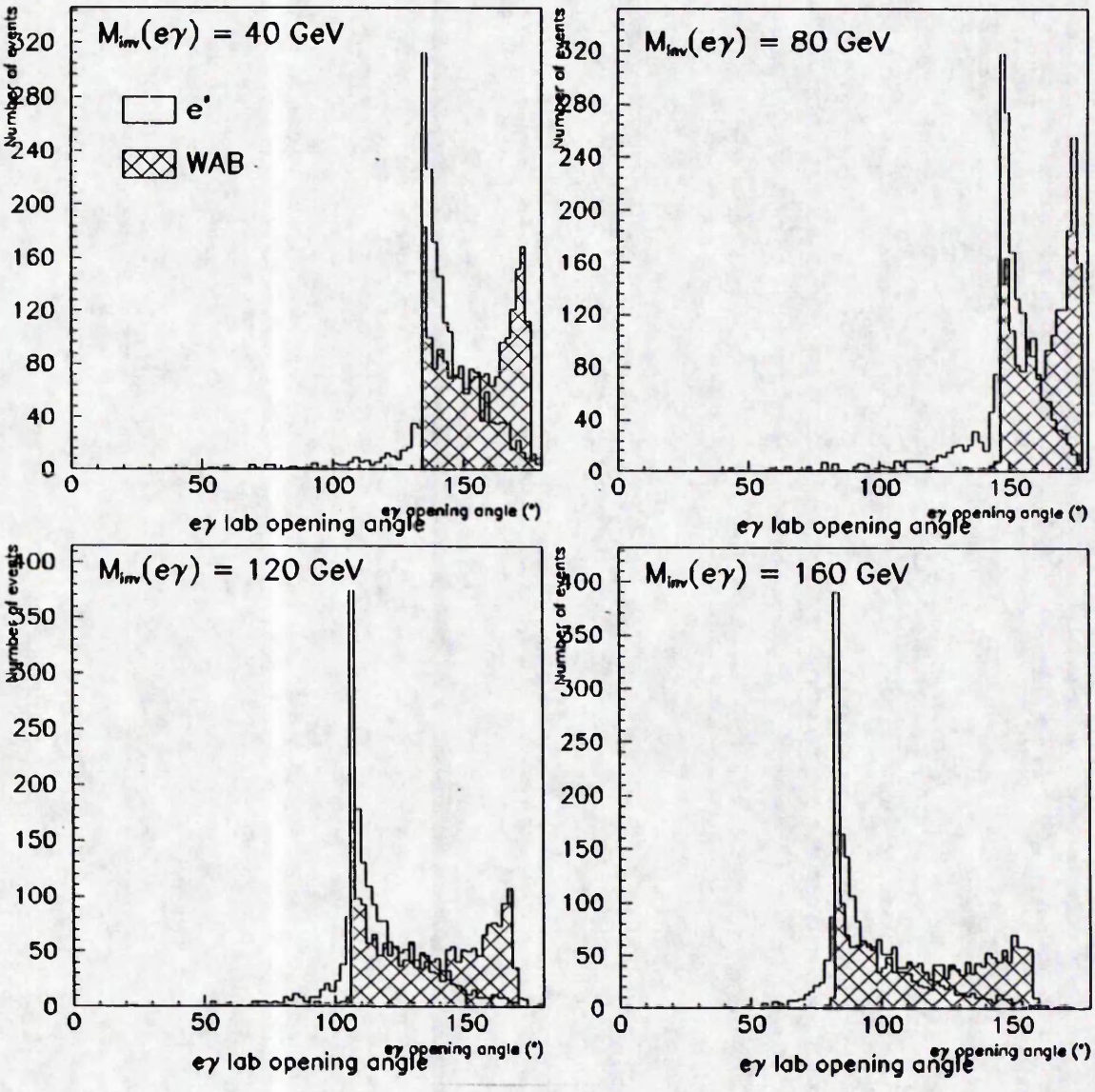

Figure 6.17: Final state $e\gamma$ lab opening angles for e^+ and wide angle bremsstrahlung events.

Use of these features should definitely be made for more detailed searches of data and therefore the limits on discovery mass with luminosity and Λ presented here must be viewed as the most conservative resulting from the most general search procedure.

6.3 Signal and Background in H1PSI

An advantage of using the fast Monte Carlo H1PSI is that it is possible to generate and simulate full data samples equivalent to years of running for both signal and the backgrounds anticipated here.

The program outputs for each event processed information on reconstructed tracks, clusters, triggers and the relevant measurement errors. The basic excited electron selection procedure is

- Require at least 2 reconstructed clusters in the event with $E > 15\ GeV$ and electromagnetic fraction > 90 %. Candidate decay $e\gamma$ clusters.
- Lateral size of both clusters consistent with one particle.
- One candidate cluster has no tracks pointing towards it - photon candidate
- One candidate cluster has 1 track pointing towards it with tracker and calorimeter measurement $\chi^2_E,\ \chi^2_{\theta,\phi} < 3.$ - electron candidate.
- Separation in $\phi = 180° \pm 60°$.
- Q^2 reconstructed from electron $>\ 100\ GeV^2$.
- $M_{\mathbf{inv}}(e\gamma) > 35\ GeV$.

The large opening angle between the decay products, and the tendency of the struck quark jet to be confined to low θ (low Q^2) results in the electron and photon being isolated in space. Therefore, the requirement that neither the electron nor photon cluster candidate have any other tracks associated with it appears a reasonable one.

6.4 Performance of the Cuts

Using these cuts the efficiency for selecting excited electron events can be studied and a first examination of problematic wide angle bremsstrahlung and DIS events made.

The trigger efficiency on all these events is > 99% due to the large transverse energy deposition in the calorimeter and is not considered further.

6.4.1 e^* Signal Losses with Basic Analysis Cuts

The basic event selection cuts are such that one would expect to retain the majority of the excited electron events. Losses in the low mass region can be anticipated from the requirements that both decay products have $E > 15GeV$ and the reconstructed $Q^2 > 100GeV^2$. These are both very dependent on m_{e^*}, as mass increases so the average decay product energy and reconstructed Q^2 increases. One would therefore expect losses in the lower mass region due to these cuts but these should be negligible at higher masses. The requirement that the decay products have $\phi_{\mathbf{sep}} = 180° \pm 60°$ can also be expected to affect the lower masses more. Figure 6.3 shows the decreasing variation in θ_{e^*} as m_{e^*} increases, thus there is less p_T available from the motion of the e^* in the lab frame to boost the decay products away from back to back in ϕ.

Extra event losses must be understood in terms of detector effects.

Event samples consisting of 1000 e^* s of each mass in the range $40-250\ GeV$ at $10\ GeV$ intervals were processed by H1PSI. The event loss statistics are summarised in Table 6.1.

A small, fairly constant, number of events are lost with no reconstructed tracks. This corresponds to situations where the decay electron θ is such that there were not enough hits in the tracking detectors to reliably construct a track with, i.e. low and high θ electrons.

After a pronounced loss of low mass e^*'s on the electromagnetic cluster selection there is a more-or-less uniform loss of events by the cut. The losses at lower masses are attributable to the lower energies of the decay electrons and photons failing to pass the $15\ GeV$ minimum while the near constancy after that represents almost exclusively a failure on the 90% electromagnetic fraction cut. This fraction can in no way be interpreted as a real containment problem since it is far greater than expected from a $20 - 30X_{\mathbf{rad}}$ deep calorimeter. There is no observed geometric or mass dependency to the effect. Therefore it is likely that this is a H1PSI feature rather than a real effect probably due to some scaling factor introduced to simulate noise in the calorimeter which does not appear to be energy dependent and overestimates the loss of physics in the high energy regime represented by the excited electron events.

This will introduce an small underestimation of event selection efficiencies to be cal-

culated which if anything will make results slightly more pessimistic than they need be.

Events lost on the Q^2 cuts clearly decrease as the e^* mass increases, reflecting the increasing transverse momentum available to the decay electron.

Failure to identify a candidate cluster as an electron results from χ^2 failure on energy or position matching of tracker and calorimeter measurements. Levels are higher than one would expect from just statistical considerations, which is to be expected due to reduced accuracy of error estimation of tracks as momentum increases and the particle trajectory in the $x - y$ plane approaches that of a straight line.

Photon losses are due to tracks being associated with the photon cluster and levels are small.

6.4.2 A Note on Photon Conversions

There is a finite chance that the high energy photons in the events under study will convert to electron-positron pairs on passage through the beam-pipe and tracker volume and thus be lost on the requirement that a photon candidate cluster has no tracks pointing to it.

Table 6.2 shows the percentage reduction in event identification efficiency for e^* events processed by H1PSI with photon conversions in the tracker volume switched on in the detector simulation compared to the situation where no conversions are included.

This clearly shows that the effect is more important for the higher mass e^* events. The more material a photon passes through, the greater the probability that it will pair produce. As has been seen previously the decay photons tend to be boosted further forward in the detector as e^* mass increases, therefore they tend to traverse more material in the beam-pipe as angle of incidence moves away from normal. There is also the material in the end walls of the central track detector and face of the forward track detector to consider at $\theta < 35°$. These factors combine to increase the probability of conversion in the tracker volume.

Thus one increasingly loses signal as the production cross section decreases. The events could be retained if the photon candidate criteria were relaxed to take into account cases where an e^+e^- pair is associated with an energetic electromagnetic cluster. However this also introduces the possibility of new backgrounds and is not considered in this work where the emphasis is on a search for e^*'s using relatively straightforward selection criteria.

H1PSI is therefore run with photon conversions in the tracker volume switched on with

e^* mass (GeV)	No Tracks Reconstructed	< 2 Energetic Electromagnetic Clusters	Q_e^2 $< 100\ GeV^2$	Failed to Find Electron	Failed to Find Photon	$\|\phi_{sep}\|$ Failure
40	1.1 ± 0.3	28 ± 2	1.9 ± 0.4	1.6 ± 0.4	0.6 ± 0.2	4.1 ± 0.6
50	0.2 ± 0.1	13 ± 1	6.9 ± 0.8	4.0 ± 0.6	0.2 ± 0.1	4.0 ± 0.6
60	0.3 ± 0.2	13 ± 1	3.6 ± 0.6	2.3 ± 0.5	0.4 ± 0.2	4.3 ± 0.7
70	0.5 ± 0.2	15 ± 1	3.3 ± 0.6	2.5 ± 0.5	0.2 ± 0.1	3.2 ± 0.6
80	0.2 ± 0.1	15 ± 1	2.1 ± 0.5	2.9 ± 0.5	0.4 ± 0.2	1.3 ± 0.4
90	0.1 ± 0.1	17 ± 1	1.1 ± 0.3	2.1 ± 0.5	0.7 ± 0.3	1.0 ± 0.3
100	0.2 ± 0.1	16 ± 1	0.7 ± 0.3	2.4 ± 0.5	0.1 ± 0.1	0.8 ± 0.3
110	0.2 ± 0.2	16 ± 1	0.3 ± 0.2	3.6 ± 0.6	0.8 ± 0.3	0.7 ± 0.3
120	0.3 ± 0.2	16 ± 1	0.4 ± 0.2	3.3 ± 0.6	0.7 ± 0.3	0.8 ± 0.3
130	0.1 ± 0.1	16 ± 1	0.3 ± 0.2	3.2 ± 0.6	0.6 ± 0.2	0.5 ± 0.2
140	< 0.1	15 ± 1	< 0.1	4.1 ± 0.6	0.7 ± 0.3	0.7 ± 0.3
150	0.2 ± 0.1	16 ± 1	0.1 ± 0.1	3.7 ± 0.6	0.3 ± 0.2	0.2 ± 0.1
160	0.1 ± 0.1	15 ± 1	0.1 ± 0.1	4.7 ± 0.7	0.3 ± 0.2	0.1 ± 0.1
170	< 0.1	18 ± 1	0.1 ± 0.1	3.6 ± 0.6	0.9 ± 0.3	0.1 ± 0.1
180	< 0.1	15 ± 1	< 0.1	4.9 ± 0.7	–	0.1 ± 0.1
190	< 0.1	16 ± 1	< 0.1	4.4 ± 0.6	–	0.2 ± 0.1
200	0.1 ± 0.1	13 ± 1	< 0.1	6.3 ± 0.7	–	0.2 ± 0.1
210	0.2 ± 0.1	16 ± 1	< 0.1	5.6 ± 0.7	–	0.1 ± 0.1
220	0.2 ± 0.1	16 ± 1	< 0.1	5.1 ± 0.7	–	0.2 ± 0.1
230	0.1 ± 0.1	14 ± 1	< 0.1	6.4 ± 0.8	–	< 0.1
240	0.4 ± 0.2	15 ± 1	< 0.1	5.5 ± 0.7	–	0.1 ± 0.1

Table 6.1: Percentage signal loss using the basic event selection.

the same isolation event selection requirement.

6.4.3 The Wide Angle Bremsstrahlung Cuts

In the comparison of the final state distributions of e^* and wide angle bremsstrahlung events (see Section 6.2) it was noted that the exploitation of the differences as cuts will be important in more mass specific searches. However, one feature which can be used in this work is the different polar angle θ distributions of the final state photons.

Figure 6.13 illustrates the dominance of backward going photons in bremsstrahlung events with $M_{\mathbf{inv}}(e\gamma)$ extending over a large range of interest here while for excited electron events the region is relatively unpopulated.

Therefore, a maximum θ_γ cut can only improve the signal to background ratio.

A data sample of bremsstrahlung events with $M_{\mathbf{inv}} > 25\ GeV$ was generated using

e^* mass (GeV)	% Reduction in Event Identification efficiency
40	1.7 ±0.6
50	3.5 ±0.7
60	6.5 ±0.9
70	8.9 ±1.1
80	11.9 ±1.2
90	8.9 ±1.1
100	11.0 ±1.2
110	11.8 ±1.2
120	12.8 ±1.3
130	11.2 ±1.2
140	11.5 ±1.2
150	13.0 ±1.3
160	12.3 ±1.2
170	14.9 ±1.4

Table 6.2: Percentage of events lost through photon conversions for various excited electron masses.

EPCOMPT and processed by H1PSI and the basic e^* event selection cuts of Section 6.3.

The distribution of final state photon polar angle θ with $M_{\mathbf{inv}}$ is shown in Figure 6.18 for 4784 events passing these selection cuts.

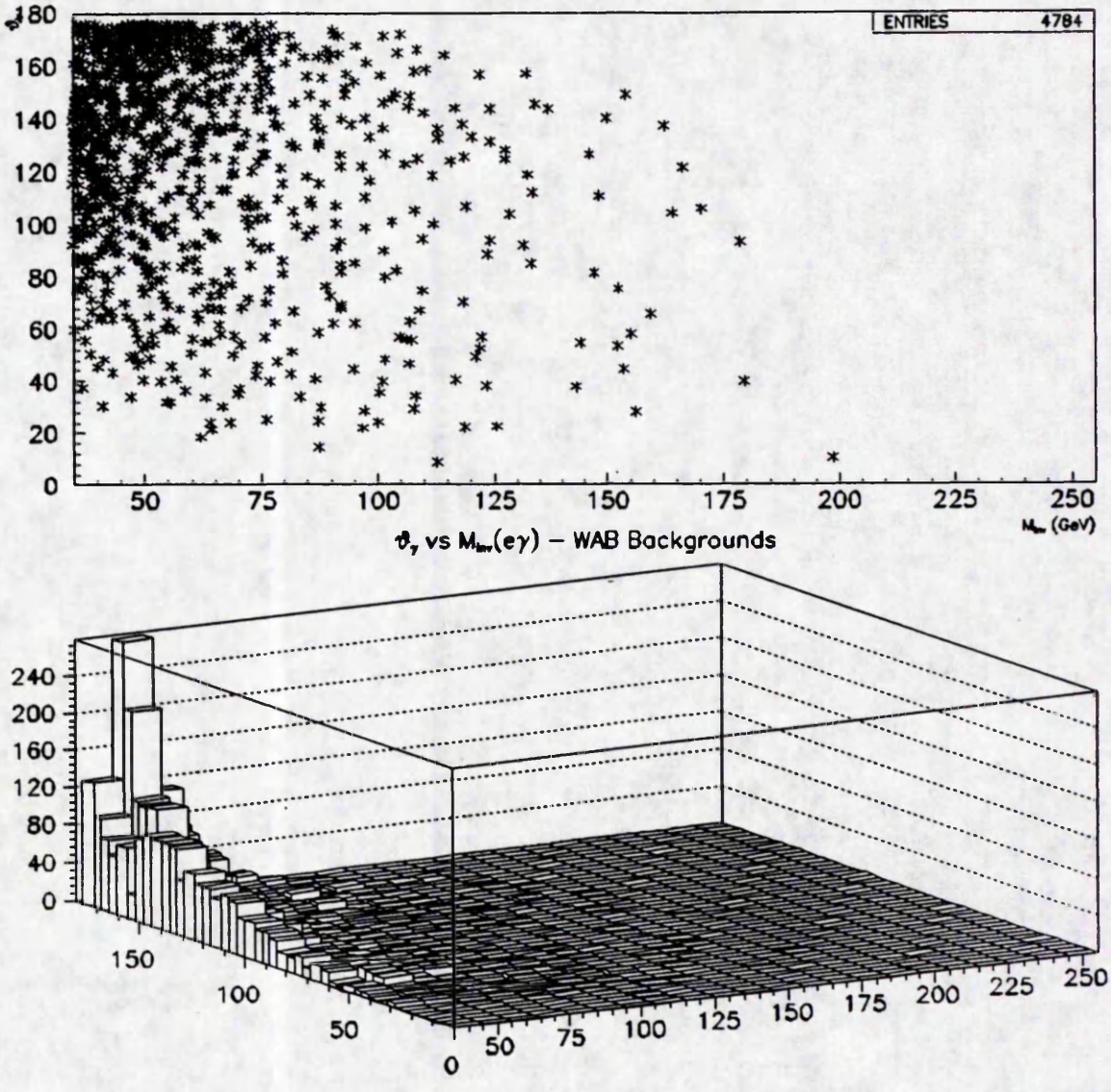

Figure 6.18: θ_γ vs $M_{\mathbf{inv}}$ for wide angle bremsstrahlung events passing basic e^* selection cuts.

The tendency of photons to be backward going over a large range of masses of interest can be seen. Comparing these results with those of Figure 6.9 which shows the θ distribution of the e^* decay products shows that requiring a maximum θ_γ of 140° significantly reduces bremsstrahlung backgrounds for a small loss in the e^* signal which is restricted to

the lower mass, higher cross section, region.

Figure 6.19 shows the effect of such a cut on the invariant mass distribution of wide angle bremsstrahlung backgrounds. The number of events remaining is 2122, a reduction in background signal of approximately $55 \pm 1\%$. The reduction falls off as $M_{\mathbf{inv}}$ increases, reflecting the trend of higher $M_{\mathbf{inv}}$ wide angle bremsstrahlung backgrounds to have the θ_γ distribution less backward dominated, see Figure 6.13.

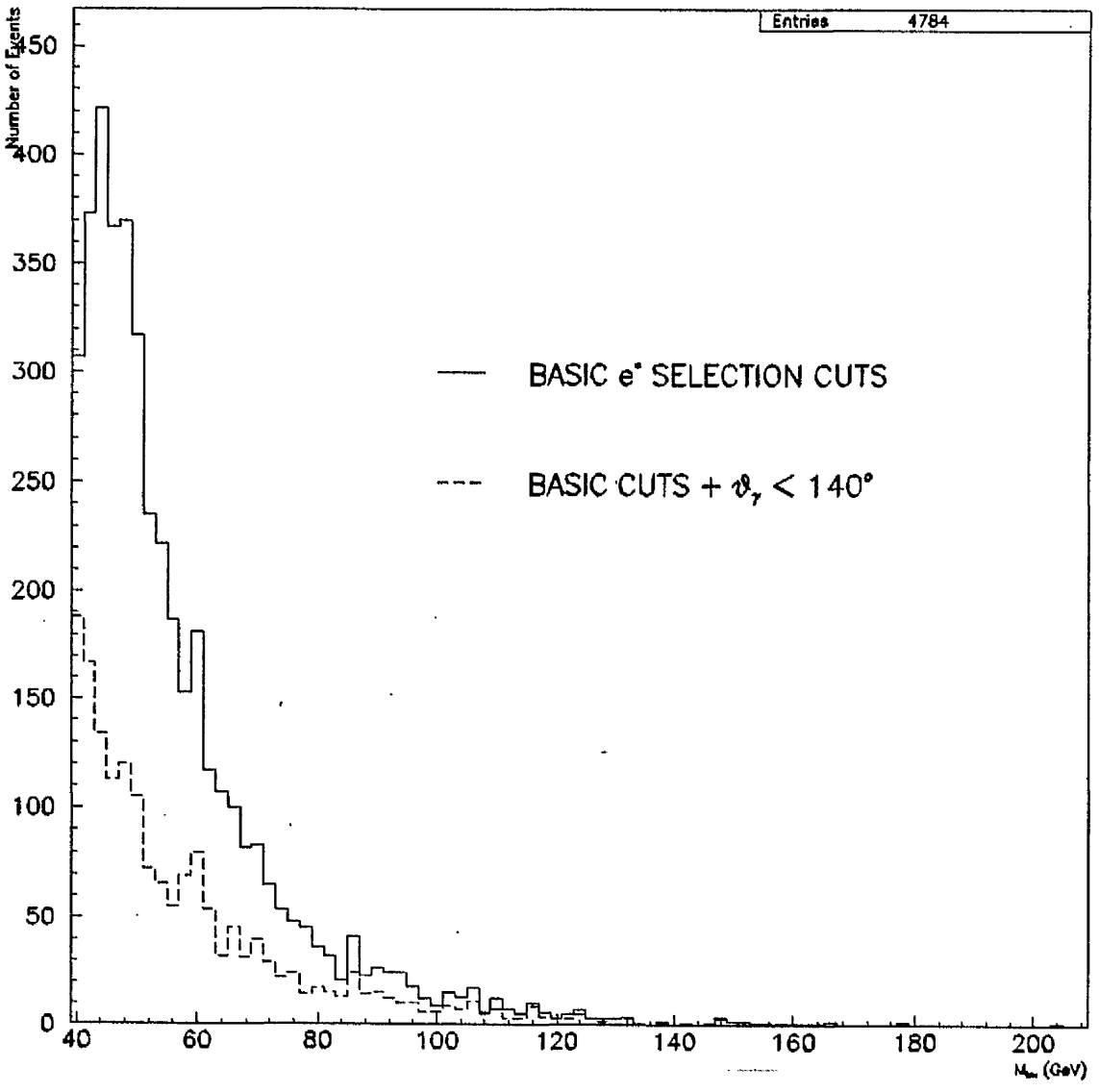

Figure 6.19: The invariant mass distribution of wide angle bremsstrahlung events passing the basic e^* selection cuts before and after the $\theta_\gamma < 140°$ cut.

6.4.4 The Neutral Current DIS Background Cuts

There is no reliable way of anticipating the class of neutral current deep inelastic physics which is problematic for excited electron event selection so there is no safe alternative but to generate a representative event sample, study the candidate events and use the information to propose further cuts. The aim of the further cuts is to ultimately yield a set of candidate events from H1 data where one is confident that the level of DIS backgrounds is small, thus reducing the effects of assumptions about the distribution of these backgrounds which is difficult due to the unpredictable source of problematics.

The first sample of events processed by H1PSI was generated with $Q^2 > 100\ GeV^2$ only. The details of dataset I can be found in Table 6.3. The level of events which passed the basic event selection cuts for candidate e^*'s corresponds to $\approx 12\ pb$. The invariant mass distribution and the reconstructed Q^2 of these events is shown in figure 6.20(a). This shows clearly the effectiveness of a $Q^2_{\mathbf{rec}} > 300\ GeV^2$ cut for rejecting DIS backgrounds over a wide range of invariant masses.

DATASET	LEPTO 5.2 data sample cuts	Integrated Cross Section (pb)	Number of Events Processed	$\equiv \int \mathcal{L}$ (pb^{-1})
I	$Q^2 > 100\ GeV$ only	$4,664 \pm 21$	26,148	5.61 ± 0.03
II	$Q^2 > 300\ GeV$ only	$1,100 \pm 5$	25,593	23.3 ± 0.1
III	$Q^2 > 100\ GeV$ ≤ 1 track with $\theta > 25°$ and $E > 1\ GeV$	$1,850 \pm 4$	184,934	100.0 ± 0.2
IV	$Q^2 > 300\ GeV$ ≤ 1 track with $\theta > 25°$ and $E > 1\ GeV$	369 ± 1	104,493	283 ± 1

Table 6.3: The DIS background event samples.

A $Q^2 > 300\ GeV^2$ cut is also useful when generating DIS background representative of a reasonable integrated luminosity from HERA (1 year's data expected to be $\simeq 100\ pb^{-1}$). Thus, the LEPTO data sample II was generated with a $Q^2 > 300\ GeV^2$ cut, (Table 6.3).

Figure 6.21 shows the invariant mass plot and the number of tracks with $\theta > 20°$ for the events which pass the e^* analysis cuts.

Of 25,593 events, 63 survive the analysis cuts corresponding to a cross section of $\approx 3\ pb$. Of these none have less than 3 reconstructed tracks located centrally ($\theta > 20°$) in the detector. This can be compared with the excited electron events from section 6.1 where $\approx 80\%$ of events have less than 2 such central tracks, reflecting the low Q^2 dominance in the inelastic e^* production process. Restricting the event sample to those with just one energetic track at reasonable θ is in keeping with the aim of looking for distinctive event signatures and a sample relatively free of DIS contamination without resorting to the powerful cluster multiplicity cut (Number of clusters in event = 2) which kills all DIS at the expense of the deep inelastic e^* signal.

The new selection criteria which now also require, in addition, a maximum of one central track were then tested on the LEPTO event sample III (Table 6.3) representing 100.0 pb^{-1} of potential DIS backgrounds. Figure 6.22(a) shows the invariant mass plot of the events which survive the new set of analysis cuts, these correspond to a cross section of $\approx 0.6\ pb$ of surviving DIS background. However, Figure 6.22(b,c) shows the relation between invariant mass and θ_γ for both DIS fake events and real e^* events.

The form of the distribution for excited electron events has been previously discussed (see section 6.1.2). Far forward going photons tend to be associated with high mass states.

The case for the DIS background is quite different. Here, because the energy of the scattered electron is close to beam energy, and it is always the scattered electron which is identified with the decay electron, there are no cases of mis-identified pions in the problematic events, it is the photon candidate that has to generate the high invariant mass. In DIS events the most likely place these are to be found are in tight clusters of forward going photons from the struck quark jet. In the problem events these are sufficiently isolated from other jet fragments to reconstruct as single photon candidates. However, the energy is not, on the whole, as high as the authentic decay photons usually found in this θ region and so the reconstructed invariant mass is lower than in true events.

A simple cut on minimum θ_γ would lose these low mass fakes at the expense of high mass (low cross section) signal and would therefore be unproductive. Instead, a better cut makes use of the different θ_γ, $M_{\mathbf{inv}}$ distributions.

The function superimposed on both plots is

$$\theta_\gamma = \exp(5.7 - 0.05 M_{\mathbf{inv}}) \tag{6.7}$$

at θ_γ below these values one would expect to find few real events but a significant fraction of DIS background.

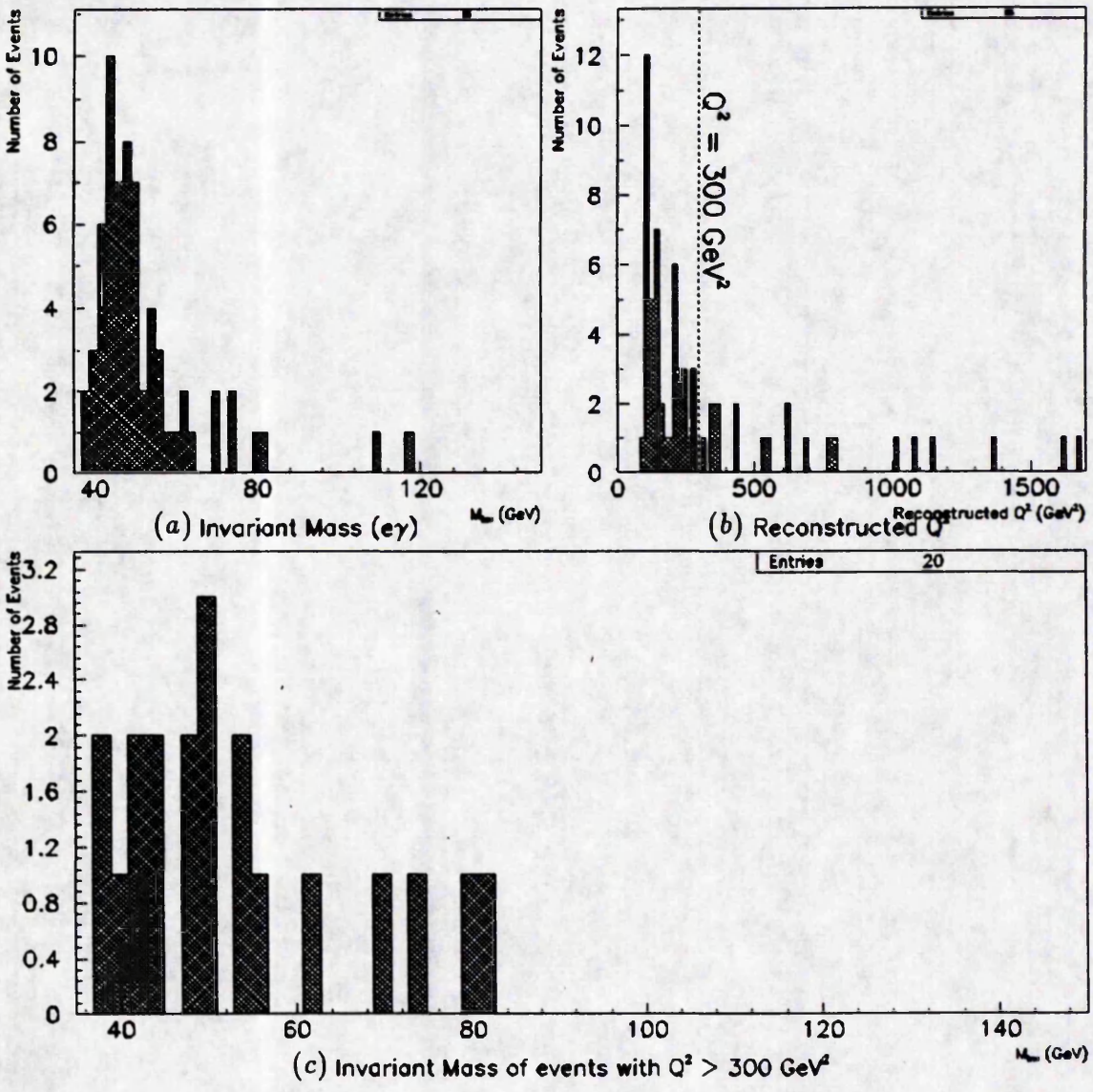

Figure 6.20: (a,b) - Invariant Mass and Reconstructed Q^2, (c) - Invariant Mass ($Q^2_{\mathbf{rec}} > 300\ GeV^2$), for LEPTO candidates ($Q^2_{\mathbf{gen}} > 100\ GeV^2$).

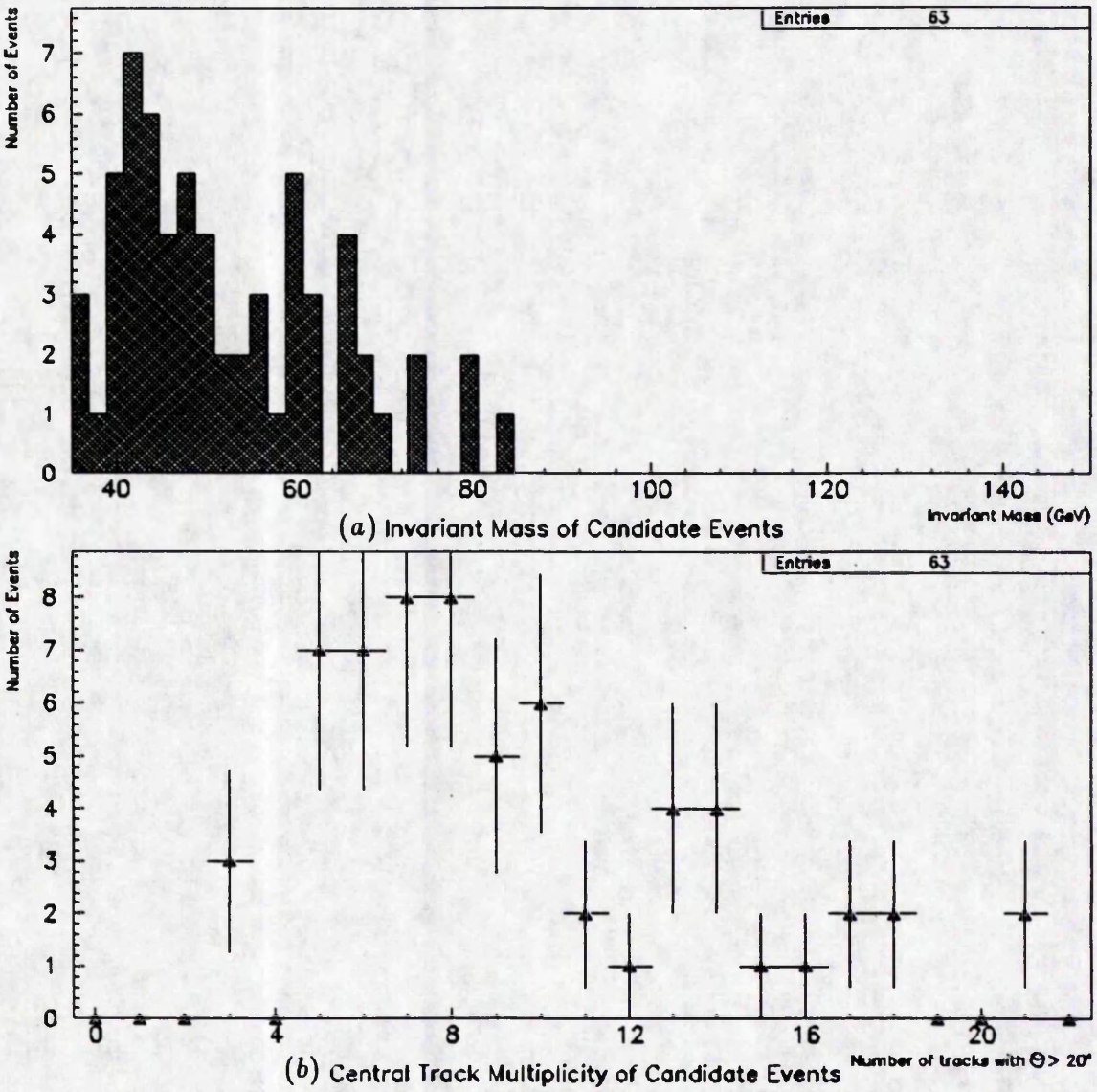

Figure 6.21: (a) - Invariant mass and (b) - central track multiplicity distributions of LEPTO 5.2 e^* background events generated with $Q^2 > 300\ GeV^2$.

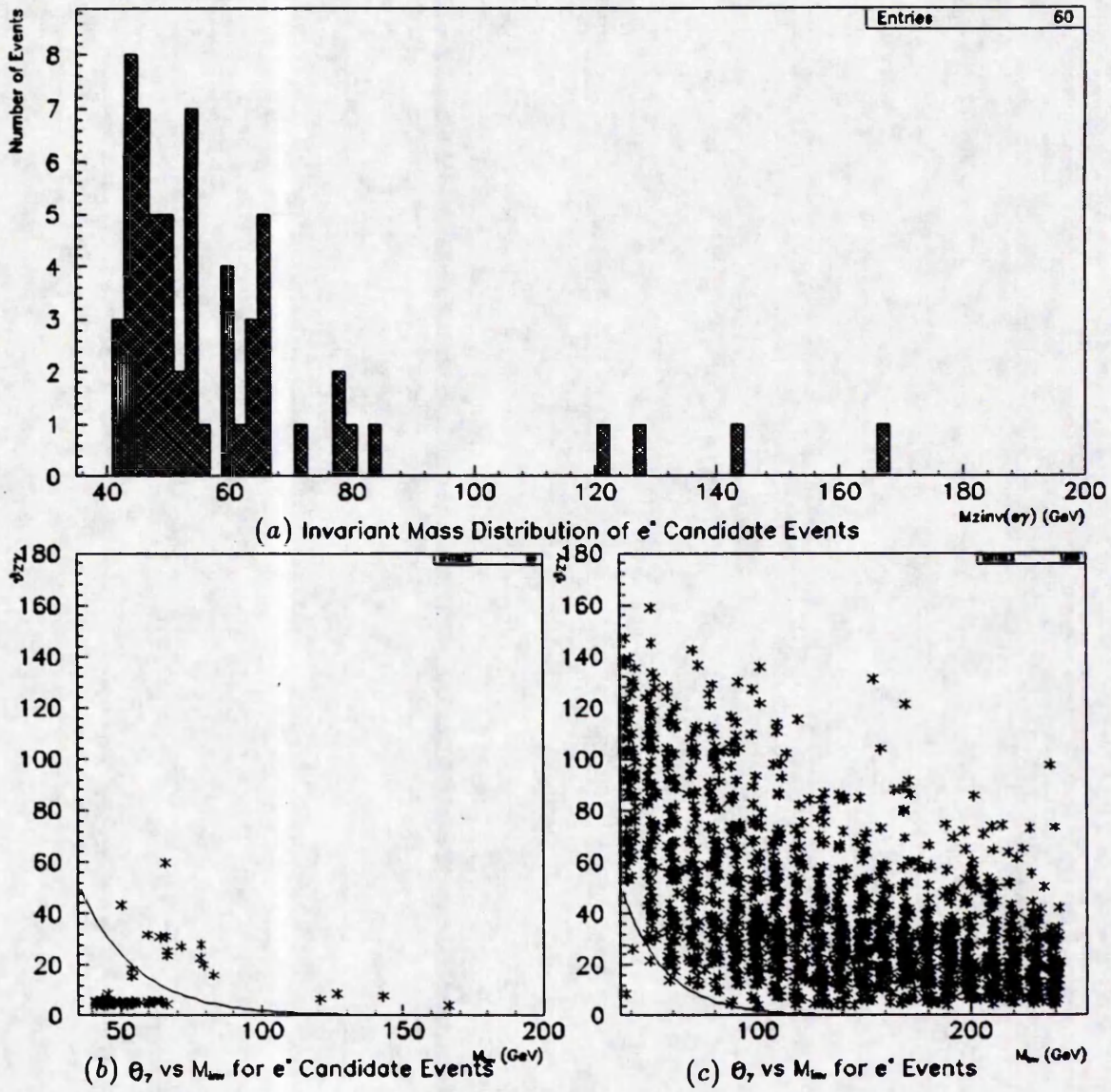

Figure 6.22: (a) - Invariant mass distribution of dataset III DIS events surviving analysis cuts, (b,c) - θ_γ vs $M_{\mathbf{inv}}$ for DIS and e^* events.

The dataset used for the results presented in the next chapter is set IV from Table 6.3. The event sample is equivalent to an integrated luminosity of $283 \pm 1 pb^{-1}$, corresponding to approximately 3 years of expected HERA data if analysed with the selection cuts developed in this section.

A summary of event cuts and performance in reducing deep inelastic neutral current scattering e^* backgrounds is given in Tables 6.4 and 6.5. The aim was to develop a set of event selection criteria which should yield an event sample relatively uncontaminated by DIS. With the cuts of set D in Table 6.4 one would expect ≈ 20 e^* candidate events over a wide range of invariant mass per year's running from DIS sources. Figure 6.23 shows a typical event of this kind in the H1 detector. In this case the decay photon candidate is actually 3 photons from the decay of a ω, highly collimated due to the high energy of the hadron and therefore identified as a single particle. Figure 6.24 shows a typical deep inelastic 100 GeV e^* event for comparison. Other events which survive the analysis cuts at this stage are mainly due to decays of the type

$$\pi^0 \rightarrow \gamma\gamma$$

$$\omega \rightarrow \pi^0\gamma \rightarrow \gamma\gamma\gamma$$

$$\eta \rightarrow \gamma\gamma$$

and are effectively indistinguishable from signal due to the tiny opening angles between the decay photons.

Table 6.5 summarises the performance of each set of analysis cuts on the sets of DIS background events, the remaining cross section for problematics after the application of the cuts. So cross sections in each column should be the same.

6.5 A Summary of Excited Electron Event Selection Cuts

The final set of cuts therefore, chosen to yield an event sample which minimizes wide angle bremsstrahlung and neutral current deep inelastic backgrounds while not seriously discriminating against any particular e^* mass in the HERA accessible range, is summarised in Table 6.6.

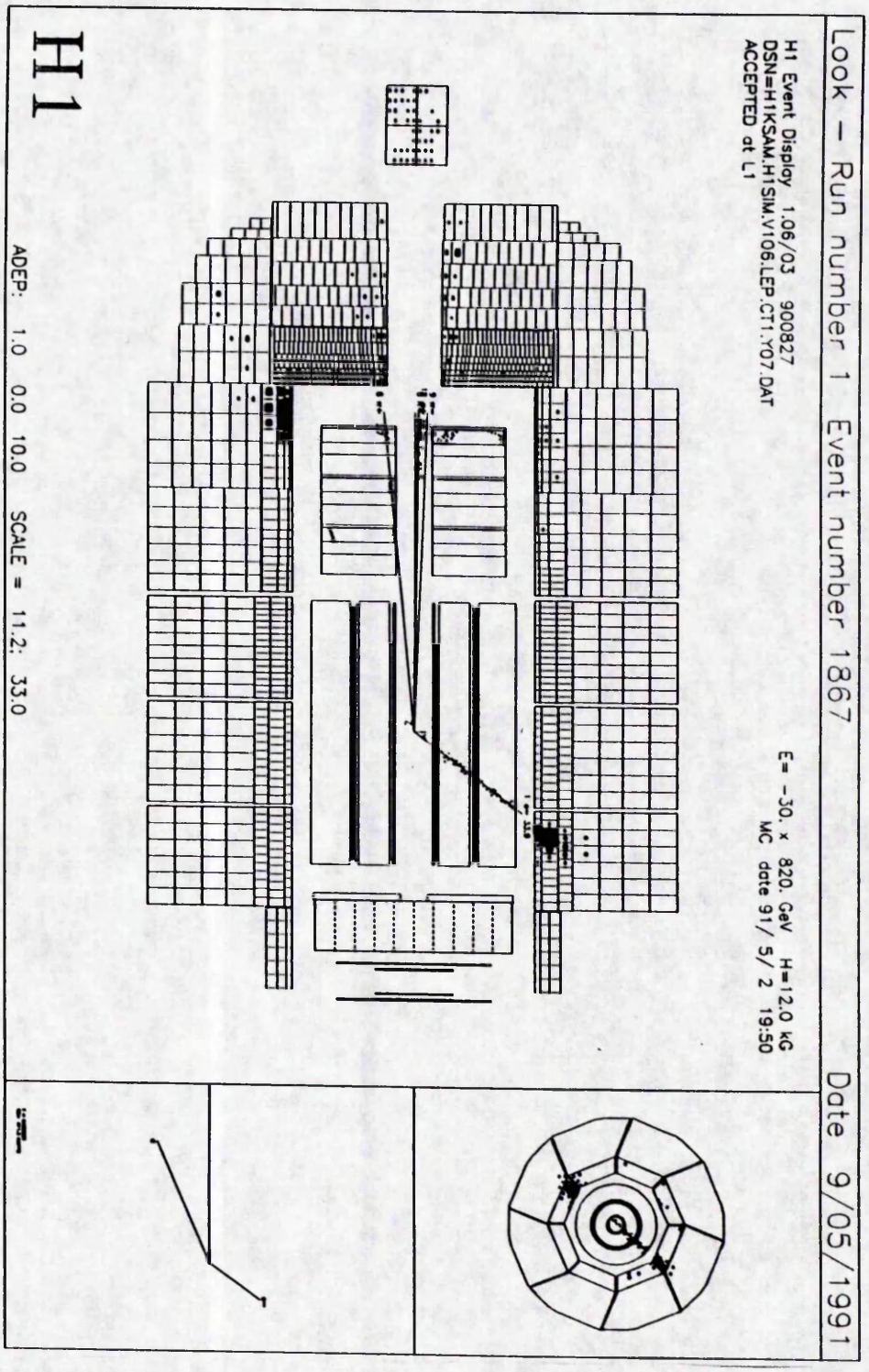

Figure 6.23: DIS e^* background event surviving all cuts. $M_{\mathbf{inv}} = 80.7GeV$ and photon candidate from the decay $\omega \to \pi^0\gamma \to \gamma\gamma\gamma$.

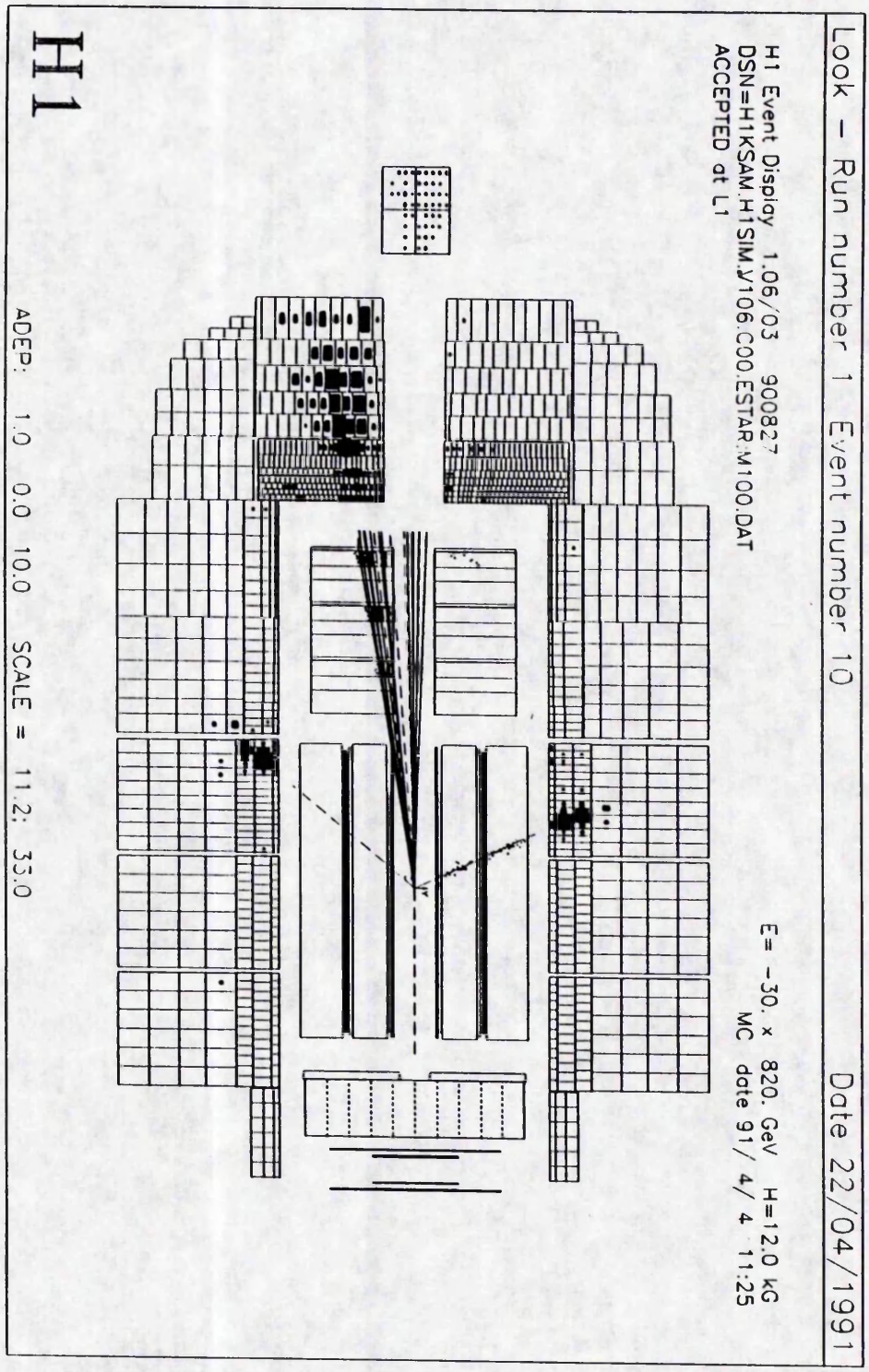

Figure 6.24: Typical deep inelastic 100 GeV e^* event in the H1 detector.

Analysis Cut Set	Event Selection Cuts
A	$\geq$ 2 clusters in event with $E > 15\ GeV$ and electromagnetic fraction $> 90\%$. $Q^2_{\mathbf{rec}} > 100\ GeV^2$ $M_{\mathbf{inv}}(e\gamma) > 35\ GeV$ $120° < \phi_{\mathbf{sep}}(e\gamma) < 240°$
B	$\geq$ 2 clusters in event with $E > 15\ GeV$ and electromagnetic fraction $> 90\%$. $Q^2_{\mathbf{rec}} > 300\ GeV^2$ $M_{\mathbf{inv}}(e\gamma) > 35\ GeV$ $120° < \phi_{\mathbf{sep}}(e\gamma) < 240°$
C	$\geq$ 2 clusters in event with $E > 15\ GeV$ and electromagnetic fraction $> 90\%$. $Q^2_{\mathbf{rec}} > 300\ GeV^2$ $M_{\mathbf{inv}}(e\gamma) > 35\ GeV$ $120° < \phi_{\mathbf{sep}}(e\gamma) < 240°$ $\leq$ 1 reconstructed track with $\theta > 20°$
D	$\geq$ 2 clusters in event with $E > 15\ GeV$ and electromagnetic fraction $> 90\%$. $Q^2_{\mathbf{rec}} > 300\ GeV^2$ $M_{\mathbf{inv}}(e\gamma) > 35\ GeV$ $120° < \phi_{\mathbf{sep}}(e\gamma) < 240°$ $\leq$ 1 reconstructed track with $\theta > 20°$ $\theta_\gamma > e^{(5.7-0.05M_{\mathbf{inv}})}$

Table 6.4: Summary of cuts used to deselect Neutral Current DIS e^* backgrounds.

DATASET	Cross Section Surviving Analysis Cuts (pb)			
	Cut Set **A**	Cut Set **B**	Cut Set **C**	Cut Set **D**
I	12.8 ± 1.5	3.6 ± 0.8	–	–
II	–	2.7 ± 0.3	–	–
III	–	–	0.6 ± 0.1	0.16 ± 0.04
IV	–	–	0.64 ± 0.05	0.20 ± 0.02

Table 6.5: Summary of analysis cut performance on LEPTO Neutral Current Deep Inelastic Scattering e^* backgrounds.

e^* **Event Selection Criteria**
≥ 2 Clusters with $E > 15\ GeV$ and Electromagnetic Fraction $> 90\%$
$Q^2_{\mathbf{rec}} > 300\ GeV^2$
$M_{\mathbf{inv}}(e\gamma) > 35\ GeV$
$120° < \phi_{\mathbf{sep}} < 240°$
≤ 1 reconstructed track with $\theta > 20°$
$e^{(5.7-0.05M_{\mathbf{inv}})} < \theta_\gamma < 140°$

Table 6.6: The Final e^* Event Selection Criteria.

Chapter 7

Discovery Limits for Excited Electrons at HERA

In this chapter limits on Λ and upper masses are set at 95% confidence level from the search for excited electrons at H1.

Event samples representing signal and all anticipated backgrounds are generated and processed by H1PSI. A final event sample representing the e^* candidate events is selected using the criteria developed in the previous chapter and summarised in Table 6.6.

Limits on Λ which can be set at H1 as a function of e^* mass are calculated. Upper limits of e^* mass which can be excluded given various values of Λ and $\int \mathcal{L}$ are also presented. These results are compared with those already set by LEP I and those predicted for LEP II.

7.1 The Event Samples

The data samples generated and subsequently analysed represent full excited electron signals in the mass range $40-240\ GeV$ and all anticipated problematics, given the analysis cuts, arising from wide angle bremsstrahlung and neutral current deep inelastic physics.

The details of these samples are summarised in Table 7.1

7.2 The Events Surviving the e^* Cuts

The characteristics of the events surviving the analysis cuts and therefore contributing to the final distributions were studied. In the case of excited electrons this was to determine

DATA SAMPLE	GENERATOR DETAILS	CROSS SECTION (pb)	# EVENTS GENERATED	EQUIVALENT $\int \mathcal{L}\ (pb^{-1})$
EXCITED ELECTRON EVENTS	COMPOS Mass $40 - 240\ GeV$ $\Lambda = 1000\ GeV$ Full γ exchange Production σ Decay $e^* \rightarrow e\gamma$ EHLQ set I $0.001 \leq x \leq 1.0$ $0.0 \leq Q^2 \leq 10^6$	Varies with Mass	2000 of each mass	Varies
WIDE ANGLE BREMSS-TRAHLUNG	EPCOMPT/COMPT $M_{\mathbf{inv}}(e\gamma) > 25\ GeV$ $E_e,\ E_\gamma > 5\ GeV$ $E_e + E_\gamma > 20\ GeV$ $3.6° \leq \theta_{e,\gamma} \leq 176°$	53 ± 0.4	26,702	503 ± 4
NEUTRAL CURRENT DIS	LEPTO 5.2 $0.001 \leq x \leq 1.0$ $300.0 \leq Q^2 \leq 10^6$ ≤ 1 Track with $\theta > 25°$ and $E > 1\ GeV$ EHLQ set I	369 ± 1	104,493	283 ± 1

Table 7.1: The signal and background data samples used in the analysis.

the magnitude and mass resolution for given e^* masses. For the background events, distribution functions were fitted to the surviving events.

7.2.1 The e^* Signal

Table 7.2 summarises the performance of the event selection package on e^* events in H1PSI. The resulting effective cross section for each e^* mass is a product of the full production cross section as calculated by COMPOS, the branching ratio to $e\gamma$ [Equations 3.15, 3.16, 3.17] and the event identification efficiencies using H1PSI and the selection criteria.

The mass resolution of the resulting e^* invariant mass peak is given as the standard deviation of a fitted Gaussian, although the generated mass is smeared with a Breit-Wigner function the dominant contribution to the finite width of the peak comes from the parameterised resolutions in H1PSI which result from fitting Gaussians to parameters derived from real data and H1SIM results.

e^* Mass (GeV)	Production σ (pb) ($\Lambda = 1000\ GeV$)	Branching Ratio to $e\gamma$	Event Identification Efficiency (%)	Effective $\sigma(pb)$ ($\Lambda = 1000\ GeV$)	Mass Resolution (GeV)
40	2.011 ± 0.004	1.00	41.2 ± 1.4	0.82 ± 0.03	0.77 ± 0.02
50	1.636 ± 0.004	1.00	51.2 ± 1.6	0.84 ± 0.03	0.87 ± 0.02
60	1.33 ± 0.01	1.00	60.2 ± 1.7	0.80 ± 0.03	1.01 ± 0.02
70	1.098 ± 0.007	1.00	56.9 ± 1.7	0.62 ± 0.03	1.08 ± 0.03
80	0.907 ± 0.004	1.00	60.4 ± 1.7	0.55 ± 0.02	1.19 ± 0.03
90	0.748 ± 0.003	0.88	64.7 ± 1.8	0.43 ± 0.01	1.18 ± 0.03
100	0.617 ± 0.002	0.72	64.6 ± 1.8	0.287 ± 0.008	1.23 ± 0.03
110	0.505 ± 0.001	0.60	63.5 ± 1.8	0.192 ± 0.005	1.33 ± 0.03
120	0.409 ± 0.001	0.53	63.4 ± 1.8	0.137 ± 0.004	1.35 ± 0.04
130	0.331 ± 0.001	0.47	64.4 ± 1.8	0.100 ± 0.003	1.36 ± 0.03
140	0.268 ± 0.001	0.44	67.1 ± 1.8	0.079 ± 0.002	1.37 ± 0.03
150	0.213 ± 0.001	0.41	66.6 ± 1.8	0.058 ± 0.002	1.38 ± 0.03
160	0.168 ± 0.001	0.39	66.3 ± 1.8	0.043 ± 0.001	1.38 ± 0.03
170	0.130 ± 0.001	0.37	65.0 ± 1.8	0.0313 ± 0.0009	1.43 ± 0.03
180	0.099 ± 0.001	0.36	65.0 ± 1.8	0.0232 ± 0.0007	1.42 ± 0.04
190	0.074 ± 0.001	0.35	65.9 ± 1.8	0.0171 ± 0.0005	1.54 ± 0.04
200	0.053 ± 0.001	0.34	66.8 ± 1.8	0.0120 ± 0.0004	1.49 ± 0.03
210	0.037 ± 0.001	0.34	66.3 ± 1.8	0.0083 ± 0.0003	1.47 ± 0.03
220	0.024 ± 0.001	0.33	64.8 ± 1.8	0.0051 ± 0.0003	1.59 ± 0.03
230	0.015 ± 0.001	0.32	66.7 ± 1.8	0.0032 ± 0.0002	1.50 ± 0.03
240	0.009 ± 0.001	0.32	64.1 ± 1.8	0.0018 ± 0.0001	1.53 ± 0.03

Table 7.2: Summary of analysis performance for excited electron events.

7.2.2 The Wide Angle Bremsstrahlung Background Distribution

Figure 7.1 shows the invariant mass distribution for an event sample representing $503 \pm 4pb^{-1}$ of wide angle bremsstrahlung background events surviving the e^* event selection. Figure 7.2 shows the corresponding distribution of effective cross section ($pb\ GeV^{-1}$) with $M_{\mathbf{inv}}(e\gamma)$ and the function fitted.

7.2.3 The Deep Inelastic Scattering Background Distribution

Figure 7.3 shows the invariant mass distribution for $283 \pm 1pb^{-1}$ of deep inelastic scattering background events surviving the e^* event selection. Figure 7.4 shows the corresponding distribution of effective cross section ($pb\ GeV^{-1}$) with $M_{\mathbf{inv}}(e\gamma)$ and the function fitted.

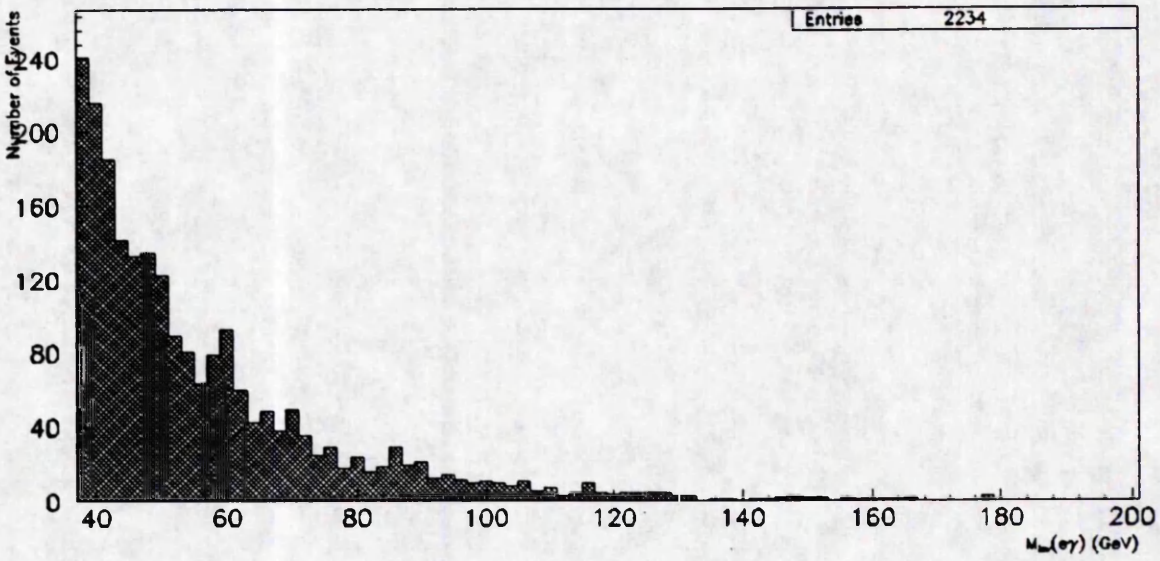

Figure 7.1: Invariant mass distribution of $503 \pm 4 pb^{-1}$ of wide angle bremsstrahlung events which survive the e^* selection cuts.

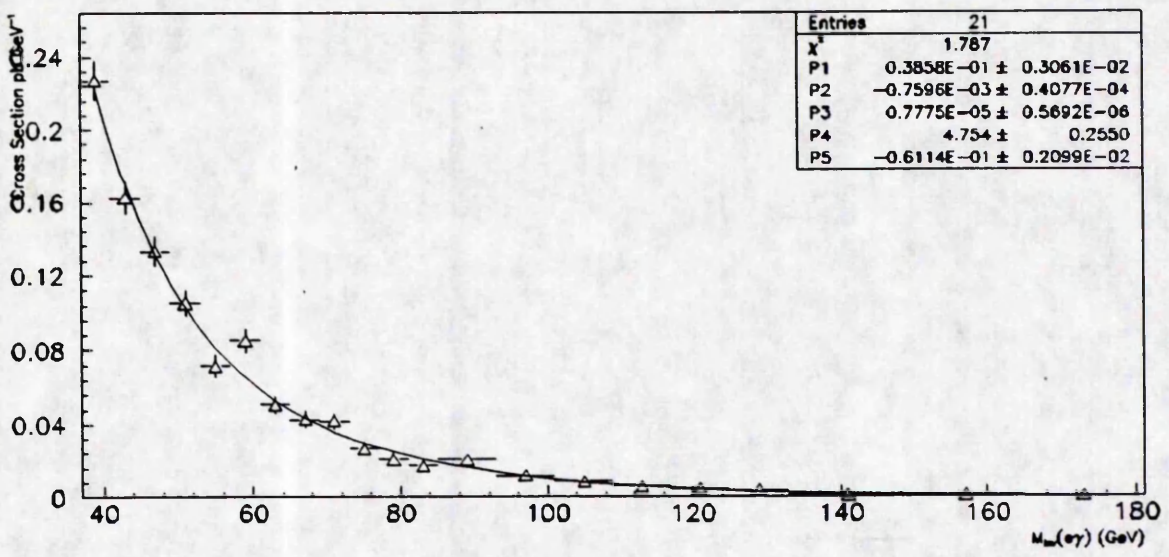

Figure 7.2: Cross section distribution with M_{inv} of wide angle bremsstrahlung events which survive the e^* selection cuts.

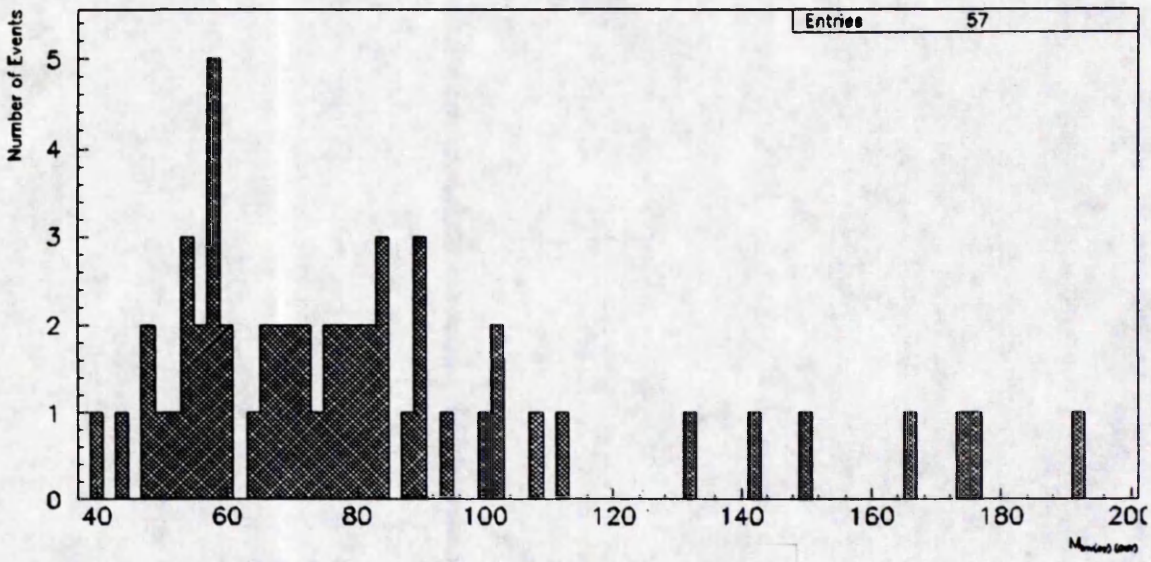

Figure 7.3: Invariant mass distribution of $283 \pm 1 pb^{-1}$ of deep inelastic scattering events which survive the e^* selection cuts.

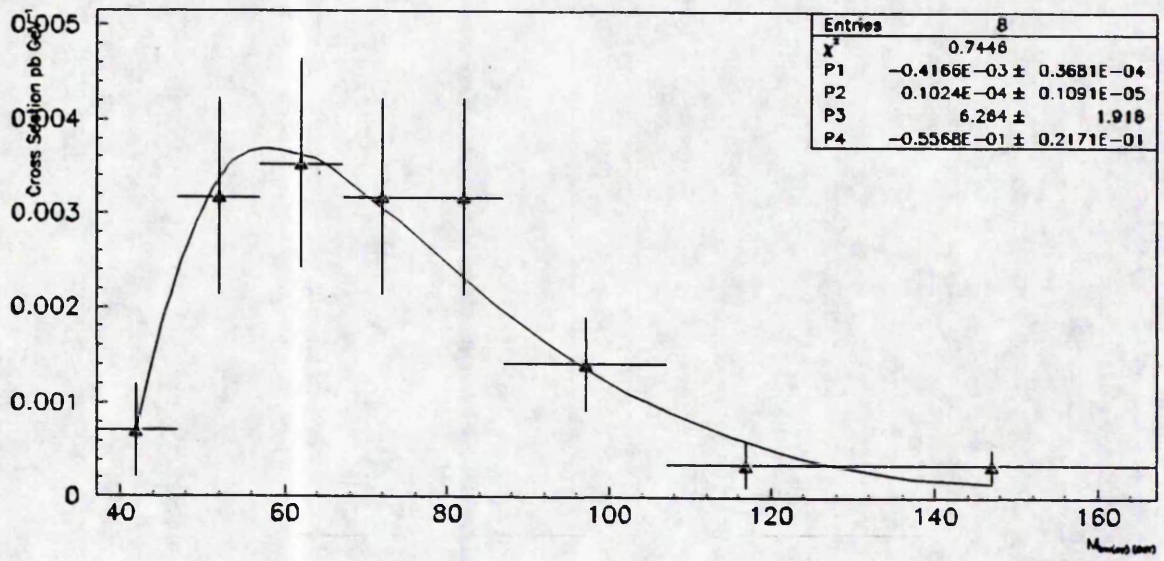

Figure 7.4: Cross section distribution with M_{inv} of deep inelastic physics events which survive the e^* selection cuts.

7.3 Electron Compositeness Limits from H1 and HERA

Given the fitted cross section distributions of Figures 7.2 and 7.4, the effective cross sections and widths of the e^* peaks (Table 7.2) and the variation of e^* production cross section with compositeness scale (Figure 3.4) ;

$$\sigma_{e^*}(\Lambda) = \sigma_{e^*(\Lambda=1000GeV)}.10^6.\Lambda^{-2} \tag{7.1}$$

One can set limits at 95% confidence limits on e^* masses and Λ at HERA.

7.3.1 Limits on Λ

For a given integrated luminosity $\mathcal{L}$ the total number of background events, $n_{\mathbf{bkd}}$, in the same mass bin as 95% of the excited electron events can be calculated. This is done using the fitted background distributions, Table 7.2 which summarises the e^* event performance of the cuts and the assumption that 95% of the e^* events are contained in a bin $\pm 1.96\sigma_{\mathbf{width}}$ centered on the e^* mass.

One then uses the Poisson probability distribution for observing $N_{\mathbf{obs}}$ events in a bin when $n_{\mathbf{bkd}}$ are expected and perform a summation until

$$\sum_N P(N) \geq 0.95 \tag{7.2}$$

and an approximate value for the number of events above which a 95% confidence limit of not belonging to the expected background distribution can be set.

This immediately yields a lower bound on e^* effective cross section at this mass since

$$N_{\mathbf{obs}}(95\%CL) = n_{e^*}(\mathbf{min}) + n_{\mathbf{bkd}} \tag{7.3}$$

and

$$\sigma_{e^*}(\mathbf{min}) = \frac{n_{e^*}(\mathbf{min})}{\mathcal{L}} \tag{7.4}$$

So, the failure to observe an excited electron signal to 95% confidence limit at a given e^* mass and integrated luminosity excludes Λ values up to

$$\Lambda = 10^3.\sqrt{\frac{\sigma_{e^*(\Lambda=1000GeV)}}{\sigma_{e^*}(\mathbf{min})}} \tag{7.5}$$

Figure 7.5 shows the limits which can be set on the magnitude of Λ as a function of e^* mass for $\mathcal{L} = 100pb^{-1}$ at HERA. The falling off in maximum Λ at lower e^* masses is

due to the lower event selection efficiencies in this region. The region also corresponds to largest background levels. At masses greater than approximately 140 GeV the maximum Λ accessible falls even more rapidly than before this point. This is due to the 1 event minimum required when expected background levels have fallen well below this value.

A price is obviously paid for the event selection cuts which discriminate against lower mass excited electrons, that is $Q^2 > 300\ GeV^2$ and the minimum cluster energy requirements. This situation can be improved on by removing these cuts and making use of Figures 6.13 through 6.17 which illustrate the different wide angle bremsstrahlung and excited electron decay product distributions at these low masses. In this region the magnitude of the background is comparable to that of the signal and thus these cuts can reduce the signal to background ratio. This would however involve a study of vastly greater number of deep inelastic backgrounds since the powerful Q^2 cut is lost. If a certain amount of anticipation, for example only processing generator events through H1PSI if they contain high energy photons at finite angles in the detector, is employed this signal is probably generatable. However, this is not as desirable as a full event sample study.

So, given a year's running of HERA at design luminosity ($100pb^{-1}$) compositeness limits at 95% confidence limits extend from

$$\Lambda > 2500GeV^2 \quad (m_{e^*} = 40GeV) \tag{7.6}$$

$$\Lambda > 3100GeV^2 \quad (m_{e^*} = 60GeV) \tag{7.7}$$

to

$$\Lambda > 400GeV^2 \quad (m_{e^*} = 240GeV) \tag{7.8}$$

on lower limits to the value representing the scale of the production interaction.

The compositeness limits derived in this study can be compared to those predicted for an equivalent integrated luminosity at HERA. The work of Berger *et al.* [27] is a study of elastic channel excited electrons only, with a limiting background due to wide angle bremsstrahlung $e + p \rightarrow e + p + \gamma$. Cuts on Q^2, x, $\sum p_T$, $M_{\mathbf{inv}}$ and opening angle which are mass dependent are put on the data, but no detector simulation is performed. The limits derived ($\mathcal{L} = 200pb^{-1}$) are shown in Figure 7.6 together with an equivalent set of values derived in this study.

The general increased sensitivity of the results using the whole e^* signal over an elastic channel search is obvious. Note also that Berger performed no detector simulation and

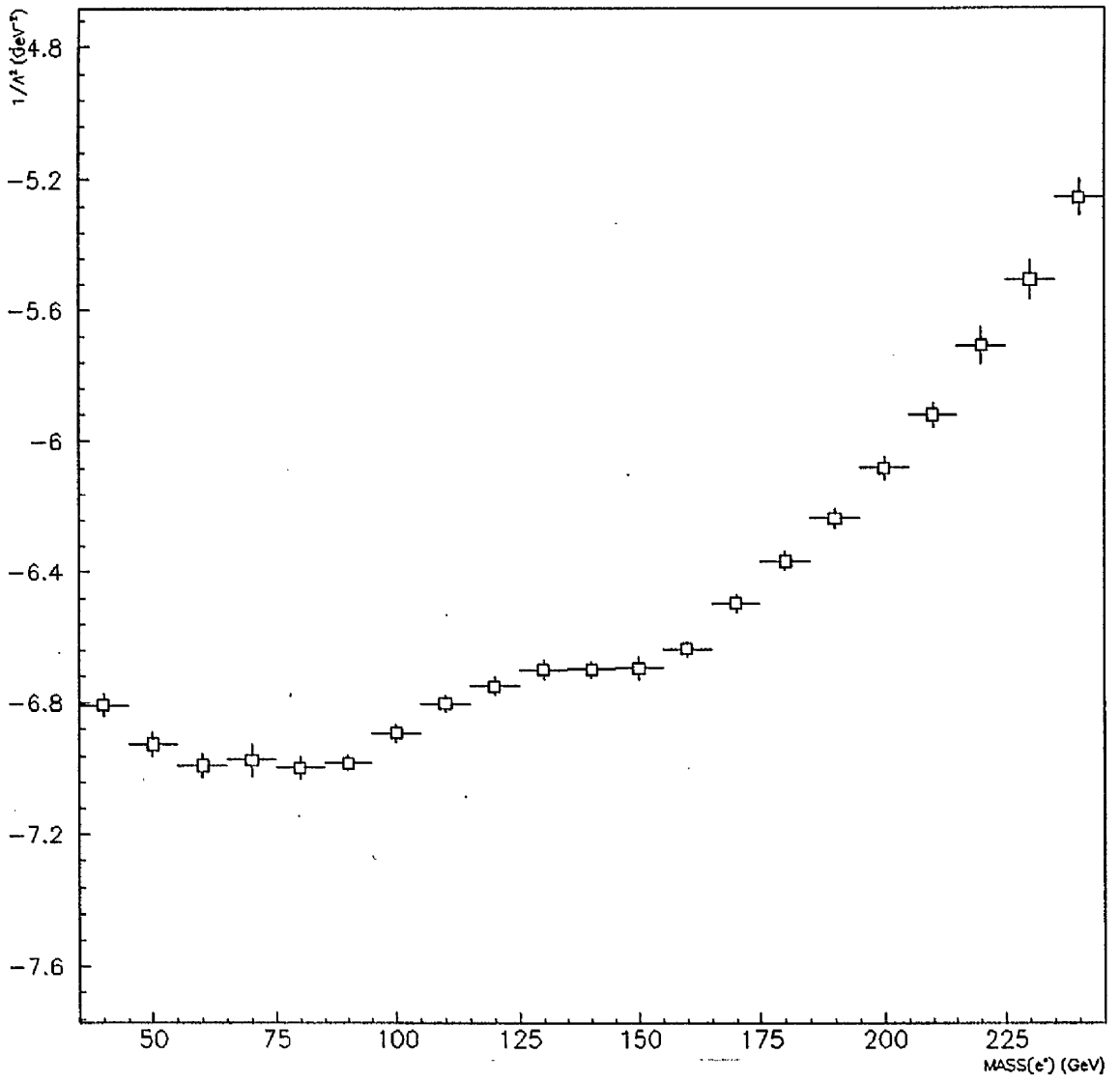

Figure 7.5: Limits on Λ at HERA ($\int \mathcal{L} = 100 pb^{-1}$).

assumed 100% identification efficiency for events which survive the selection criteria. There is also a question as to whether, in stressing the benefits of a search for e^*'s in the elastic channel only, the sizeable fraction of quasi-real $ep \rightarrow eX\gamma$ bremsstrahlung events which have the $e\gamma$ pair back to back in the lab and are therefore indistinguishable from elastic bremsstrahlung have been neglected in background calculations.

Results at lower e^* masses are better in the elastic search, this is probably a reflection of the difficulty of generating deep inelastic backgrounds in this region rather than a real effect and can be improved upon using the methods discussed earlier in this section.

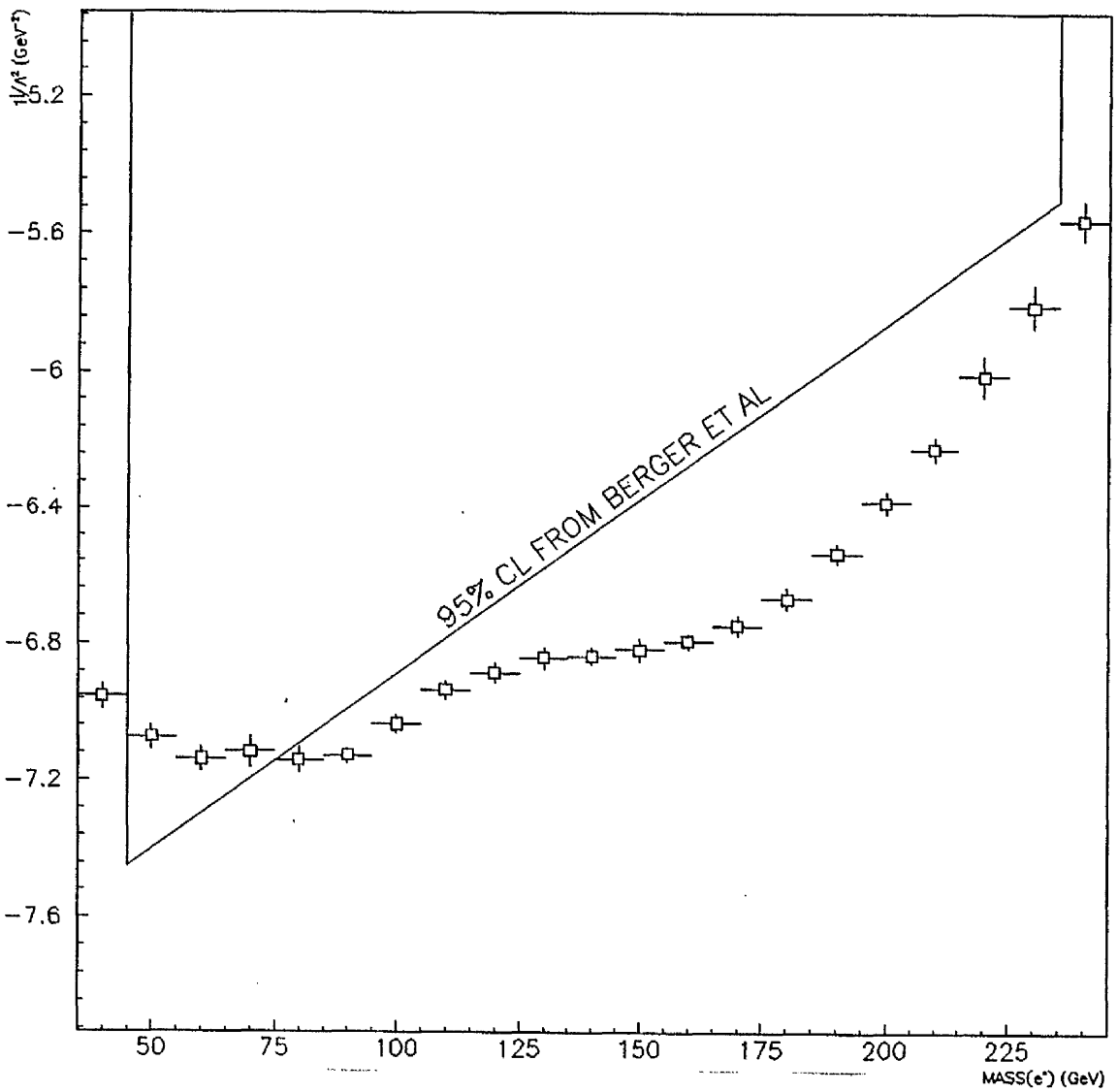

Figure 7.6: Limits on e^* production at HERA (200 pb^{-1}).

A comparison with the results from LEP 1 is made in Figure 7.7 where the 95% confidence limits derived from failing to find an excited electron peak at $\mathcal{L} = 1.15pb^{-1}$ are compared to the equivalent results published by the OPAL collaboration [17]. So, given the same luminosity one would expect more stringent limits on compositeness from HERA rather than LEP. Note, the effective cross sections have been corrected in the data calculated in this work to assume a 100% branching ratio $e^* \rightarrow e\gamma$ since this is an assumption of the OPAL paper.

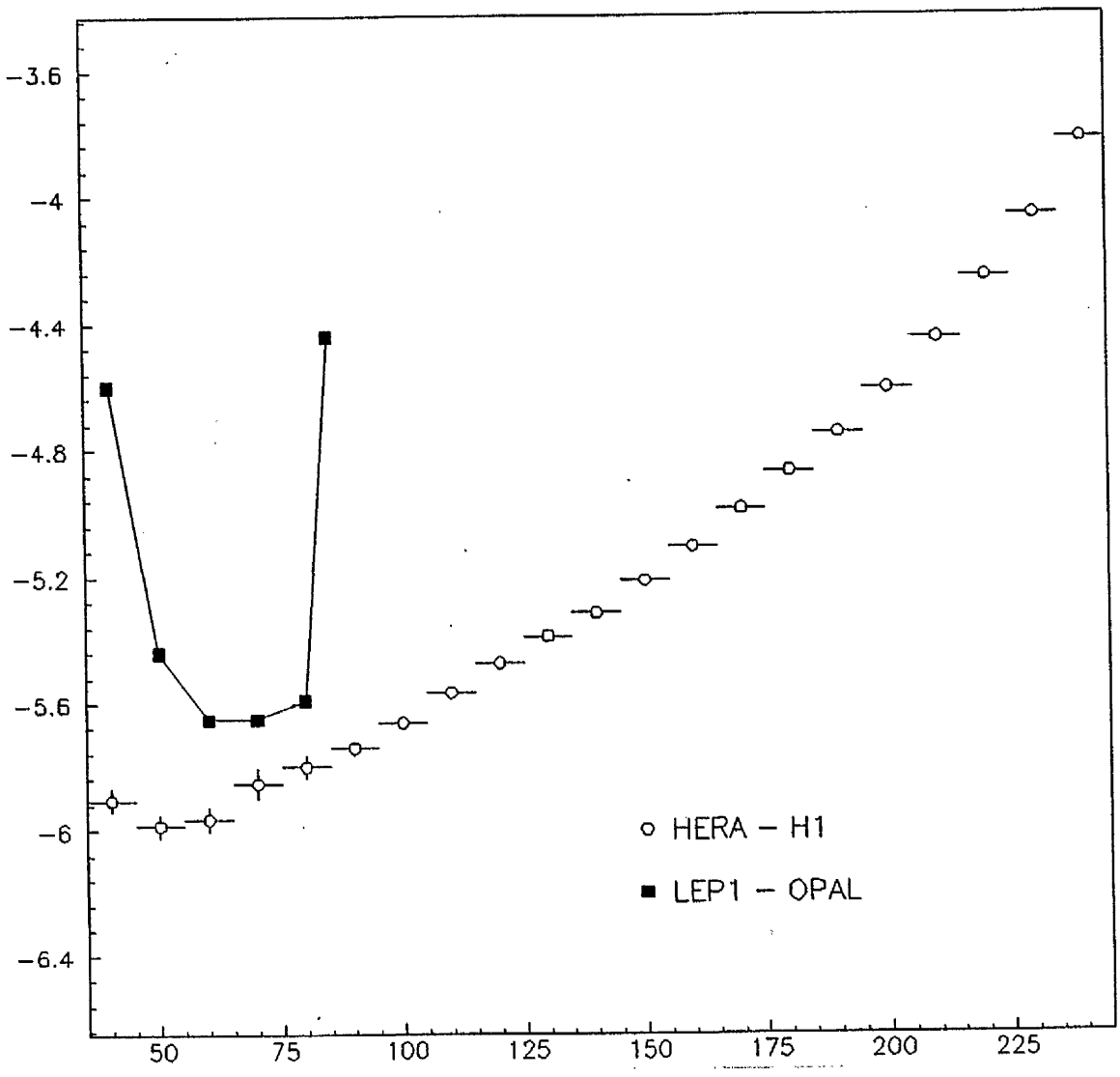

Figure 7.7: Limits on e^* production at HERA/H1 and LEP1/OPAL (1.15 pb^{-1}).

In reference [19] Treille *et al.* study the compositeness limits available at LEP 2 also based on single production $e^+e^- \rightarrow e^{*\pm}e^{\mp}$. A 100% branching ratio $e^* \rightarrow e\gamma$ is again assumed. In Figure 7.8 results for $500pb^{-1}$ from LEP 2 and HERA are compared. These results show that at masses above 50 GeV HERA will provide more stringent limits on the scale of e^* production interactions than both LEP 1 and LEP 2 given the same integrated luminosities. Since the anticipated luminosities for the 3 colliders are roughly equal [12] one can therefore expect the highest limits on Λ to come from HERA results.

At a more realistic estimate for HERA of $200pb^{-1}$ of total data HERA can be expected to extend limits on Λ to approximately $4000GeV$ at $m_{e^*} = 80GeV$ and $600GeV$ at $m_{e^*} = 240GeV$.

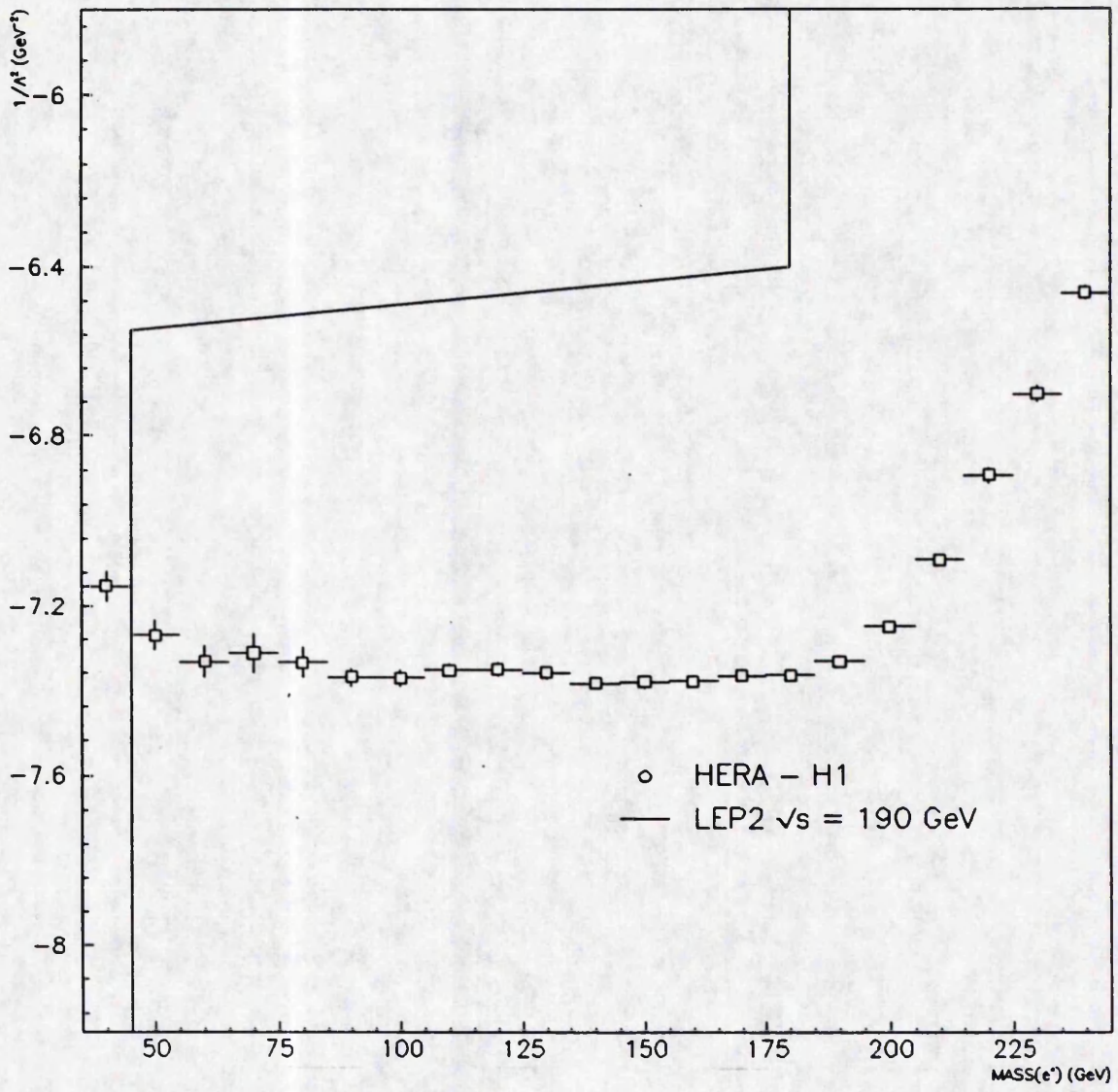

Figure 7.8: Limits on e^* production at HERA/H1 and LEP2 (500 pb^{-1}).

7.3.2 Excited Electron Mass Limits at HERA

Another composite limit which can be set at HERA is the highest mass which can be excluded at 95% confidence limit for a given $\mathcal{L}$ and Λ.

Approximate e^* mass limits for various values of $\mathcal{L}$ and Λ are shown in Figure 7.9. Zero entries correspond to mass limits below 40 GeV, the mass range already excluded at 95% in pair production studies at LEP [16]. It can be seen that the present limits on e^* from single production searches (Table 2.5) shall be much improved at HERA, and with more stringent requirements on the transition coupling. For example, $100pb^{-1}$ of data is expected to exclude e^* masses from $200GeV(\Lambda = 1000GeV)$ to $90GeV(\Lambda = 3000GeV)$ at 95% confidence levels.

Given $200pb^{-1}$ of HERA data masses up to $220GeV$ can be excluded ($\Lambda = 1000GeV$). For masses above this value one runs out of rate for realistic values of Λ.

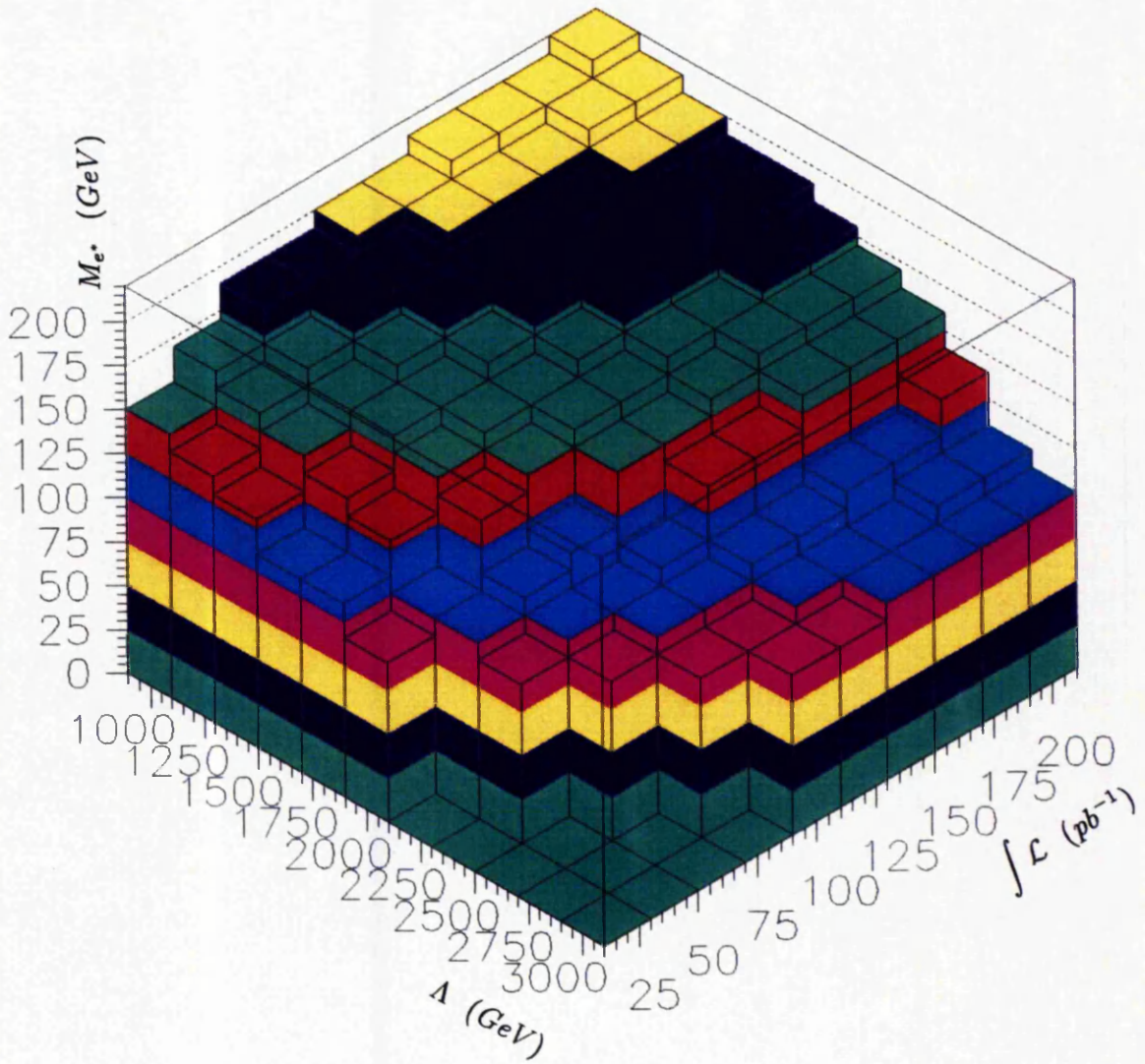

Figure 7.9: Excited electron mass limits from HERA.

7.4 Conclusions

The results of this study show that the prospects for extending composite searches and limits at HERA are very promising.

Using a general event selection procedure, limits on the interaction scale Λ can be extended to values comparable to those set on composite scale Λ_c from contact interaction studies, and are expected to be in excess of those set by both LEP and LEP II. Mass limits on single e^* production supercede existing results with more stringent restrictions on the transition coupling $\lambda(=\frac{m_{e^*}}{\Lambda})$.

These results can be improved on by introducing more mass dependent cuts into the selection procedure and possibly increasing the estimated e^* event identification efficiency in a study of the signal using the full detector Monte Carlo.

Bibliography

[1] G. B. West. (Ed) *Los Alamos Primer for Particle Phyiscs.* 1988 Cambridge University Press.

[2] F. Halzen, A. D. Martin. *Quarks and Leptons* 1984 John Wiley & Sons, New York.

[3] Donald H. Perkins. *Introduction to High Energy Physics.* 1987 Addison-Wesley Publishing Company Inc.

[4] I. J. R. Aitchison & A. J. Hey. *Gauge theories in Particle Physics (Second Edition)* 1989 Adam Hilger.

[5] F. Dydak. *Review Talk, International Conference on High Energy Physics.* Singapore August 1990

[6] H. Fritzcsh. *Lectures given at the International School on Subnuclear Physics.* Erice, Sicily August 1984

[7] *DESY at Microcosm CERN.* DESY PR 1990

[8] *Technical Proposal for the H1 Detector.* The H1 Collaboration DESY 1986

[9] *H1 Technical Progress Report.* The H1 Collaboration DESY 1987

H1 Technical Progress Report. The H1 Collaboration DESY 1988

H1 Technical Progress Report. The H1 Collaboration DESY 1989

H1 Technical Progress Report. The H1 Collaboration DESY 1990

[10] R. Fernow, *Introduction to Experimental High Energy Physics.* Cambridge University Press (1986).

[11] Braunschweig et al., Z.Phys. C37 p171 (1988).

Bartel et al., Z.Phys. C30 p371 (1986).

Bartel et al., Z.Phys. C31 p359 (1986).

Abe et al., Phys. Lett. B232 p425 (1989)

Jododio et al., Phys. Rev. D34 p1967 (1986), Phys. Rev. D37 p237 erratum. (1988).

Abe. et al., Phys. Rev. Lett. 62 p613 (1989).

[12] *Review of Particle Properties.*, Phys. Lett. B239 II.27,IX.9 (1990).

[13] E. J. Eichten and K. Lane., Phys. Lett. B90 p125 (1980).

[14] E. J. Eichten et al., Phys. Rev. Lett. 50 p811 (1983).

[15] G. 't Hooft. *Recent Developments in Gauge Theories.* Plenum, New York, 1980.

[16] Decamp et al., Phys. Lett. B236 p501 (1990).

Adachi et al., Phys. Lett. B228 p553 (1989).

[17] Akrawy et al., Phys. Lett. B224 p135 (1990).

[18] K. Hagiwara, S. Komamiya, D. Zeppenfeld, Z. Phys. C29, p115 (1985).

[19] D. Treille, *Proceedings of the ECFA Workshop on LEP200 Vol. II p414*, Aachen 1986, CERN 87-08.

[20] R. Kleiss, P. M. Zerwas, *Proceedings of the Workshop on physics at future colliders Vol. II p277*, La Thuile 7-13 January, CERN 87-07.

[21] F. Cornet, Rückl, *Proceedings of the Workshop on physics at future colliders Vol. II p288*, La Thuile 7-13 January, CERN 87-07.

[22] G. Ingleman et al., Proceedings of the HERA Workshop Vol. 1. Hamburg October 12-14 p3 (1987)

[23] U. Baur, H. Fritzcsh, Phys. Lett. B134, p105 (1984).

[24] F. M. Renard, Phys. Lett. B116, p264 (1982).

F. del Aguila et al., Phys. Lett. B140, p431 (1984).

M. Suzuki, Phys. Lett. B143, p237 (1984).

[25] F. M. Renard, Phys. Lett. B126, p59 (1983).

N. Cabibbo et al., Phys. Lett. B139, p459 (1984).

A. De Rújula et al., Phys. Lett., B140, p253 (1984).

J. Kuhn, P. Zerwas, Phys. Lett. B147, p189 (1984).

[26] T. Köhler, *Ereignisgeneratoren zur Elektron Proton Streuung*, Diploma Thesis RWTH Aachen, (1990).

[27] Ch. Berger, Proceedings of the HERA Workshop Vol. 2, Hamburg October 12-14 p813 (1987).

[28] A. Courau, H1 Internal Report, H1-07/91-186, July 1991.

[29] F. W. Brasse et al., Nucl. Phys. B39 p421 (1972).

[30] D. W. Duke, J. F. Owens. Phys. Rev. D30 p49 (1984) .

[31] T. Sjöstrand *The Lund Monte Carlo for hadronic processes - JETSET version 6.2,* LU TP-85-10, Comp. Phys. Comm. 39 p347 (1986).

T. Sjöstrand, M. Bengtsson, *JETSET version 6.3 (updates),* LU TP-86-22

[32] B. Anderson, G. Gustafson, G. Ingleman, T. Sjöstrand, Phys. Rev. Rep. 97 p33 (1983).

T. Sjöstrand, Phys. Lett. B142 p420 (1984), Nucl. Phys. B248 p469 (1984)

B. Andersson, G. Gustafson, G. Ingleman, T. Sjöstrand LU TP 84-9 T. Sjöstrand, Z. Physik C26 p93 (1984)

[33] G. Ingleman, T. Sjöstrand, *A Monte Carlo for leptoproduction,* LU TP 80-12.

G. Ingleman, *LEPTO Version 4.3 - The Lund Monte Carlo for deep inelastic lepton nucleon scattering,* CERN pool program W5046 long write-up (1987).

G. Ingleman, *LEPTO 5.2 Manual,* DESY Central IBM (T00ING.LUND.INFO52).

[34] T. Köhler, *COMPOS Version 1.1 Manual,* DESY Central IBM, (1991). 'F14KOE'.

[35] F. Raupach, Talk to the H1 Exotics Group, DESY, June 1990.

[36] Budnev et al., Phys. Rep. C15 p181 (1975).

[37] R. Brun et al., *GEANT detector simulation program,* CERN Program Library.

[38] J. Meyer (Ed.), *H1SIM long writeup and manual,* DESY Central IBM, (1991). 'HERA01.H1SIM'.

[39] P. Schleper, *H1PSI version 0.92 Guide,* DESY Central IBM, (1991). 'HERA01.H1PSI'.

[40] V. Blobel, *The BOS System,* DESY Internal Report, DESY R1-88-01, January 1988.

V. Blobel, *FPACK - A general input/output system,* DESY Central IBM, (1991). 'HERA01.FPACK'.

[41] Z. Y. Feng et al., *The basic H1DDL Rules,* H1 Internal Report, H1-06/90-139 (1990).

U. Berthon et al., *A Data Management Tool Package for H1 Reconstruction and Analysis,* DESY Computer Centre, 'HERA01.H1.DATMAN.DOC(DATTEX)' (1990).

Acknowledgements

I'd like to thank the entire Manchester high energy group for all the help and advice over the course of my Ph.D. Special thanks to Tony Doyle for his time and patience and the huge amount of stuff he taught me, Phil Ottewell and Scott Koyla for knowing everything and always willing to help with wisecracks thrown in, and to Dave Mercer for putting up with me in Prague. To John Ellison for his ideas and guidance and patient proof-reading of this thesis.

I'm not sure if I'd have been able to stick things out without the Manchester students I've been lucky enough to work (well, mostly talk about anything other than HEP) with. Ashy and Allister, the two best officemates in the world and who are both great at putting HEP into perspective, and Sara and Mark, 25% shareholders in the mysterious disappearing Koosh balls.

The members of the 1989−1990 Manchester University womens' football team for some great nights out, especially Sarah, Kirsty and Helen, and to Pete Hinde who couldn't be more different and has put up with my continual whinging for a long time now.

If this doesn't sound too naff, to Hamburg for being such a great place to live, and to SERC for giving me the chance to do so. Simon 'Jaaaaaames Brown' Lumsdon and Christine, she'll probably be dead miffed she's mentioned in something as dull as a physics thesis, who along with Mr Dann made the time in Germany pretty darned good fun. Doug Gillespie as well, who kept throwing those parties even though we kept throwing up all over his flat.

Chris 'I"m the trendiest dude in the physics department' Barham who is still my mate even though I'm such a shit.

A big mention to my family who are sound, especially my Mum who's superb.

Finally to Dawn French and Jennifer Saunders who have provided me with about half of my conversation for the last two years, and who are the funniest thing on four legs.